Modelling and Estimation of Aerodynamic Disturbances Acting on a Hovering Micro Helicopter in Close Proximity to Planar Surfaces

David Conal Robinson

Bachelor of Engineering (Honours)

A thesis submitted for the degree of Doctor of Philosophy

Monash University

Faculty of Engineering

Melbourne, Australia

2016

Copyright Notice

© David Conal Robinson (2016). Except as provided in the Copyright Act 1968, this thesis may not be reproduced in any form without the written permission of the author.

I, David Conal Robinson, certify that I have made all reasonable efforts to secure copyright permissions for third-party content included in this thesis and have not knowingly added copyright content to my work without the owner's permission.

Abstract

Micro rotor-craft, and micro helicopters in particular, are a class of micro aerial vehicle (MAV) that utilise rotary wings to generate lift. Such aircraft are capable of hovering and performing precise manoeuvres, making them particularly well suited to carrying out missions within confined indoor or urban environments. Operation within a confined environment will, by definition, place a micro rotor-craft in close proximity to obstacles. Fluid interactions between rotors and adjacent obstacles will induce aerodynamic disturbances that can have adverse effects on stability and performance. At a micro scale, viscous effects are more dominant within the flow due to the low Reynolds number regime that micro rotors operate within. With the exception of a hovering micro rotor near a ground plane, fluid interactions between low Reynolds number micro rotors and adjacent obstacles are poorly understood. The research outlined in this thesis extends the existing body of micro rotor research by investigating the physical nature of fluid interactions between a hovering micro rotor and nearby planar surfaces.

This thesis uses an unsteady computational fluid dynamics (CFD) method to investigate fluid interactions between a micro rotor and ceiling and wall planes. A Reynolds-averaged Navier-Stokes (RANS) method is used to resolve the flow field and a Spalart-Allmaras turbulence model is used to account for turbulent effects. An immersed boundary technique is used to model the effect of the planar surfaces near the rotor. The CFD method is comprehensively validated by comparison against experimental measurements, two-dimensional fluid dynamics theory and results from the existing literature. The CFD results show that a hovering micro rotor in close proximity to a ceiling plane will experience an increase in thrust and efficiency as rotor-ceiling gap decreases. This effect is driven by an increase in local effective angle

of attack along the blade which is caused by the ceiling plane reducing the induced velocity through the rotor disk. For a hovering micro rotor in close proximity to a wall plane, asymmetry in the flow field induces a thrust imbalance across the rotor disk. This generates a torque that will rotate the rotor disk toward the wall plane.

Additionally, as a first step toward implementing control systems for stabilising micro helicopters in close proximity to obstacles, this thesis postulates a novel linear simultaneous state and disturbance estimator for estimating disturbances induced by aerodynamic proximity effects during flight. The estimator relies only on measurements that are provided by a helicopter's on-board inertial sensors and considers the effect of direct feed-through of force disturbances to measured accelerations. Flight test results show that this scheme can provide a fair in-flight estimate of aerodynamic disturbances that are induced by fluid interactions with ground, ceiling and wall planes. Finally, it is shown that the disturbance estimate, along with *a priori* knowledge of how the disturbance varies with proximity to a ground/ceiling/wall plane, can be used to passively estimate proximity. This is a significant contribution of this thesis as the passive proximity estimate can serve as the basis for future development of robust helicopter control and collision avoidance systems.

Declaration

This thesis contains no material which has been accepted for the award of any other degree or diploma at any university or equivalent institution and, to the best of the author's knowledge and belief, this thesis contains no material previously published or written by another person, except where due reference is made in the text of the thesis.

Publications during enrolment

David Conal Robinson, Hoam Chung and Kris Ryan. Numerical Investigation of a Hovering Micro Rotor in Close Proximity to a Ceiling Plane. In: *Journal of Fluids and Structures*, 2016.

David Conal Robinson, Kris Ryan and Hoam Chung. Helicopter Hovering Attitude Control Using a Direct Feedthrough Simultaneous State and Disturbance Observer. In: *Systems and Control, IEEE Multi-Conference on*, 2015.

David Conal Robinson, Hoam Chung and Kris Ryan. Computational Investigation of Micro Helicopter Near-Wall Effect. In: *19th Australasian Fluid Mechanics Conference*, 2014.

David Conal Robinson, Hoam Chung and Kris Ryan. Computational Investigation of Micro Rotorcraft Near-Wall Hovering Aerodynamics. In: *Unmanned Aircraft Systems, International Conference on*, 2014.

David Conal Robinson, Kris Ryan and Hoam Chung. Evaluation of Micro Coaxial Rotor, Single Rotor and Quad Rotor Hovering Attitude Dynamics Using System Identification. In: *AUVSI Unmanned Systems*, 2014.

David Conal Robinson, Erin Doherty, Steve Tsai and Hoam Chung. Design and System Identification of a Micro Coaxial Helicopter Testbed. In: *Advanced Intelligent Mechatronics, IEEE/ASME International Conference on*, 2013.

Acknowledgements

Hoam and Kris, thank you for the many hours that you have spent in meetings with me, giving me feedback on my thesis and guiding me through my research. Your collective input has helped me to hone my research, writing and presentation skills - certainly, I have learnt a lot from you both and I am very grateful for the time and effort that you have both invested in me. Kris, I still hope to one day be as good at public speaking as you are.

Tracy, Julia and Megan, thank you for your continued encouragement and support over the last few years. And Mum and Dad, you have taught me the value of education and I'll be forever grateful for this. I love you all.

And to Tess, thank you for putting up with me, especially over the past six months while I have been writing (it's over now, I promise!). I love you and I can't tell you how lucky I am to be able to come home to your company every night.

Contents

Nomenclature **xv**

Abbreviations **xxiii**

1 Introduction **1**

1.1 Challenges Facing Micro Helicopters in Confined Environments . . . 2

1.2 Objectives and Scope 3

1.3 Contributions of this Thesis 5

1.4 Overview of Thesis Structure 6

2 Background and Literature Review **9**

2.1 Micro Rotor-Craft Flight Vehicles 9

2.1.1 Rotor Configurations 10

2.1.2 Hardware 13

2.2 Aerodynamics of a Rotor in Hover 14

2.2.1 Fundamentals of Rotor Aerodynamics 15

2.2.2 Momentum Theory 17

2.2.3 Blade Element Momentum Theory 20

2.2.4 Studies of Full-Scale Rotor Aerodynamics 21

2.2.5 Studies of Micro Rotor Aerodynamics 23

2.2.6 Studies of Fluid Interactions Between a Rotor and a Planar Surface 24

2.3 State and Disturbance Estimation 27

2.3.1 Fundamentals of State Estimation and Kalman Filtering . . . 28

2.3.2 Disturbance Estimation 31
2.3.3 Simultaneous State and Disturbance Estimation 34
2.4 Summary 36

3 Micro Helicopter Hovering Dynamics 39
3.1 Derivation of Micro Helicopter Hovering Dynamics Model 39
3.1.1 Rigid Body Dynamics 40
3.1.2 Stability Derivative Linearisation 42
3.1.3 Rotor Dynamics 44
3.1.4 Complete Hovering Dynamics Model with Exogenous Disturbance Dynamics 47
3.1.5 Output Dynamics 49
3.2 Overview of Micro Helicopter Test-Bed 51
3.2.1 Hardware Modifications 52
3.2.2 Firmware 55
3.2.3 Ground Station 62
3.2.4 Motion Capture System 65
3.3 System Identification of Micro Helicopter Test-Bed Hovering Dynamics 67
3.3.1 Closed Loop Hovering Dynamics 68
3.3.2 Flight Data Collection 70
3.3.3 Frequency Domain Parametric System Identification 73
3.3.4 Validation of Identified Model Parameters 77

4 Computational Fluid Dynamics Method 81
4.1 Fluid Domain and Rotor Geometry 82
4.2 Mesh 82
4.3 Governing Equations 86
4.3.1 Navier-Stokes Equations 86
4.3.2 RANS Equations and Turbulence Modelling 91
4.3.3 Rotating Mesh Model 93
4.3.4 Immersed Boundary Model 93
4.4 Boundary Conditions 96

4.5 CFX Solver 98
4.6 Mesh Independence 99
4.7 Domain Size Independence 100
4.8 Validation Methods 102
4.8.1 Two-Dimensional Free Vortex Model 102
4.8.2 Experimental Validation of Rotor Thrust and Torque 108

5 Validation of Computational Fluid Dynamics Method 117
5.1 Validation of Baseline Results 118
5.1.1 Flow Field 118
5.1.2 Blade Tip Vortex 119
5.1.3 Spanwise Blade Loading 121
5.2 Validation of Near-Ground Results 125
5.2.1 Rotor Thrust 126
5.2.2 Flow Field 129
5.2.3 Blade Tip Vortex 132
5.3 Summary 134

6 Fluid Interactions Between a Hovering Micro Rotor and a Ceiling Plane 137
6.1 Results 138
6.1.1 Rotor Thrust and Power 138
6.1.2 Flow Field 140
6.1.3 Blade Tip Vortex 142
6.1.4 Induced Velocity 146
6.1.5 Local Effective Angle of Attack 149
6.1.6 Blade Pressure Field 150
6.1.7 Spanwise Loading 151
6.2 Discussion 153
6.2.1 Relationship Between Vertical Force Disturbance and Rotor-Ceiling Gap 153
6.2.2 Blade Tip Vortex Interactions With a Ceiling Plane 155

6.2.3 Potential Flow Analysis of Near-Ceiling Flow Field 157
6.2.4 Rotor Efficiency 161
6.2.5 Comparison With Hovering Micro Rotor Fluid Interactions with a Ground Plane 163
6.3 Summary 165

7 Fluid Interactions Between a Hovering Micro Rotor and a Wall Plane 167
7.1 Results 168
7.1.1 Rotor Thrust, Power and Torque 168
7.1.2 Flow Field 175
7.1.3 Blade Tip Vortex 180
7.1.4 Induced Velocity 185
7.1.5 Local Effective Angle of Attack 187
7.1.6 Blade Pressure Field 189
7.1.7 Spanwise Loading 191
7.2 Discussion 194
7.2.1 Relationship Between Torque Disturbances and Rotor-Wall Gap 194
7.2.2 Blade Tip Vortex Interactions With a Wall Plane 198
7.2.3 Potential Flow Analysis of Near-Wall Flow Field 199
7.2.4 Comparison with Near-Ground and Near-Ceiling Fluid Interactions 204
7.3 Summary 206

8 In-Flight Estimation of Aerodynamic Disturbances Induced by Micro Rotor Fluid Interactions with Planar Surfaces 209
8.1 Simultaneous State and Disturbance Estimator 210
8.1.1 Estimator Derivation 211
8.1.2 Estimator Error Dynamics 212
8.1.3 Observability 212
8.1.4 H_∞ Synthesis 213

8.2 Application of Estimator to Micro Helicopter Test-Bed Hovering Dynamics . . . 214
8.2.1 Heave-Yaw Estimator . . . 214
8.2.2 Lateral-Longitudinal Estimator . . . 215
8.3 Flight Test Results . . . 218
8.3.1 Near-Ground Flight Test Results . . . 219
8.3.2 Near-Ceiling Flight Test Results . . . 223
8.3.3 Near-Wall Flight Test Results . . . 226
8.4 Discussion . . . 233
8.4.1 State Estimation Performance . . . 233
8.4.2 Disturbance Estimation Performance . . . 235
8.4.3 Passive Proximity Estimation Performance . . . 236
8.4.4 Further Applications . . . 237
8.5 Summary . . . 238

9 Conclusions and Recommendations for Future Work 241
9.1 Conclusions . . . 241
9.2 Recommendations for Future Work . . . 244

References 247

Appendix A Additional Computational Fluid Dynamics Results 265
A.1 Fluid Interactions Between a Hovering Micro Rotor and a Ground Plane . . . 265
A.1.1 Induced Velocity . . . 265
A.1.2 Local Effective Angle of Attack . . . 266
A.1.3 Blade Pressure Field . . . 267
A.1.4 Spanwise Loading . . . 268
A.1.5 Relationship Between Vertical Force Disturbance and Rotor-Ground Gap . . . 269
A.2 Fluid Interactions Between a Hovering Micro Rotor and a Wall Plane 271
A.2.1 Flow Field . . . 271

Nomenclature

Note that, because this research covers aspects of helicopter dynamics, fluid dynamics and control theory, some symbols are defined multiple times in this thesis. Vector and matrix terms are printed in **boldface** type.

Latin Alphabet Nomenclature

Symbol	**Description**
A	Area
A	Stream function constant
$\boldsymbol{A}$	State matrix
A_1	Swashplate angle about lateral axis
A_b	Lateral flapping/longitudinal flapping stability derivative
A_{lat}	Lateral flapping/lateral cyclic input control derivative
A_{lon}	Lateral flapping/longitudinal cyclic input control derivative
A_{outlet}	Outlet area
A_{rotor}	Rotor disk area
a	Flapping angle about lateral axis
a_x	x-axis accelerometer measurement
a_y	y-axis accelerometer measurement
a_z	z-axis accelerometer measurement
B_1	Swashplate angle about longitudinal axis
B_a	Longitudinal flapping/lateral flapping stability derivative
$\boldsymbol{B_d}$	Disturbance matrix
B_{lat}	Longitudinal flapping/lateral cyclic input control derivative

B_{lon}	Longitudinal flapping/longitudinal cyclic input control derivative
$\boldsymbol{B_u}$	Input matrix
b	Flapping angle about longitudinal axis
$\boldsymbol{C}$	Output matrix
C_c	Near-ceiling induced velocity constant
C_D	Drag coefficient
C_d	Sectional drag coefficient
C_g	Near-ground induced velocity constant
C_L	Lift coefficient
C_l	Sectional lift coefficient
C_P	Power coefficient
C_p	Pressure coefficient
C_Q	Torque coefficient
C_T	Thrust coefficient
c	Blade chord length
D	Drag
$\boldsymbol{D_d}$	Disturbance feed-through matrix
$\boldsymbol{D_f}$	Flapping damping matrix
$\boldsymbol{D_u}$	Input feed-through matrix
d	Sectional drag
$\boldsymbol{d}$	Disturbance vector
$\hat{\boldsymbol{d}}$	Disturbance estimate vector
$\boldsymbol{F}$	Force vector
$\overline{\boldsymbol{F}}$	Exogenous force disturbance vector
$\boldsymbol{F_f}$	Flapping forcing matrix
$\boldsymbol{F_{viscous}}$	Viscous force vector
$F.M.$	Figure of merit
$\boldsymbol{f}$	Body force per unit mass vector
$\boldsymbol{G}$	Process noise input matrix
G_{uu}	Input auto-spectrum
G_{yu}	Input-output cross-spectrum

G_{yy}	Output auto-spectrum
g	Acceleration due to gravity
g_x	x-axis gyroscope measurement
g_y	y-axis gyroscope measurement
g_z	z-axis gyroscope measurement
$g.r.$	Prism layer growth rate
h	Prism layer height
$h1_{domain}$	Domain height above rotor
$h1_{refine1}$	Height above rotor of refinement region 1
$h1_{refine2}$	Height above rotor of refinement region 2
$h2_{domain}$	Domain height below rotor
$h2_{refine1}$	Height below rotor of refinement region 1
$h2_{refine2}$	Height below rotor of refinement region 2
h_c	Rotor-ceiling gap
h_g	Rotor-ground gap
h_w	Rotor-wall gap
J	Moment of inertia
$\boldsymbol{J}$	Inertial tensor
J_β	Blade moment of inertia (about flapping axis)
$\boldsymbol{K}$	Gain matrix
$\boldsymbol{K_f}$	Flapping stiffness matrix
K_I	Integral gain
K_m	Mesh refinement factor
K_P	Proportional gain
k	Time step count
k	Number of vortices in 2D FV model
k_β	Blade stiffness
L	Lift
L	Moment about x-axis
$\overline{L}$	Exogenous torque disturbance about x-axis
L_b	x moment/lateral flapping stability derivative

$\boldsymbol{L_d}$	Disturbance estimator gain matrix
L_u	x moment/x velocity stability derivative
L_v	x moment/y velocity stability derivative
L_w	x moment/z velocity stability derivative
$\boldsymbol{L_x}$	State estimator gain matrix
l	Sectional lift
M	Moment about y-axis
$\boldsymbol{M}$	Moment vector
$\overline{M}$	Exogenous torque disturbance about y-axis
$\overline{\boldsymbol{M}}$	Exogenous torque disturbance vector
M_a	y moment/longitudinal flapping stability derivative
$\boldsymbol{M}_{immersed}$	Immersed momentum source vector
$\boldsymbol{M}_{rotating}$	Rotating momentum source vector
M_u	y moment/x velocity stability derivative
M_v	y moment/y velocity stability derivative
M_w	y moment/z velocity stability derivative
m	Mass
m	Number of inputs
$\dot{m}$	Mass flow rate
$\dot{m}_{rotor}$	Mass flow rate through rotor disk
N	Moment about z-axis
N	Number of mesh elements
$\overline{N}$	Exogenous torque disturbance about z-axis
N_b	Number of blades
N_{col}	z moment/collective input control derivative
N_r	z moment/z angular velocity stability derivative
N_w	z moment/z velocity stability derivative
N_{yaw}	z moment/yaw input control derivative
n	Number of states
P	Power
P'	Baseline power

p	Pressure
p	Number of measured outputs
p	Roll-rate (angular velocity about x-axis)
Q	Torque about z-axis
$\boldsymbol{Q}$	Process noise covariance matrix
Q'	Baseline torque about z-axis
Q_x	Torque about x-axis
Q_y	Torque about y-axis
q	Pitch-rate (angular velocity about y-axis)
q	Number of exogenous disturbances
R	Rotor radius
$\boldsymbol{R}$	Measurement noise covariance matrix
R_{domain}	Domain radius
$R_{refine1,inner}$	Inner radius of refinement region 1
$R_{refine1,outer}$	Outer radius of refinement region 1
$R_{refine2}$	Radius of refinement region 1
Re	Reynolds number
r	Yaw-rate (angular velocity about z-axis)
r	Radial distance
$\boldsymbol{r}$	Position vector of element within domain
r_c	Vortex core radius
r_{CoD}	Radial distance to centre of drag
r_{col}	Reference collective pitch input
r_{lat}	Reference lateral cyclic pitch input
r_{lon}	Reference longitudinal cyclic pitch input
r_{thr}	Reference throttle input
r_{yaw}	Reference yaw input
S	Mean strain
$\mathcal{S}$	Control surface
T	Thrust
T'	Baseline thrust

t	Time
u	Velocity in x direction
$\boldsymbol{u}$	Input vector
u_{col}	Collective pitch input
u_{lat}	Lateral cyclic pitch input
u_{lon}	Longitudinal cyclic pitch
u_{thr}	Throttle input
u_{yaw}	Yaw input
V	Volume
$\mathcal{V}$	Finite control volume
$\boldsymbol{V}$	Flow velocity vector
$\overline{\boldsymbol{V}}$	Average flow velocity vector
$\overline{\boldsymbol{V}}_{abs}$	Average flow velocity vector in global reference frame
$\boldsymbol{V}_{immersed}$	Immersed boundary velocity vector
v	Velocity
v	Velocity in y direction
$\boldsymbol{v}$	Velocity vector
$\overline{\boldsymbol{v}}$	Fluctuating flow velocity vector
v_∞	Far wake velocity
v_i	Induced velocity
v_{inc}	Incident velocity
v_{tip}	Blade tip velocity
W_{in}	Inlet velocity
w	Velocity in z direction
X	Force in x direction
$\overline{X}$	Exogenous force disturbance in x direction
X_a	x force/longitudinal flapping stability derivative
X_u	x force/x velocity stability derivative
x	Average mesh element dimension
$\boldsymbol{x}$	State vector
$\hat{\boldsymbol{x}}$	State estimate vector

Y	Force in y direction
$\overline{Y}$	Exogenous force disturbance in y direction
Y_b	y force/lateral flapping stability derivative
Y_v	y force/y velocity stability derivative
$\boldsymbol{y}$	Output vector
Z	Force in z direction
$\overline{Z}$	Exogenous force disturbance in z direction
Z_a	z force/longitudinal flapping stability derivative
Z_b	z force/lateral flapping stability derivative
Z_{col}	z force/collective input control derivative
Z_w	z force/z velocity stability derivative
Z_r	z force/z angular velocity stability derivative
z	Vertical distance
$\boldsymbol{z}$	Augmented state vector

Greek Alphabet Nomenclature

Symbol	**Description**
α	Angle of attack
α_c	Passive ceiling proximity estimate constant
α_e	Effective angle of attack
α_g	Passive ground proximity estimate constant
α_w	Passive wall proximity estimate constant
β_0	Coning angle
Γ	Circulation
γ	Lock number
γ_{yu}^2	Magnitude squared coherence
δ_{col}	Collective pitch input (difference from equilibrium value)
δ_{lat}	Lateral cyclic pitch input (difference from equilibrium value)
δ_{lon}	Longitudinal cyclic pitch input (difference from equilibrium value)
δ_{yaw}	Yaw input (difference from equilibrium value)

ζ	Damping ratio
ζ	Wake age
$\boldsymbol{\Theta}$	Attitude/heading vector
θ	Pitch angle (rotation about y-axis)
$\hat{\theta}_{\text{acc}}$	Pitch angle estimate from accelerometer measurement
$\hat{\theta}_{\text{gyr}}$	Pitch angle estimate from gyroscope measurement
μ	Coefficient of viscosity
ν	Kinematic viscosity
ν_t	Turbulent eddy viscosity
π	Pi
ρ	Fluid density
σ	Standard deviation
τ	Stress
$\boldsymbol{\tau}$	Stress tensor
τ_f	Flapping time constant
Φ	Solution used for Richardson extrapolation
ϕ	Roll angle (rotation about x-axis)
$\hat{\phi}_{\text{acc}}$	Roll angle estimate from accelerometer measurement
$\hat{\phi}_{\text{gyr}}$	Roll angle estimate from gyroscope measurement
ϕ_w	Rotor-wall angle
ψ	Stream function
ψ	Yaw angle (rotation about z-axis)
ψ_w	Helicopter-wall angle
Ω	Rotor speed
$\boldsymbol{\omega}$	Angular velocity vector
ω_1	Chirp start frequency
ω_2	Chirp stop frequency
ω_c	Complementary filter cut-off frequency
ω_n	Natural frequency

Abbreviations

Abbreviation	Description
2D	Two Dimensional
3D	Three Dimensional
BEMT	Blade Element Momentum Theory
BIBO	Bounded-Input Bounded-Output
CCPM	Collective-Cyclic Pitch Mixing
CFD	Computational Fluid Dynamics
DARPA	Defense Advanced Research Projects Agency
DC	Direct Current
DNS	Direct Numerical Simulation
DOF	Degrees of Freedom
DPIV	Digital Particle Image Velocimetry
EKF	Extended Kalman Filter
ESO	Extended State Observer
FPS	Frames Per Second
FV	Free Vortex
GINA	Guidance and Inertial Navigation Assistant
GPS	Global Positioning System
HPC	High Performance Computing
IMU	Inertial Measurement Unit
LED	Light Emitting Diode
LHP	Left Half Plane
LQG	Linear Quadratic Gaussian

MAV	Micro Aerial Vehicle
MEMS	Microelectromechanical System
MIMO	Multi-Input Multi-Output
MOSFET	Metal-Oxide Semiconductor Field-Effect Transistor
NACA	National Advisory Committee for Aeronautics
PEM	Prediction Error Method
PWM	Pulse Width Modulation
RANS	Reynolds-Averaged Navier-Stokes
RHP	Right Half Plane
RMS	Root Mean Square
TPP	Tip Path Plane
UAV	Unmanned Aerial Vehicle
UKF	Unscented Kalman Filter
USB	Universal Serial Bus

Chapter 1

Introduction

Since Leonardo da Vinci first conceived of his *aerial screw* in 1483, humankind has dreamt of rotor-craft capable of lifting from the ground and hovering. With the rapid development of the internal combustion engine in the late 19th and early 20th centuries, da Vinci's ideas began to inspire a range of early attempts at helicopter flight. Although cause for some debate, the first successful helicopter flight is generally considered to have occurred in 1907, when Paul Cornu hovered 1 foot above the ground for 20 seconds in a home-built dual-rotor helicopter (Leishman and Johnson, 2009). This flight, and the other early attempts that followed, spurred on the rapid development of helicopter technology. By the early 1960s, helicopters such as the Sikorsky S-55, Bell Jet-Ranger and the UH-1 Huey were in mass production (Leishman, 2006). These helicopters were often favoured over fixed-wing aircraft for carrying out missions that required precise flight manoeuvres or hovering over a fixed position. Today, the use of rotor-craft, including helicopters and multi-rotors, has grown widespread in applications such as search and rescue, reconnaissance, military and civilian transport, surveillance, crop spraying and videography.

More recently, advances in micro scale sensor and actuator technologies have made it possible to shrink rotor-craft systems down to a micro scale[1]. Owing to their hovering capability and manoeuvrability, micro rotor-craft are well suited to search and rescue (Chen and McKerrow, 2007), reconnaissance (McCalmont

[1]There is no strict definition of micro rotor-craft size. The Defense Advanced Research Projects Agency (DARPA) suggests that a micro aerial vehicle should have a maximum dimension of less than 6" (152 mm) (Bohorquez et al., 2003a).

et al., 2007), remote inspection (Irizarry et al., 2012), and aerial photography and videography applications (Natalizio et al., 2013). Further to this, their small size allows them to operate within confined or cluttered urban or indoor environments that are otherwise inaccessible to larger aircraft (Koehl et al., 2012). A micro rotorcraft operating in a confined environment will be subject to disturbances induced by aerodynamic proximity effects. Such disturbances are likely to adversely affect stability and performance. The physical nature of confined environment aerodynamic disturbances acting on a micro helicopter is the focus of the research outlined in this thesis.

1.1 Challenges Facing Micro Helicopters in Confined Environments

The main advantage of micro helicopters over larger aircraft and ground robots is that they are small enough to access confined environments such as small windows and doors, air ducts, narrow corridors, collapsed spaces and between buildings. By definition, operation within such confined environments will require micro helicopters to fly in close proximity to obstacles. This will result in aerodynamic disturbances due to fluid interactions that occur between rotors and nearby obstacles. With the exception of fluid interactions between a micro rotor and a ground plane (Lee et al., 2010; Lakshminarayan et al., 2013; Kalra, 2014), fluid interactions between hovering micro rotors and nearby obstacles are poorly understood. This is largely due to the fact that the bulk of helicopter aerodynamics studies in the existing literature are concerned with full-scale helicopters. Because full-scale helicopters are typically prohibited from operating in close proximity to obstacles, there has previously been little motivation for investigation of full-scale rotor proximity effects. Further to this, micro rotors operate at significantly lower Reynolds numbers (Leishman, 2006) than full-scale rotors. This means that full-scale rotor studies have limited applicability to micro rotors because the scaling of micro rotor viscous effects with Reynolds number is not well studied. Therefore, it is clear that further research is required in order to understand the full range of fluid phenomena that micro helicopters are

likely to encounter.

Additionally, because micro helicopters have very small inertia, disturbances induced by aerodynamic proximity effects are likely to have a significant adverse effect on helicopter performance. These disturbances must be estimated and compensated for during flight in order to maintain stable control of a micro helicopter. Disturbance estimation (also referred to as disturbance observation) is a well studied subject of control theory. In principle, disturbance estimation can be used to estimate disturbances induced by aerodynamic proximity effects, however, doing so relies on having access to accurate estimates of the helicopter's position and velocity. Position and velocity estimates are typically obtained from measurements provided by a Global Positioning System (GPS) with inertial sensors, or a motion capture camera system. In practice, confined environments are likely to deny GPS access and motion capture camera systems are only feasible in controlled laboratory and manufacturing environments. As such, a micro helicopter is not likely to have access to accurate estimates of position and velocity when carrying out a mission in a confined GPS-denied environment. This places micro helicopters in an especially vulnerable position because they are susceptible to disturbances induced by aerodynamic proximity effects and also lack the sensing capability to accurately detect and estimate proximity to obstacles. With this in mind, it is clear that the existing body of disturbance estimation research must be extended in order to estimate aerodynamic proximity effect disturbances using only measurements provided by a helicopter's on-board inertial sensors.

1.2 Objectives and Scope

The first major objective of the research outlined in this thesis is to investigate the fluid interactions that occur between a hovering micro rotor and nearby planar surfaces. Specifically, this research focuses on fluid interactions between a micro rotor and a horizontal ceiling plane and a vertical wall plane. Fluid interactions between a hovering rotor and a horizontal ground plane will also be investigated in order to validate the methods used in this research against results from the existing literature. For the benefit of the reader, qualitative representations of the subtle

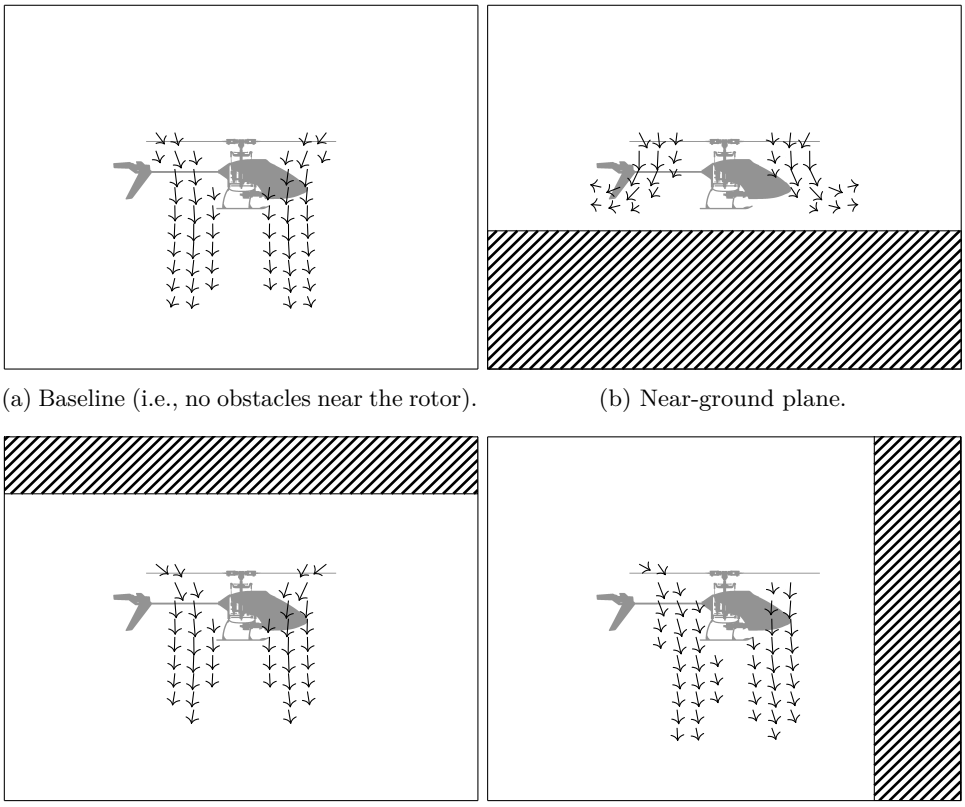

(a) Baseline (i.e., no obstacles near the rotor).

(b) Near-ground plane.

(c) Near-ceiling plane.

(d) Near-wall plane.

Figure 1.1: Qualitative schematic of flow velocity vectors through a micro rotor in close proximity to planar surfaces.

effects that ground, ceiling and wall planes can have on the flow field through a micro rotor are provided in Figure 1.1. Ground, ceiling and wall planes have been chosen as the focus of this study because they are considered to be the most common obstacles that a micro helicopter will encounter. This research aims to identify how fluid interactions with these planar surfaces distorts the wake downstream of a micro rotor. Additionally, this research aims to characterise the relationship between disturbances induced by aerodynamic proximity effects and proximity to the planar surface that is inducing the disturbance. Fluid interactions between a micro rotor and inclined, curved and irregular shaped surfaces are beyond the scope of this research.

The second major objective of this research is to estimate the disturbances acting on a micro helicopter due to aerodynamic proximity effects during flight. In order to estimate these disturbances in confined GPS-denied environments, this research aims

to estimate disturbances using only measurements provided by a micro helicopter's on-board inertial sensors (i.e., acceleration and angular rate measurements obtained from microelectromechanical system (MEMS) accelerometer and gyroscope sensors). Additionally, this research aims to show that the disturbance estimate, along with *a priori* knowledge of how the disturbance varies with proximity, can be used to passively estimate proximity to planar surfaces. This will be a significant development as it will mitigate the need for accommodating additional proximity sensors on-board a micro helicopter where power and payload capacity is already constrained. Note that implementation of disturbance estimator based control systems for compensation of disturbances induced by aerodynamic proximity effects is beyond the scope of this research.

1.3 Contributions of this Thesis

This thesis will show that the vortex wake downstream of a micro helicopter rotor will interact with nearby obstacles due to viscous action of the fluid and boundary layer effects near the obstacle. These fluid interactions will disrupt the rotor wake which will, in turn, generate a disturbance acting on the helicopter. This thesis extends the existing body of helicopter aerodynamics research by using a computational method (outlined in Chapter 4) to investigate the fluid interactions that occur between a micro rotor and a ceiling plane or wall plane. The computational method is validated by comparison against experimental results, fluid dynamics theory and results from the existing literature. The results presented in this thesis show that rotor thrust and efficiency both increase as proximity to a ceiling plane decreases. Additionally, as proximity to a wall plane decreases, a micro rotor will experience a significant torque disturbance about the horizontal axis parallel to the wall. The fundamental fluid dynamics that drive these proximity effect disturbances are explained by analysing the flow field through the rotor disk, vortex structures in the wake and loading across the blade span.

Further to this, the disturbances generated by aerodynamic proximity effects can have an adverse effect on helicopter performance. If uncompensated for, these disturbances may destabilise the helicopter and, in the worst case, cause the helicopter

to collide with the obstacle that is inducing the disturbance. To compensate for such disturbances, it is desirable to estimate the magnitude of the disturbances generated by aerodynamic proximity effects. With this in mind, this thesis postulates a linear simultaneous state and disturbance estimation scheme that relies only on knowledge of control inputs provided to the helicopter and measurements provided by on-board inertial sensors. The estimator accounts for direct feed-through of exogenous disturbances to measured outputs and is tuned optimally using H_∞ synthesis. Experimental flight tests show that the estimation scheme can provide a fair estimate of the aerodynamic disturbances induced by proximity to a ground plane, ceiling plane or wall plane.

Finally, this thesis will show that estimates of disturbances induced by aerodynamic proximity effects can be used to passively estimate proximity to a ground plane, ceiling plane and wall plane. This is achieved by using the disturbance estimate, as well as *a priori* knowledge of how the disturbance varies with proximity to the planar surface to infer proximity to the surface. This result is a significant contribution to the field of micro helicopters as it demonstrates the feasibility of obstacle detection using only on-board inertial sensors. Use of this passive proximity estimation scheme will mitigate the need for accommodating additional exteroceptive proximity sensors on-board a micro helicopter. This will free-up power, payload and computation capacity, allowing micro helicopters to be more effective at carrying out missions within confined environments.

1.4 Overview of Thesis Structure

This thesis begins with a comprehensive overview of the relevant literature in Chapter 2. This includes an overview of micro rotor-craft configurations and hardware; a review of the fundamentals of hovering rotor aerodynamics and numerical and experimental studies of full-scale and micro-scale rotor fluid dynamics; and a review of state and disturbance estimation methods. In Chapter 3, the micro helicopter test-bed used in this research is outlined in detail, including: an overview of the test-bed's software, firmware and hardware and a derivation of the test-bed's hovering dynamics. The computational fluid dynamics (CFD) method used to investigate micro rotor

fluid interactions between a hovering micro rotor and planar surfaces is outlined in Chapter 4. A comprehensive validation of the CFD method by comparison against fluid dynamics theory, experimental results and results from the literature is provided in Chapter 5. CFD results for ceiling plane and wall plane fluid interactions are provided in Chapters 6 and 7 respectively. The effect of these fluid interactions on rotor thrust and power are presented, along with a comprehensive analysis of the flow field, blade tip vortex, blade pressure field and blade loading. An overview of the disturbance estimation scheme developed as a part of this research is provided in Chapter 8, along with experimental results. Finally, concluding remarks and recommendations for future work are made in Chapter 9.

Chapter 2

Background and Literature Review

This chapter provides an overview of micro rotor-craft configurations and introduces the fundamental theory behind rotor aerodynamics. Additionally, it provides an overview of existing literature relating to micro rotor-craft, micro rotor fluid dynamics and state and disturbance estimation techniques that have been applied to micro aerial vehicles (MAVs).

2.1 Micro Rotor-Craft Flight Vehicles

Micro rotor-craft[1] are a class of MAV that utilise rotary wings to generate lift. Micro rotor-craft are well suited to applications where hovering and precise manoeuvring are required; they can be controlled in six degrees of freedom (DOF) and can yaw, pitch and roll independently, as illustrated in Figure 2.1. Their small size and low cost have allowed researchers, developers and hobbyists to conceive a wide range of different rotor configurations, utilising a range of different types of hardware. This thesis focuses specifically on single main rotor/tail rotor micro rotor-craft, i.e., a conventional helicopter configuration. Nonetheless, an overview of different types of micro rotor-craft configurations and hardware is provided in this section for the

[1] Micro rotor-craft are also commonly referred to in the literature as rotary wing micro aerial vehicles.

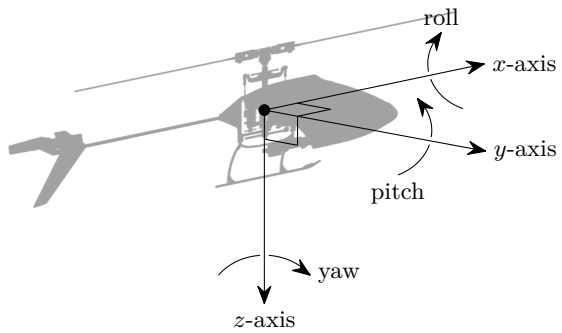

Figure 2.1: Schematic showing the roll, pitch and yaw axes for a micro helicopter.

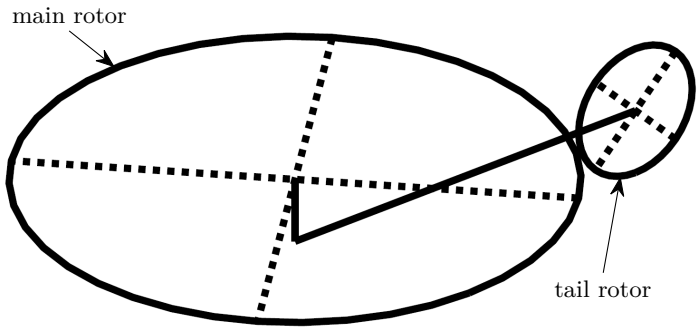

Figure 2.2: Single main rotor helicopter configuration. The tail rotor is required to balance the torque generated by the main rotor about the vertical axis.

benefit of the reader.

2.1.1 Rotor Configurations

The three most commonly used and well understood micro rotor-craft configurations are: single main rotor (with tail rotor); coaxial rotor; and quad rotor. Schematics showing the differences between these configurations are provided in Figures 2.2, 2.3 and 2.4 respectively.

Single rotor helicopters (Conroy et al., 2011) are configured with one large main rotor and one smaller tail rotor. Thrust is generated by varying main rotor speed or blade collective pitch; roll and pitch motion is achieved by varying cyclic pitch; and yaw motion is achieved with the use of the tail rotor. Coaxial helicopters (Bohorquez and Pines, 2003; Schafroth, 2010) are configured with two coaxial counter-rotating

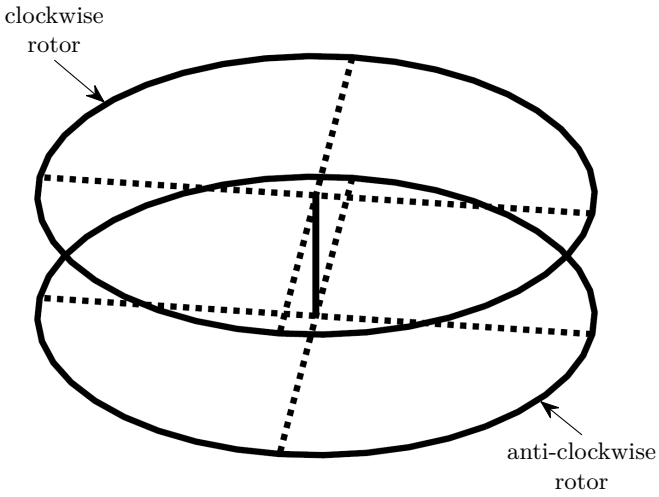

FIGURE 2.3: Coaxial rotor helicopter configuration. The rotors counter-rotate in order to balance out the torque about the vertical axis.

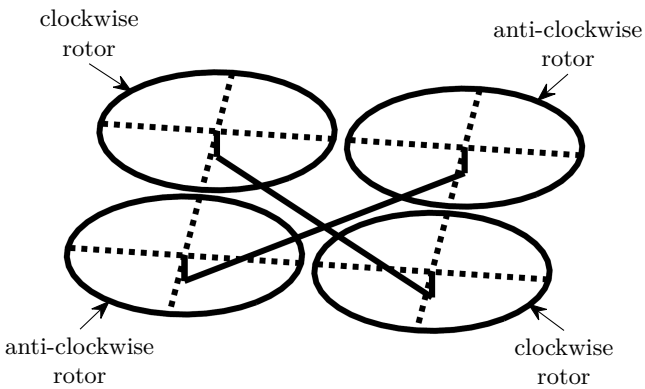

FIGURE 2.4: Quad rotor helicopter configuration. Two rotors spin clockwise and two rotors spin anti clockwise in order to balance out torque about the vertical axis.

rotors. Thrust is generated by varying rotor speed or blade pitch; roll and pitch motion is achieved using a cyclic pitch rotor head assembly; and yaw motion is achieved by offsetting the top and bottom rotor blade speeds. Many single main rotor and coaxial rotor micro helicopters also utilise a stabiliser bar to slow down pitch and roll response (Mettler et al., 2002); this makes the helicopter more stable and easier to pilot. Quad rotors (Cutler et al., 2011; Kumar and Michael, 2012) consist of four independently controlled rotors, typically arranged in a cross shape. Stability of the quad rotor is maintained by independently controlling the speed of each of the four rotors. Note that this requires high frequency control responses and thus cannot be achieved by a human pilot; as such, an on-board attitude control

Table 2.1: Summary of micro rotor-craft test-beds.

Developer	Configuration	Blade pitch	Rotor diameter (mm)	Mass (g)
University of Maryland (Bohorquez et al., 2003a)	coaxial	fixed	140	100
ETHZ Autonomous Systems Lab (Schafroth et al., 2010b)	coaxial	fixed	175	80
University of Maryland (Conroy et al., 2011)	single rotor	fixed	505	390
MIT Aerospace Controls Lab (Cutler et al., 2011)	quad rotor	variable	230	462
UPenn GRASP Lab (Kumar and Michael, 2012)	quad rotor	fixed	210	73

system is required to stabilise a quad rotor. The quad rotor configuration can also be extended to accommodate additional rotors (typically referred to as multi rotor configurations). For the benefit of the reader, a summary of several successful and well documented micro rotor-craft test-beds is provided in Table 2.1.

There is little consensus amongst researchers as to which is the *best* configuration as each has its own associated advantages and disadvantages. The research outlined in this thesis focuses on single rotor micro helicopters (i.e., a single main rotor and a single tail rotor). This configuration has been chosen because it allows for the use of a variable pitch rotor which provides faster response times than fixed pitch rotors (conventionally used by coaxial and quad rotor micro helicopters). Additionally, the interactions between a main rotor and a smaller tail rotor are relatively weak and are often neglected in aerodynamic analysis of single rotor micro helicopters. In contrast, coaxial and quad rotor configurations generate rotor interactions that are relatively more significant and cannot readily be neglected from aerodynamic

analysis.

2.1.2 Hardware

Due to their small size, limited payload capacity and limited battery life, micro rotor-craft are very limited in terms of the electronic hardware that they are able to accommodate. Because of this, micro rotor-craft designers and developers must carefully select hardware in order to ensure that good sensor, computer and actuator performance is achieved without compromising payload capacity or battery life (Soundararaj et al., 2009).

Most micro rotor-craft on-board inertial navigation is performed with the aid of MEMS inertial measurement units (IMUs). Grauer et al. (2009), Conroy et al. (2011) and Mukherjee and Waslander (2011) have all implemented micro rotor-craft IMUs that utilise on-board MEMS magnetometer, gyroscope and accelerometer sensors. Such systems fulfil the weight and power requirements of MAVs, however, they typically provide poor accuracy because they are susceptible to time-varying biases and drifts as well as noise induced by interference from direct current (DC) motors and servos (Grauer et al., 2009). To a certain extent, this can be addressed using state estimation methods (a review of which is provided in Section 2.3.1), however, numerous researchers have sought to improve measurement accuracy by using additional sensors, including: ultrasonic sensors (Schafroth et al., 2010a); pressure sensors (Fankhauser et al., 2011); and GPS (Mukherjee and Waslander, 2011). While these sensors are able to provide more accurate estimates of micro rotor-craft states, accommodating them on-board a micro rotor-craft will reduce battery life and payload capacity. Note also that GPS is not likely to be feasible when operating within a confined environment due to obstacles denying GPS signals. Another approach is to use an external motion capture system to augment, or instead of, on-board sensors. Grauer et al. (2009) compared the performance of on-board IMU measurement with external motion capture measurement (using only six cameras) and found that the motion capture system provided less noisy state estimates and yielded more accurate modelling results. Motion capture is especially useful for collecting flight data for the purposes of system identification or testing of

advanced control systems, however, it should be noted that controllers that rely on real time motion capture data have only a limited applicability as they cannot be implemented outside of a laboratory environment. With this in mind, this research will focus on utilising MEMS inertial sensors only in order to ensure that sensing performance will be guaranteed in confined unknown environments and to maximise battery life and payload capacity.

Micro rotor-craft typically utilise micro scale brushed DC motors and servo motors to turn rotors and actuate collective and/or cyclic pitch rotor-head assemblies (Mukherjee and Waslander, 2011; Fankhauser et al., 2011; Schafroth et al., 2010a; Limnaios and Tsourveloudis, 2012). Other electronics commonly used on-board micro rotor-craft include: computational resources, such as the dsPIC micro processor (Limnaios and Tsourveloudis, 2012), for implementing control architectures; and wireless transceivers, such as the Zigby Bluetooth module (Fankhauser et al., 2011), for communication with ground station computers or other aircraft. Typically, the combined mass of motors, servo motors and other required electronics will fit within a micro rotor-craft's payload capacity. However, this hardware rapidly consumes the limited power available and, therefore, micro rotor-craft are commonly unable to operate for longer than approximately 5–10 minutes before battery charging is required (Schafroth, 2010).

2.2 Aerodynamics of a Rotor in Hover

As outlined in Chapter 1, the primary objective of this research is to investigate the disturbances that are induced by fluid interactions between a hovering micro rotor and nearby planar surfaces. This scenario is of particular interest because micro helicopters are likely to encounter planar surfaces (as well as irregular shaped obstacles) when operating within a confined environment. In this section, a review of the fundamentals of hovering rotor aerodynamics is provided along with a review of numerical and experimental studies of full-scale and micro-scale rotor fluid dynamics.

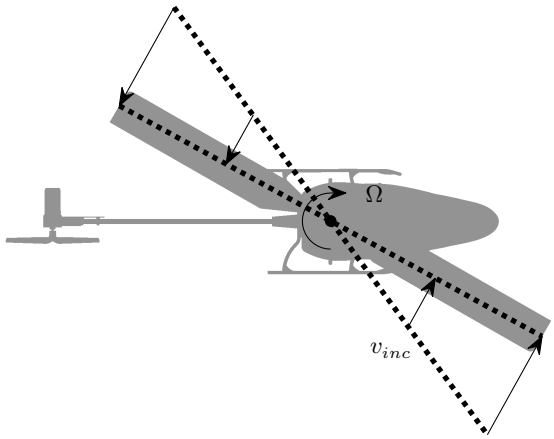

FIGURE 2.5: Schematic showing incident flow velocity at rotor, where Ω and v_{inc} are the angular velocity of the rotor and incident flow velocity respectively.

2.2.1 Fundamentals of Rotor Aerodynamics

In principle, a rotor blade (or a propeller or turbine blade) can be considered as a rotating wing. The rotation of the rotor blade induces an incident flow velocity over each blade. As illustrated in Figure 2.5, the incident velocity, v_{inc}, varies linearly along the blade span and can be calculated from

$$v_{inc} = \Omega r, \tag{2.1}$$

where Ω and r are the angular velocity of the rotor and radial distance measured from the rotor hub respectively. The incident flow velocity is zero at the rotor hub. The peak incident velocity, v_{tip}, occurs at the blade tip and can be calculated from

$$v_{tip} = \Omega R, \tag{2.2}$$

where R is the rotor radius.

Reynolds number, Re, for a helicopter rotor is typically defined using the blade tip velocity and blade chord length

$$Re = \frac{v_{tip} c}{\nu}, \tag{2.3}$$

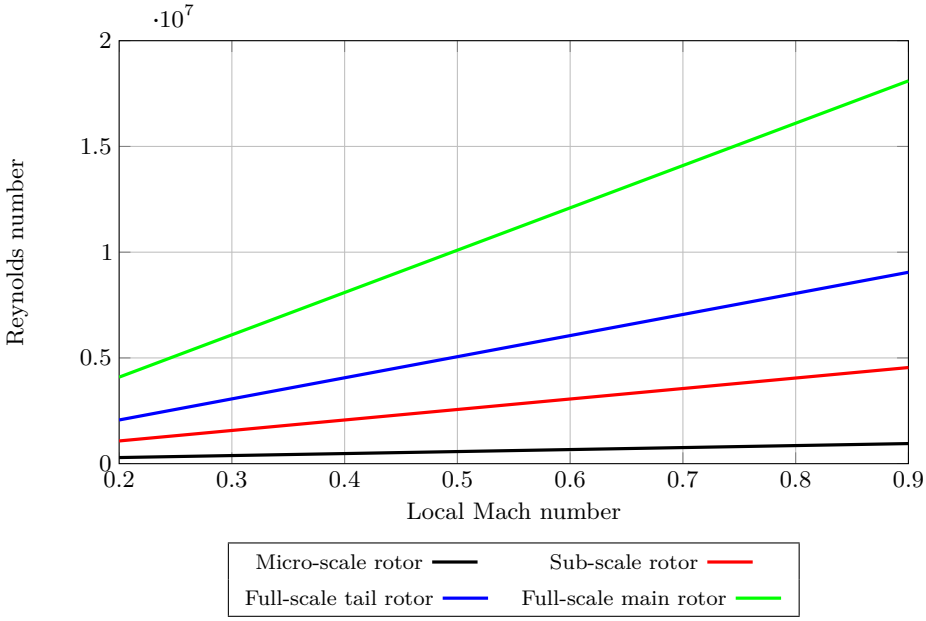

Figure 2.6: Variation of Reynolds number with local Mach number for micro-scale, sub-scale and full-scale main and tail rotors.

where c and ν are the blade chord length and kinematic viscosity respectively. Reynolds number is a useful measure of the ratio between fluid body forces and viscous forces and will be referred to extensively in this thesis. For full-scale rotors, Reynolds numbers are typically in the range of $10^6 < Re < 10^7$ (Leishman, 2006), while micro-scale rotor Reynolds numbers are typically in the range of $10^3 < Re < 10^5$ (Lakshminarayan and Baeder, 2010a). A graphical summary of typical Reynolds number ranges for full-scale, sub-scale and micro-scale rotors is provided in Figure 2.6 (obtained from data published by Leishman (2006)). Note that full-scale, sub-scale and micro scale rotors typically have a radius of 1 – 20 m, 0.25 - 1 m and under 0.25 m respectively (Lakshminarayan, 2009). Due to their low Reynolds number, micro helicopters are likely to suffer from poorer lift and drag performance due to an increased dominance of viscous effects (Lissaman, 1983; Selig et al., 1995). The effect of viscosity on rotor performance is discussed further in Section 2.2.5.

The high incident velocity experienced toward the blade tip induces high dynamic pressures. This causes vortical structures trailing from the blade to roll up into a concentrated blade tip vortex (Landgrebe, 1972). The blade tip vortex forms a helical structure in the wake downstream of the rotor. Blade tip vortices move

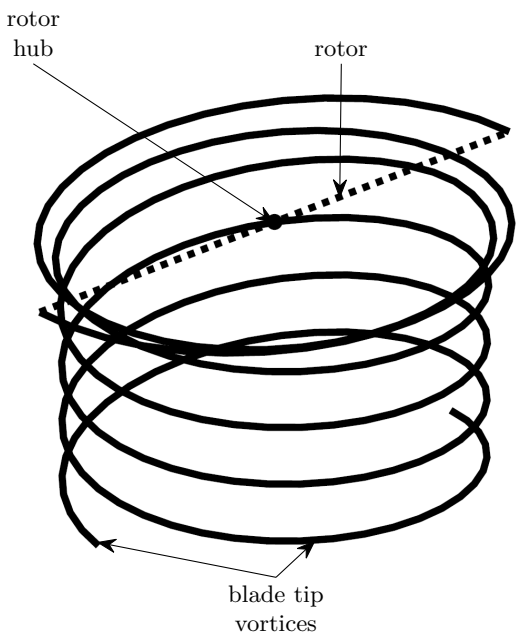

FIGURE 2.7: Schematic showing the helical structure of the blade tip vortices shed from a helicopter rotor. The vortices move inward and downward as they are convected through the wake downstream of the rotor.

inward radially and downward vertically as they are convected through the rotor wake. A schematic showing the general helical structure of the blade tip vortex is provided in Figure 2.7. Free vortex (FV) model analysis by Leishman et al. (2002) indicates that the structure of the blade tip vortex can deform significantly due to translation of the helicopter or due to fluid interactions between the blade tip vortex and a ground plane. The structure of the blade tip vortex is of particular interest because the induced velocity field at the blade is directly affected by circulation throughout the blade tip vortex; therefore, any deformation of the wake due to fluid-structure interactions will alter the induced velocity (and hence the lift and drag forces) at the rotor. The structure of the blade tip vortex is discussed in further detail in Sections 2.2.4 and 2.2.5.

2.2.2 Momentum Theory

The vortex structures within a rotor wake are complex to model or visualise experimentally. Because of this, early helicopter rotor research focussed on using simplified techniques to analyse rotor performance. For example, a simplified fundamental

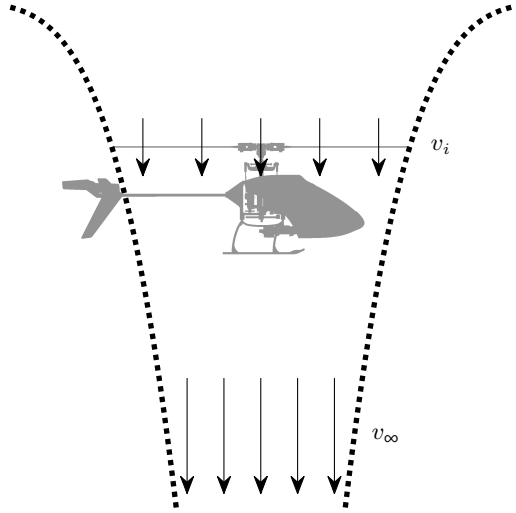

Figure 2.8: Momentum theory flow model, where v_i and v_∞ are the induced velocity through the rotor disk and the velocity in the far wake respectively. The arrows represent velocity vectors and the dashed lines represents the wake slipstream boundary. Flow outside the wake slipstream boundary is assumed to be quiescent.

understanding of rotor thrust and power can be obtained using Rankine-Froude momentum theory (Rankine, 1865; Froude, 1878). Momentum theory involves application of the laws of conservation of mass, momentum and energy to a quasi one-dimensional control volume about a rotor. The rotor is represented by an infinitesimally thin *actuator disk*. A pressure drop over the actuator disk produces the thrust acting at the rotor. The actuator disk imparts kinetic energy to the flow downstream of the rotor; the rate that this energy is imparted is the rotor power. Momentum theory was first postulated by Rankine (1865) for analysing thrust and power provided by marine propellers. Further developments were made by Froude (1878) and momentum theory was more formally generalised by Glauert (1935). It shows that the induced velocity through the rotor disk, v_i, is half the induced velocity in the far wake, v_∞, and that the cross sectional area of the far wake is half the area of the rotor disk. A schematic of this is provided in Figure 2.8.

By using the assumption of quasi one-dimensional flow through the control volume, the rotor thrust, T, and rotor power, P, can be obtained from

$$T = 2\rho A_{rotor} v_i^2,$$
$$P = 2\rho A_{rotor} v_i^3, \tag{2.4}$$

where A_{rotor} and ρ are the area of the rotor/actuator disk and fluid density respectively. A comprehensive derivation of Equation (2.4) can be found in Leishman (2006) and Johnson (1980). Thrust and power are typically non-dimensionalised to obtain the thrust coefficient, C_T

$$C_T = \frac{T}{1/2\rho\Omega^2 R^2 A_{rotor}}, \tag{2.5}$$

and the power coefficient, C_P

$$C_P = \frac{P}{1/2\rho\Omega^3 R^3 A_{rotor}}. \tag{2.6}$$

Note that, because power is directly proportional to torque about the vertical axis ($P = \Omega Q$), power coefficient is equivalent to torque coefficient, C_Q, where

$$C_Q = \frac{Q}{1/2\rho\Omega^2 R^3 A_{rotor}} \equiv C_P, \tag{2.7}$$

where Q is the torque generated by the rotor about the vertical axis. C_T, C_P and C_Q will be referred to extensively throughout this thesis as a measure of rotor performance. Note that North American studies typically omit the $1/2$ from the denominator in Equations (2.5), (2.6) and (2.7) (Leishman, 2006).

Despite the simplified nature of momentum theory, Leishman (2006) notes that it can still provide many useful insights into rotor performance. From Equation (2.4) it is clear that rotor thrust increases with the square of velocity while rotor power increases with the cube of velocity. In order to maximise rotor efficiency, it is desirable to minimise rotor power by minimising induced velocity. This is typically achieved by reducing the mass flow rate through the rotor disk by increasing the rotor radius. For micro rotors, increasing the rotor radius is often not feasible. Therefore, momentum theory shows that micro rotors are likely to have poor power performance when compared with large size rotors. Although outside the scope of this research, momentum theory can also be extended to the case of ascending and descending helicopters (Leishman, 2006).

2.2.3 Blade Element Momentum Theory

Momentum theory can be extended to account for variations in loading across the blade span by using blade element momentum theory (BEMT) (Gustafson and Gessow, 1946). This method considers a two dimensional cross section through the blade, referred to as a *blade element*, as shown in Figure 2.9. Here, the free-stream incident velocity, v_{inc}, varies across the blade span according to Equation (2.1). The effective angle of attack, α_e, along the blade span can be calculated from

$$\alpha_e = \alpha - \arctan\left(\frac{v_i}{v_{inc}}\right), \tag{2.8}$$

where α is the angle of attack of the blade. Induced velocity is determined using momentum theory. From Equation (2.8) it is clear that increasing the induced velocity will, in fact, reduce the effective angle of attack of the blade. The sectional lift and drag force can then be calculated from

$$\begin{aligned} l &= C_l\left(\alpha_e\right)\frac{1}{2}\rho v^2 c, \\ d &= C_d\left(\alpha_e\right)\frac{1}{2}\rho v^2 c, \end{aligned} \tag{2.9}$$

where l, d, C_l, C_d and v are lift per unit span, drag per unit span, sectional lift coefficient, sectional drag coefficient and flow velocity respectively. The flow velocity is the magnitude of the free-stream incident velocity and induced velocity

$$v = \sqrt{v_{inc}^2 + v_i^2}. \tag{2.10}$$

The sectional lift and sectional drag coefficients are typically determined by experiment and vary depending on blade pitch, thickness, camber and Reynolds number (Abbott and Doenhoff, 1959; Selig et al., 1995).

By integrating sectional lift and drag along the blade span, total lift and drag can be obtained

$$\begin{aligned} L &= \int_0^R C_l \frac{1}{2}\rho v^2 c \, \mathrm{d}r, \\ D &= \int_0^R C_d \frac{1}{2}\rho v^2 c \, \mathrm{d}r. \end{aligned} \tag{2.11}$$

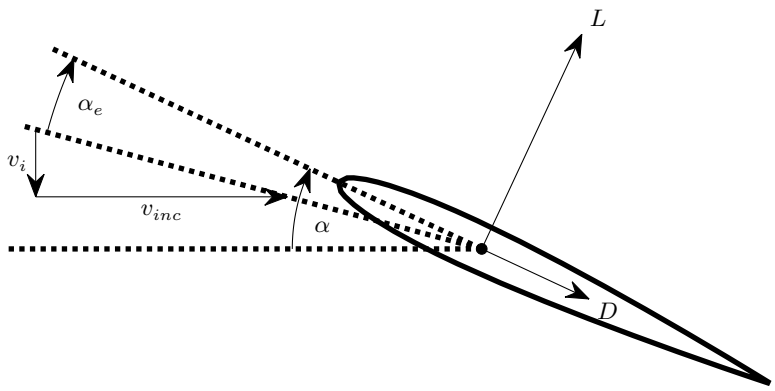

FIGURE 2.9: Schematic of lift and drag forces acting on a blade element, where α_e, α, v_i, v_{inc}, L and D are local effective angle of attack, local angle of attack, induced velocity, incident velocity, lift and drag respectively.

The lift and drag force can then be used to calculate the thrust, T, and torque about the z-axis, Q,

$$\begin{aligned} T &= N_b \left(L\cos(\alpha) - D\sin(\alpha) \right), \\ Q &= N_b r_{CoD} \left(L\sin(\alpha) + D\cos(\alpha) \right), \end{aligned} \tag{2.12}$$

where N_b and r_{CoD} are the number of rotor blades and radial distance measured from the rotor hub to the centre of drag respectively.

BEMT typically provides a more accurate estimate of rotor performance than momentum theory alone because it considers variation in loading across the blade span. Nonetheless, it is still limited because it assumes that the flow is inviscid and irrotational. More advanced numerical or experimental techniques are required in order to fully understand the effects that viscosity and vorticity have on rotor performance.

2.2.4 Studies of Full-Scale Rotor Aerodynamics

Due to the inherent limitations of momentum theory and BEMT, numerous researchers have sought to further understanding of hovering rotor performance by studying the formation of rotor wake structures. This subsection will focus on studies of full-scale rotor aerodynamics (i.e., within the Reynolds number range

$10^6 < Re < 10^7$). Balsa dust (Taylor, 1950), smoke flow (Drees and Hendal, 1951), water tunnel (Landgrebe and Bellinger, 1971), smoke entrapment (Landgrebe, 1972) and optical flow (Tangler et al., 1973) experimental methods have been used to visualise hovering rotor wakes. The results of these studies provide clear evidence for the presence of strong complex vortical structures in hovering rotor wakes. These structures consist of a strong vortex trailing from the blade tip as well as a vortex sheet that is shed from the rotor hub. The blade tip vortex is convected downward and inward radially, following the wake slipstream boundary that is predicted from momentum theory (as shown in Figure 2.8). Landgrebe (1972) used the results of these studies to obtain empirical laws governing the structure of rotor wakes and blade tip vortices. Caradonna and Tung (1981) used hot wire measurements to show that the peak swirl velocities within the blade tip vortex are approximately 40% of the blade tip speed. Thompson et al. (1988) used laser Doppler velocimetry measurements to analyse the blade tip vortex core in more detail, finding secondary vortex structures within the vortex core.

Beginning in the early 1990s, CFD began to rapidly grow in popularity, owing primarily to major advances in computing technology. Pioneering CFD research by Srinivasan et al. (1992), Srinivasan et al. (1993) and Srinivasan and Baeder (1993) used a Reynolds-averaged Navier-Stokes (RANS) method to compute the flow field through a hovering rotor. The solutions obtained were relatively under-resolved due to the coarseness of the meshes used. Nonetheless, they served to clearly demonstrate the potential for using RANS methods to model helicopter rotor fluid flow and wake structures. Accuracy of results improved rapidly with advances in computing technology with Wake and Baeder (1996) using a RANS method to model a UH-60 helicopter rotor. The results obtained were deemed to be accurate enough to use for industry design purposes. A major further development came with the application of overset grid methods (Steger et al., 1983) which allowed grid resolution to be simply and precisely specified in blade surface and wake regions. Despite these advances, early computational studies of helicopter rotor wakes tended to dissipate vortex structures faster than what was observed experimentally (Costes et al., 2012). This issue was addressed by Tang (1998) using an adaptive mesh

refinement technique and a high order Euler solver and by Steinhoff and Lynn (2006) using a vorticity confinement technique that modified the momentum equation in order to reduce the effect of numerical dissipation of vorticity. Both methods reduced numerical dissipation of vorticity and provided velocity profile results that more closely matched experimental results. Beginning in 2005, Duraisamy (2005), Duraisamy and Baeder (2007) and Duraisamy et al. (2007) used a RANS solver to model hovering rotors with a specific focus on resolving the structure of blade tip vortices. The results of these studies were validated against experimental results and showed clear evidence for the existence of secondary and tertiary vortex structures within the blade tip vortex core.

2.2.5 Studies of Micro Rotor Aerodynamics

When it comes to understanding micro rotor-craft fluid dynamics, studies of full-scale rotors can provide only limited insight due to the large difference in Reynolds number that occurs when moving from full-scale to micro-scale aircraft. As previously mentioned, micro rotors operate in a Reynolds number range of $10^3 < Re < 10^5$ (Lakshminarayan and Baeder, 2010a) which is significantly lower than for full-scale rotors. This means that viscous effects are much more significant at micro-scale than at full-scale, causing micro rotor-craft to suffer from poor lift and drag performance (Lissaman, 1983). Scaling of aerodynamic performance with varying Reynolds number has motivated researchers to conduct aerodynamic studies specific to micro rotor-craft.

Ramasamy et al. (2007) used digital particle image velocimetry (DPIV) to show that hovering micro rotors have significantly thicker boundary layers at the blade surface and a more turbulent wake than higher Reynolds number rotors. Additionally, the flow visualisations showed that the significant viscous effects at low Reynolds numbers cause an increase in tip vortex core size. Lakshminarayan and Baeder (2010a) used numerical methods to visualise micro rotor flow and also observed phenomena that are characteristic of low Reynolds number flow, including large turbulence in separated regions and shear layer instabilities in the wake. Nonetheless, the far wake contracted to $0.75R$ which is consistent with what has previously been

observed for full-scale rotors and what is predicted by momentum theory.

Studies of micro rotor efficiency have shown that these observed viscous effects contribute to a significant reduction in aerodynamic efficiency. Experimental studies have measured maximum figure of merit ($F.M.$, a measure of rotor efficiency) values of 0.55 (Bohorquez et al., 2003b) and 0.5 (Ramasamy et al., 2007) for single micro-rotors and 0.46 and 0.33 (Liu et al., 2011) for upstream and downstream micro coaxial rotors respectively. These results have been further strengthened by numerical studies which have calculated maximum $F.M.$ values of 0.55 (Lakshminarayan and Baeder, 2010a) for single micro rotors. These measures of efficiency are significantly smaller than for higher Reynolds number rotors which typically operate in a $F.M.$ range of 0.7 to 0.8 (Leishman, 2006). Despite these discrepancies in efficiency, Ramasamy et al. (2008) found that conventional rotor design methods (i.e., varying blade twist and area to improve efficiency) are still applicable at a micro scale.

2.2.6 Studies of Fluid Interactions Between a Rotor and a Planar Surface

The studies discussed in Sections 2.2.4 and 2.2.5 show that the blade tip vortex downstream of a rotor is a complex aerodynamic phenomena containing secondary and tertiary vortex structures. When a rotor is in close proximity to a planar surface, these vortex structures within the wake will interact with the planar surface and induce changes in the flow field through the rotor disk (Leishman et al., 2002). To date, studies of fluid interactions between a rotor and nearby obstacles have primarily focused on ground plane interactions. This is because the bulk of rotor aerodynamics research is concerned with full-scale helicopters which are typically prohibited from operating near to obstacles (other than the ground). Cheeseman and Bennett (1955) sought to simplify the complex vortex interactions with a ground plane using a momentum theory/method of images model, showing that the relationship between ground proximity, h_g, and rotor thrust, T, could be approximated by

$$\frac{T}{T'} = \frac{1}{1 - {R^2}/{16h_g^2}}, \tag{2.13}$$

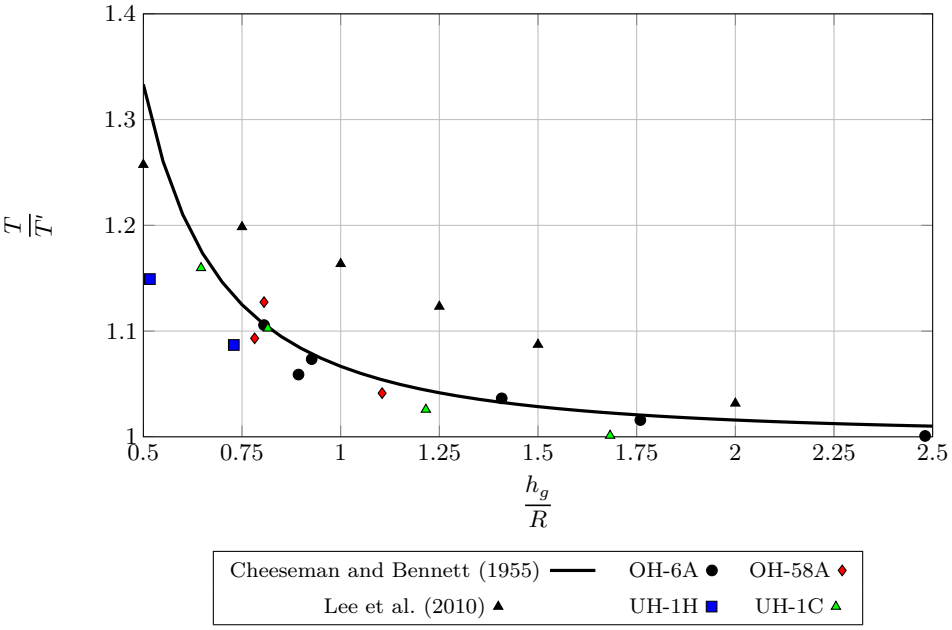

FIGURE 2.10: Effect of ground proximity on rotor thrust. Plot shows non-dimensionalised thrust vs non-dimensionalised rotor-ground gap.

where T' is the baseline hovering thrust (i.e., the thrust generated by the rotor when it is far from any obstacles). Equation (2.13) is limited because it does not consider viscosity or boundary layer effects near the ground plane and is only valid for rotor-ground gaps greater than $0.5R$. Despite this, it still fits well to experimental data collected for the OH-6A, OH-58A, UH-1H and UH-1C helicopters (Hayden, 1976), as shown in Figure 2.10. These helicopters all have full scale rotors with Reynolds numbers in the range of $10^6 < Re < 10^7$. For comparison, the experimental results of Lee et al. (2010) for a hovering micro rotor with a Reynolds number of $42,170$ are also included in Figure 2.10. Equation (2.13) shows significantly poorer agreement with the lower Reynolds number rotor, as is discussed in more detail in the following paragraphs. Nonetheless, the results presented in Figure 2.10 all clearly demonstrate that a hovering rotor in close proximity to the ground will experience a significant increase in thrust. If thrust is kept constant as a rotor nears the ground, the power required to maintain the constant thrust will reduce, i.e., rotor efficiency improves as rotor-ground gap decreases (Leishman, 2006).

Experimental and numerical techniques have been used to more comprehensively analyse the flow field through a full-scale rotor in close proximity to a ground

plane. Curtiss et al. (1984) analysed a rotor at low advance ratios using hot wire measurements and found that a recirculation region formed directly below the rotor. At higher advance ratios, a vortex formed at the ground with larger circulation than the circulation within the blade tip vortex. The structure of the blade tip vortex near the ground has been analysed in more detail by Light (1989) using a wide-field shadowgraph technique. Results showed that the radial position of the tip vortex increases with decreasing rotor-ground gap and the vertical position of the tip vortex moves nearer to the rotor disk with decreasing rotor-ground gap. Essentially, the wake is diverted outward by the ground plane and the blade tip vortex is convected outward as a result of this. This outward radial expansion of the wake has been confirmed by FV model studies of rotor wakes in close proximity to a ground plane (Leishman et al., 2002; Griffiths et al., 2005). More comprehensive RANS simulations conducted by Hariharan et al. (2011) using an adaptive mesh refinement technique also exhibited radial wake expansion as well as complex secondary and tertiary vortex structures near the surface of the ground plane. Further to this, the effects of turbulent interactions near a ground plane have been investigated by Morales and Squires (2011) using direct numerical simulation (DNS). Results showed that vortex structures near the ground plane distorted the turbulent boundary layer and increased shear stress at the ground, as well as turbulent kinetic energy.

Several studies of fluid interactions between a hovering rotor and a ground plane from the existing literature focus specifically on low Reynolds number micro-scale rotors. An experimental study by Lee et al. (2010) (previously presented in Figure 2.10) has shown that a micro rotor hovering in close proximity to a ground plane with a Reynolds number of $42,170$ will experience a significant increase in thrust as rotor-ground gap decreases. The observed thrust increase due to ground proximity is approximately 1.5 to 2 times larger than for full-scale rotors, i.e., fluid interactions with a ground plane become more significant as Reynolds number decreases. The results of Lee et al. (2010) showed that this strengthening of fluid interactions with decreasing Reynolds number is induced by increases in the blade tip vortex core size and circulation. RANS studies by Lakshminarayan et al. (2013) and Kalra (2014) at a Reynolds number of $32,400$ have also shown that the decay

of vorticity within the blade tip vortex slows as rotor-ground gap decreases.

Fluid interactions between a rotor and a ceiling plane have been investigated by Rossow (1985) using a vortex cylinder model and experimental methods. Rossow (1985) analysed a Reynolds number range of $86,000$ to $158,000$ and showed that radial contraction of the wake increases as rotor-ceiling gap decreases. This change in wake shape was shown to provide an increase in thrust as rotor-ceiling gap decreases (although this thrust increase is approximately half that experienced by a micro rotor in close proximity to a ground plane). This thrust increase has also been observed anecdotally by Powers et al. (2013).

Studies of fluid interactions between a hovering rotor and a planar surface from the existing literature provide clear evidence for the existence of complex interactions between vortex structures. These interactions have been observed to cause vortex stretching and intensification which, in turn, alter the induced velocity and forces and torques acting at the rotor. At present, there is a comprehensive body of research in the existing literature relating to ground plane fluid interactions. Efforts have also been made to investigate ceiling plane fluid interactions, although further work is necessary in order to understand the fundamental fluid interaction phenomena that drive ceiling-plane interactions. Fluid interactions between hovering rotors and wall planes, inclined planes or irregular shaped obstacles are not addressed in the existing literature.

2.3 State and Disturbance Estimation

As discussed in Section 2.2, fluid interactions between a hovering micro rotor and a planar surface will alter rotor thrust and torque. These changes in thrust and torque due to aerodynamic proximity effects can be treated as exogenous disturbances acting on a micro helicopter. In order to compensate for these disturbances and to maintain stability of a micro helicopter, it is necessary to estimate helicopter states and disturbances during flight (Radke and Gao, 2006). As outlined in Chapter 1, the simultaneous estimation of micro helicopter states and exogenous disturbances is the secondary objective of this research. In this section, a review of state estimation, disturbance estimation and simultaneous state and disturbance estimation techniques

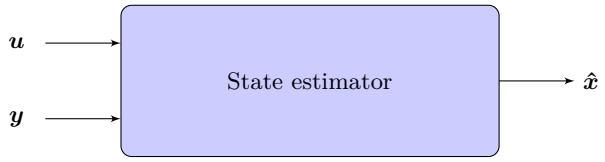

Figure 2.11: State estimator schematic, where $\boldsymbol{u}$, $\boldsymbol{y}$ and $\hat{\boldsymbol{x}}$ are the known inputs, measured outputs and estimated states respectively.

is provided. Because helicopter hovering dynamics can be accurately represented by a linear model (Mettler et al., 2002), linear estimation techniques are the focus of this review. Note that, while the content of this section focuses on micro helicopter state and disturbance estimation, it is applicable to multi-rotor and fixed wing MAVs also.

2.3.1 Fundamentals of State Estimation and Kalman Filtering

In general, state estimation techniques seek to answer the following question: *How can the states of a system be most accurately estimated based upon observed signals that are affected by random noise and exogenous disturbances?* The state estimation problem can be expressed more generally for a linear system by considering it in state space form

$$\begin{aligned} \dot{\boldsymbol{x}} &= \boldsymbol{A}\boldsymbol{x} + \boldsymbol{B}_{\boldsymbol{u}}\boldsymbol{u}, \\ \boldsymbol{y} &= \boldsymbol{C}\boldsymbol{x} + \boldsymbol{D}_{\boldsymbol{u}}\boldsymbol{u}, \end{aligned} \tag{2.14}$$

where $\boldsymbol{x} \in \mathbb{R}^n$, $\boldsymbol{u} \in \mathbb{R}^m$, $\boldsymbol{y} \in \mathbb{R}^p$, $\boldsymbol{A} \in \mathbb{R}^{n\times n}$, $\boldsymbol{B}_{\boldsymbol{u}} \in \mathbb{R}^{n\times m}$, $\boldsymbol{C} \in \mathbb{R}^{p\times n}$ and $\boldsymbol{D}_{\boldsymbol{u}} \in \mathbb{R}^{p\times m}$ are the state vector, input vector, output vector, state matrix, input matrix, output matrix and input feed-through matrix respectively and m, n and p are the number of inputs, number of states and number of outputs respectively. The goal of a state estimator is to obtain an estimate of the state vector, $\hat{\boldsymbol{x}} \in \mathbb{R}^n$, using only the known inputs and measured outputs. A schematic showing this process is provided in Figure 2.11.

The simplest model-based state estimator is that postulated by Luenberger (1966) (commonly known as the Luenberger observer or state observer). The Luenberger

observer uses a state estimator gain, $\boldsymbol{L_x} \in \mathbb{R}^{n \times p}$, to minimise the error between the state estimate and the actual states

$$\dot{\hat{\boldsymbol{x}}} = \boldsymbol{A}\hat{\boldsymbol{x}} + \boldsymbol{B_u}\boldsymbol{u} + \boldsymbol{L_x}\left(\boldsymbol{y} - \boldsymbol{C}\hat{\boldsymbol{x}} - \boldsymbol{D_u}\boldsymbol{u}\right). \tag{2.15}$$

Direct pole placement is commonly used to choose $\boldsymbol{L_x}$ such that the estimator error dynamics, $\boldsymbol{A} - \boldsymbol{L_x}\boldsymbol{C}$, are stable according to the Routh-Hurwitz criterion, i.e., the real component of eigenvalues for the estimator error dynamics must all be negative (Hurwitz, 1895). This method can provide adequate state estimation performance for many applications, however, estimation accuracy can degrade due to model uncertainty, measurement noise and the presence of exogenous disturbances. Under such conditions, it is likely that a more systematic process will be required in order to optimise estimation performance. State estimation for systems affected by random measurement noise was addressed by Kalman (1960), using what is now commonly referred to as the Kalman filter. Kalman built upon the earlier work of Weiner (1949) by approaching the problem of optimal state estimation from the point of view of conditional probabilities. Kalman's novel method uses the solution to the algebraic Riccati equation (Lancaster and Rodman, 1995)

$$\begin{aligned} \dot{\boldsymbol{P}} &= \boldsymbol{A}\boldsymbol{P} + \boldsymbol{P}\boldsymbol{A}^T + \boldsymbol{G}\boldsymbol{Q}\boldsymbol{G}^T - \boldsymbol{P}\boldsymbol{C}^T\boldsymbol{R}^{-1}\boldsymbol{C}\boldsymbol{P}, \\ \boldsymbol{L_x} &= \boldsymbol{P}\boldsymbol{C}^T\boldsymbol{R}^{-1}, \end{aligned} \tag{2.16}$$

to optimally obtain $\boldsymbol{L_x}$, where $\boldsymbol{G} \in \mathbb{R}^{n \times n}$, $\boldsymbol{Q} \in \mathbb{R}^{n \times n}$ and $\boldsymbol{R} \in \mathbb{R}^{n \times n}$ are the process noise input matrix, process noise covariance matrix and measurement noise covariance matrix respectively. The Kalman filter has since been extended to non-linear systems using the extended Kalman filter (EKF) (McElhoe, 1966) and unscented Kalman filter (UKF) (Julier and Uhlmann, 1997) and is widely used in fields such as inertial navigation, error dynamics modelling, radar tracking and global navigation satellite systems (Grewal and Andrews, 2010).

For rotor-craft and helicopters, it is common to estimate kinematic states in order to implement attitude and trajectory control systems. In this case, the state vector can be defined as

$$\boldsymbol{x} = \begin{bmatrix} \boldsymbol{v} \\ \boldsymbol{\Theta} \\ \boldsymbol{\omega} \end{bmatrix}, \tag{2.17}$$

where the velocity states, $\boldsymbol{v} \in \mathbb{R}^3$, attitude and heading states, $\boldsymbol{\Theta} \in \mathbb{R}^3$, and angular velocity states, $\boldsymbol{\omega} \in \mathbb{R}^3$, are

$$\begin{aligned} \boldsymbol{v} &= \begin{bmatrix} u & v & w \end{bmatrix}^T, \\ \boldsymbol{\Theta} &= \begin{bmatrix} \phi & \theta & \psi \end{bmatrix}^T, \\ \boldsymbol{\omega} &= \begin{bmatrix} p & q & r \end{bmatrix}^T, \end{aligned} \tag{2.18}$$

where u, v, w, ϕ, θ, ψ, p, q and r are velocity in the x direction (also referred to as longitudinal velocity), velocity in the y direction (also referred to as lateral velocity), velocity in the z direction (also referred to as heave velocity), rotation about the x-axis, rotation about the y-axis, rotation about the z-axis, angular velocity about the x-axis, angular velocity about the y-axis and angular velocity about the z-axis respectively, as defined in Figure 2.12. Additional states such as rotor and stabiliser bar flapping angles may also be included (Mettler et al., 2002). Typically, these states are estimated by combining measurements from MEMS inertial sensors, GPS, motion capture systems and additional proximity sensors. A simple commonly used attitude estimator is the complementary filter (Higgins, 1975) which low-pass filters accelerometer data and high-pass filters gyroscope data to obtain an attitude estimate. The complementary filter has a low computational cost and is ideal for applications where translational accelerations are expected to remain close to zero (Marantos et al., 2015). For a rotor-craft performing high acceleration manoeuvres, it is likely that a more robust estimation scheme will be required. Improved attitude estimation performance can be obtained using the gradient descent algorithm (Madgwick et al., 2011). Porter et al. (2015) successfully used this scheme to estimate attitude of a fixed multi-rotor test-bench and Valenti et al. (2015) have successfully used this scheme to estimate attitude of a micro quad rotor during experimental flight tests.

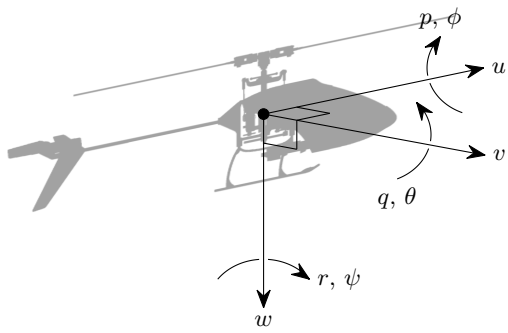

FIGURE 2.12: Schematic showing the kinematic states of a rotor-craft where u, v, w, ϕ, θ, ψ, p, q and r are velocity in the x direction, velocity in the y direction, velocity in the z direction, rotation about the x-axis, rotation about the y-axis, rotation about the z-axis, angular velocity about the x-axis, angular velocity about the y-axis and angular velocity about the z-axis respectively.

To estimate the remaining kinematic states, it is most common to use a Kalman filter (or a Kalman filter-based algorithm) to merge inertial sensor measurements with GPS or motion capture measurements. The EKF (Ye et al., 2013) and the UKF (de Marina et al., 2012) have both been used extensively in the existing literature for micro rotor-craft and fixed-wing MAV state estimation.

Note that, in the case of a micro rotor-craft operating within a confined environment, it is not viable to rely on access to GPS or motion capture measurements. Under such conditions, special consideration must be given to the translational velocity states as these cannot typically be directly estimated from inertial sensor data alone (Bry et al., 2012).

2.3.2 Disturbance Estimation

In general, disturbance estimation techniques seek to answer the following question: *How can the exogenous disturbances acting on a system be most accurately estimated based upon known system states and known inputs to the system?* For many applications, it is desirable to estimate exogenous disturbances in order to implement a control system that can compensate for them. For a linear system that is subject to exogenous disturbances, the state dynamics described by Equation (2.14) can be extended to

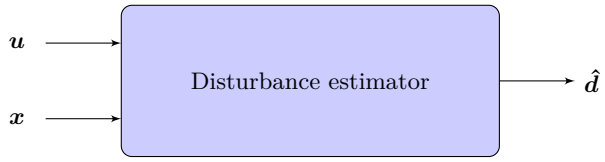

Figure 2.13: Disturbance estimator schematic, where $\boldsymbol{u}$, $\boldsymbol{x}$, and $\hat{\boldsymbol{d}}$ are the known inputs, known states and estimated disturbances respectively.

$$\begin{aligned} \dot{\boldsymbol{x}} &= \boldsymbol{A}\boldsymbol{x} + \boldsymbol{B}_{\boldsymbol{u}}\boldsymbol{u} + \boldsymbol{B}_{\boldsymbol{d}}\boldsymbol{d}, \\ \boldsymbol{y} &= \boldsymbol{C}\boldsymbol{x} + \boldsymbol{D}_{\boldsymbol{u}}\boldsymbol{u}, \end{aligned} \tag{2.19}$$

where $\boldsymbol{d} \in \mathbb{R}^q$ and $\boldsymbol{B}_{\boldsymbol{d}} \in \mathbb{R}^{n \times q}$ are the disturbance vector and disturbance matrix respectively and q is the number of exogenous disturbances. A schematic illustrating a typical disturbance estimation process is provided in Figure 2.13, where $\hat{\boldsymbol{d}} \in \mathbb{R}^q$ is the disturbance estimate.

The most common simple linear disturbance estimator assumes a constant disturbance and uses an augmented state vector, $\boldsymbol{z} \in \mathbb{R}^n$, to obtain a disturbance estimate (Li et al., 2014)

$$\begin{aligned} \dot{\boldsymbol{z}} &= -\boldsymbol{L}_{\boldsymbol{d}}\left(\boldsymbol{A}\boldsymbol{x} + \boldsymbol{B}_{\boldsymbol{u}}\boldsymbol{u} + \boldsymbol{B}_{\boldsymbol{d}}\hat{\boldsymbol{d}}\right), \\ \hat{\boldsymbol{d}} &= \boldsymbol{z} + \boldsymbol{L}_{\boldsymbol{d}}\boldsymbol{x}, \end{aligned} \tag{2.20}$$

where $\boldsymbol{L}_{\boldsymbol{d}} \in \mathbb{R}^{q \times n}$ is the disturbance estimator gain. $\boldsymbol{L}_{\boldsymbol{d}}$ is typically chosen using direct pole placement such that $-\boldsymbol{L}_{\boldsymbol{d}}\boldsymbol{B}_{\boldsymbol{d}}$ is stable according to the Routh-Hurwitz criterion (Hurwitz, 1895). Similar linear disturbance estimation techniques have also been postulated by Umeno and Hori (1991) and Schrijver and van Dijk (2002). Like the Luenberger observer, linear disturbance estimators can provide good estimation performance, however, estimation performance can degrade due to model uncertainty and measurement noise. To a certain extent, this issue has been addressed using non-linear estimators (Muller, 1990) and fault estimators (Chen et al., 1995). More significant advances have also been made with the introduction of the perturbation observer (Kwon and Chung, 2003, 2004), which estimates unmodelled plant dynamics as well as exogenous disturbances. An alternative method for accounting for

unmodelled plant dynamics was introduced by Han (1995), using an extended state observer (ESO). The ESO uses a canonical formulation that groups unmodelled dynamics with disturbance estimation, allowing for good disturbance estimation performance even in the presence of high model uncertainty.

In the case of a hovering rotor-craft, exogenous disturbances, $\boldsymbol{d}$, are made up of force disturbances, $\overline{\boldsymbol{F}} \in \mathbb{R}^3$, and torque disturbances, $\overline{\boldsymbol{M}} \in \mathbb{R}^3$, where

$$\begin{aligned} \overline{\boldsymbol{F}} &= \begin{bmatrix} \overline{X} & \overline{Y} & \overline{Z} \end{bmatrix}^T, \\ \overline{\boldsymbol{M}} &= \begin{bmatrix} \overline{L} & \overline{M} & \overline{N} \end{bmatrix}^T, \end{aligned} \tag{2.21}$$

where $\overline{X}$, $\overline{Y}$, $\overline{Z}$, $\overline{L}$, $\overline{M}$ and $\overline{N}$ are disturbance force in the x direction, disturbance force in the y direction, disturbance force in the z direction, disturbance torque about the x-axis, disturbance torque about the y-axis and disturbance torque about the z-axis respectively, as shown in Figure 2.14. For a rotor-craft hovering in close proximity to a planar surface, these exogenous force and torque disturbances will be induced by fluid interactions between the rotor and the planar surface. Several studies from the existing literature have applied disturbance estimation techniques to micro rotor-craft or MAVs. Shin et al. (2009) demonstrated the applicability of robust disturbance estimators to unmanned aerial vehicle (UAV) control by using a robust disturbance estimator to improve simulated UAV formation control. A sliding mode disturbance estimator was used by Besnard et al. (2007) to simulate attitude and translational control of a X-4 Flyer quad rotor in the presence of lateral wind gusts and modelling uncertainties. The simulation results indicated that the sliding mode estimator significantly improved the aircraft's ability to compensate for the lateral wind gust disturbances. Iqbal et al. (2011) later verified the robustness of the sliding mode disturbance estimator through experimental tests using a DC motor rig. Fan et al. (2011) were able to significantly reduce steady-state error by introducing a simple disturbance estimator into the attitude control loop for a small scale helicopter. Liu et al. (2012) successfully implemented a non-linear model based controller with a disturbance estimator to regulate position and attitude of a micro rotor-craft hovering in the presence of wind gust disturbances. More recently,

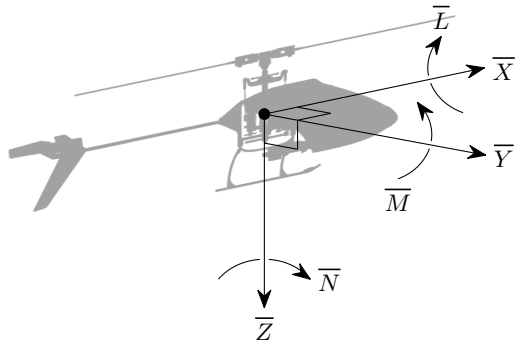

Figure 2.14: Schematic showing exogenous force and torque disturbances acting on a rotor-craft where $\overline{X}$, $\overline{Y}$, $\overline{Z}$, $\overline{L}$, $\overline{M}$ and $\overline{N}$ are disturbance force in the x direction, disturbance force in the y direction, disturbance force in the z direction, disturbance torque about the x-axis, disturbance torque about the y-axis and disturbance torque about the z-axis respectively.

Xie et al. (2015) have implemented a disturbance estimator based control system for a multi rotor helicopter with unstructured model uncertainties. The control system was shown to provide superior exogenous disturbance rejection performance to conventional robust H_∞ loop shaping controllers. These studies demonstrate the viability of applying disturbance estimation techniques to the estimation of exogenous disturbances induced by aerodynamic proximity effects.

2.3.3 Simultaneous State and Disturbance Estimation

The primary limitation of the disturbance estimation techniques reviewed in Section 2.3.2 is that they rely on having access to the full state vector in order to obtain a disturbance estimate. As noted in Section 2.3.1, the translational velocity states of a micro rotor-craft cannot typically be directly estimated using measurements provided by inertial sensors alone, i.e., a micro rotor-craft operating within a confined GPS-denied environment will not have access to the full state vector described by Equation (2.17). Under such conditions, the disturbance estimation schemes presented in Section 2.3.2 cannot be realised. Instead, a simultaneous state and disturbance estimation scheme must be utilised.

In general, a simultaneous state and disturbance estimator seeks to answer the following question: *How can the unknown states and exogenous disturbances acting*

on a system be most accurately estimated based upon known state measurements and known inputs to the system? A schematic describing such a system is provided in Figure 2.15. Several studies in the existing literature have addressed the problem of simultaneous state and disturbance estimation. Although not a true state and disturbance estimator, Fairman et al. (1984) developed a full order linear state estimator for systems with unknown inputs. Fairman et al. (1984) also explicitly proved the conditions required for the existence of such an estimator for a given system. Miller and Mukundan (1982) derived a reduced order linear state estimator for systems with unknown inputs that eliminated some of the computational requirements associated with a full order estimator. Both techniques could be cascaded in series with a conventional disturbance estimator in order to estimate disturbances as well. However, such an approach was deemed too computationally expensive to be viable for real-time estimation. A true simultaneous state and disturbance estimator was first postulated by Stein and Park (1988). This estimator utilised deconvolution and singular value decomposition to obtain a linear estimator for time invariant systems. A similar estimator derived using an inverse dynamics-based approach was also postulated by Liu and Peng (2002). Zhu (2012) later used a sliding mode approach to develop a reduced order estimator that is valid for systems where the observer matching condition is not satisfied, i.e., for systems where the invariant zeros do not all lie in the left half plane (LHP) (Kalsi et al., 2010).

A major limitation of the simultaneous state and disturbance estimators reviewed in this section is that they do not consider the effect of direct feed-through of disturbances to the measured output, i.e., systems with an output equation of the following form

$$\begin{aligned} \dot{\boldsymbol{x}} &= \boldsymbol{A}\boldsymbol{x} + \boldsymbol{B}_{\boldsymbol{u}}\boldsymbol{u} + \boldsymbol{B}_{\boldsymbol{d}}\boldsymbol{d}, \\ \boldsymbol{y} &= \boldsymbol{C}\boldsymbol{x} + \boldsymbol{D}_{\boldsymbol{u}}\boldsymbol{u} + \boldsymbol{D}_{\boldsymbol{d}}\boldsymbol{d}, \end{aligned} \tag{2.22}$$

where $\boldsymbol{D}_{\boldsymbol{d}} \in \mathbb{R}^{p \times q}$ is the disturbance feed-through matrix. As will be shown in Chapter 3.1, exogenous disturbances acting on a micro helicopter will feed-through directly to translational acceleration measurements obtained using a MEMS accelerometer, i.e., $\boldsymbol{D}_{\boldsymbol{d}} \neq 0$ for a micro helicopter. With this in mind, it is clear that the existing

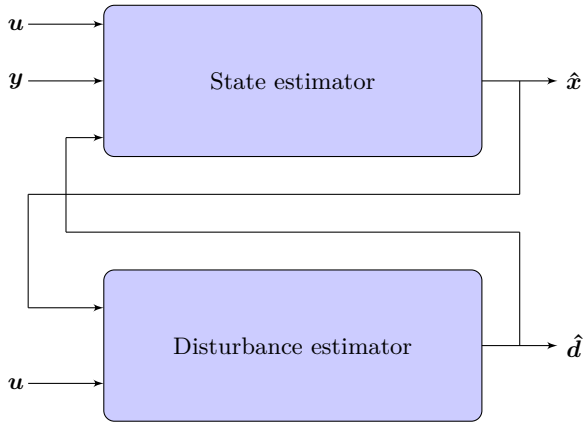

Figure 2.15: Simultaneous state and disturbance estimator schematic, where $\boldsymbol{u}$, $\boldsymbol{y}$, $\hat{\boldsymbol{x}}$ and $\hat{\boldsymbol{d}}$ are the known inputs, measured outputs, estimated states and estimated disturbances respectively.

body of simultaneous state and disturbance estimation research must be extended in order to implement an estimator on-board a micro helicopter that relies only on measurements provided by inertial sensors and accounts for direct feed-through.

2.4 Summary

The existing literature reviewed in this chapter demonstrates that an obstacle in close proximity to a hovering micro rotor will induce fluid interactions with the rotor wake. At present, fluid interactions between a micro rotor and a ground plane have been studied in the existing literature, however, further investigation is required in order to understand the physical nature of fluid interactions between a micro rotor and a ceiling or wall plane. These interactions are likely to alter the flow field through the rotor disk which will, in turn, generate a disturbance at the rotor. Micro helicopters are vulnerable to disturbances induced by aerodynamic proximity effects because of their low inertia and their lack of sensing hardware capable of detecting proximity to an obstacle. If uncompensated for, these disturbances may have an adverse effect on micro helicopter stability and/or performance. To maintain control of a micro helicopter under such conditions, it is necessary to estimate disturbances during flight so that an appropriate control response can be generated. With this in mind, the research outlined in this thesis aims to investigate the fundamental physics

that govern fluid interactions between a micro rotor and a nearby ceiling plane or wall plane. Additionally, this thesis aims to estimate the disturbances induced by these fluid interactions during flight using a simultaneous state and disturbance estimator. The estimator will be designed to rely only on measurements provided by on-board inertial sensors (as systems such as GPS and motion tracking are not likely to be feasible in a confined environment). Finally, the disturbance estimate, along with *a priori* knowledge of how the disturbance varies with proximity, will be used to passively estimate proximity to a planar surface. The objectives of this research have previously been outlined in more detail in Section 1.2.

Chapter 3

Micro Helicopter Hovering Dynamics

This chapter provides an overview of the hovering dynamics of a micro helicopter. Understanding hovering dynamics is important in order to evaluate how the stability of a micro helicopter will be affected by exogenous disturbances induced by aerodynamic proximity effects. Additionally, a model of micro helicopter hovering dynamics is required in order to implement the model-based simultaneous state and disturbance estimator outlined in Chapter 8. In Section 3.1, the hovering dynamics model is derived. Note that, while this model is applied to micro helicopters in this thesis, it is also applicable to larger scale single main rotor helicopters. In Section 3.2, the micro helicopter test-bed used in this research for performing experimental flight tests is outlined in detail. Finally, in Section 3.3, frequency domain parametric system identification is used to identify the unknown hovering dynamics model parameters for the experimental test-bed.

3.1 Derivation of Micro Helicopter Hovering Dynamics Model

In this section, a linearised representation of a micro helicopter's hovering dynamics is derived using the method of Mettler et al. (2002) and Mettler (2003). This method is well regarded in the existing literature, having been used extensively for the

implementation of model-based helicopter control systems (Ahmed and Pota, 2011).

Note that the model derived in this section uses the standard body-fixed aircraft coordinate system (Padfield, 2007), previously illustrated in Figure 2.1. Note also that coupling between translation in the x direction and rotation about the y-axis is referred to as *longitudinal dynamics*. Coupling between translation in the y direction and rotation about the x-axis is referred to as *lateral dynamics*. Coupling between translation in the z direction and rotation about the z-axis is referred to as *heave-yaw dynamics*.

3.1.1 Rigid Body Dynamics

The rigid body 6 DOF dynamics of flight vehicles, such as a helicopter, can be derived from the Newton-Euler equations

$$\begin{aligned} \boldsymbol{F} &= m\frac{\mathrm{d}\boldsymbol{v}}{\mathrm{d}t}, \\ \boldsymbol{M} &= \boldsymbol{J}\frac{\mathrm{d}\boldsymbol{\omega}}{\mathrm{d}t}, \end{aligned} \tag{3.1}$$

where m and t are mass and time respectively. The force vector, $\boldsymbol{F} \in \mathbb{R}^3$, torque vector $\boldsymbol{M} \in \mathbb{R}^3$, and inertial tensor, $\boldsymbol{J} \in \mathbb{R}^{3\times3}$, are

$$\begin{aligned} \boldsymbol{F} &= \begin{bmatrix} X & Y & Z \end{bmatrix}^T, \\ \boldsymbol{M} &= \begin{bmatrix} L & M & N \end{bmatrix}^T, \\ \boldsymbol{J} &= \begin{bmatrix} J_{xx} & -J_{xy} & -J_{xz} \\ -J_{yx} & J_{yy} & -J_{yz} \\ -J_{zx} & -J_{zy} & J_{zz} \end{bmatrix}, \end{aligned} \tag{3.2}$$

where X, Y, Z, L, M, N, and J are force in the x direction, force in the y direction, force in the z direction, torque about the x-axis, torque about the y-axis, torque about the z-axis and moment of inertia respectively.

Equation (3.1) can be rewritten in the body fixed frame as

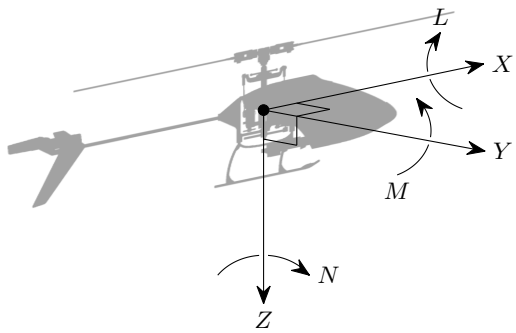

FIGURE 3.1: Schematic showing the forces and torques acting on a rotor-craft where X, Y, Z, L, M and N are force in the x direction, force in the y direction, force in the z direction, torque about the x-axis, torque about the y-axis and torque about the z-axis respectively.

$$\begin{aligned} \boldsymbol{F} &= m\dot{\boldsymbol{v}} + m\left(\boldsymbol{\omega} \times \boldsymbol{v}\right), \\ \boldsymbol{M} &= \boldsymbol{J}\dot{\boldsymbol{\omega}} + \left(\boldsymbol{\omega} \times \boldsymbol{J}\boldsymbol{\omega}\right). \end{aligned} \tag{3.3}$$

Expanding Equation (3.3) and rewriting in terms of translational and angular accelerations yields

$$\begin{aligned} \dot{u} &= -wq + vr + \frac{X}{m}, \\ \dot{v} &= -ur + wp + \frac{Y}{m}, \\ \dot{w} &= -vp + uq + \frac{Z}{m}, \\ \dot{p} &= -qr\frac{J_{yy} - J_{zz}}{J_{xx}} + \frac{L}{J_{xx}}, \\ \dot{q} &= -pr\frac{J_{zz} - J_{xx}}{J_{yy}} + \frac{M}{J_{yy}}, \\ \dot{r} &= -pq\frac{J_{xx} - J_{yy}}{J_{zz}} + \frac{N}{J_{zz}}. \end{aligned} \tag{3.4}$$

Equation (3.4) describes how a helicopter's rigid body kinematics responds to forces and torques. For a helicopter, these forces and torques are generated by the main and tail rotors as well as exogenous force and torque disturbances.

3.1.2 Stability Derivative Linearisation

If it is assumed that the helicopter is in hover, then attitude angles and translational accelerations will be near zero. Under such conditions, helicopter hovering dynamics can be approximated by a linear model (Mettler et al., 2002). As this research is focused on helicopters in hover only, the accuracy provided by a linear model has been deemed adequate. Use of a linear model can also be advantageous over non-linear models as it greatly simplifies the estimator and controller design process.

The non-linear dynamics described by Equation (3.4) can be linearised by analysing the dynamics about the hovering equilibrium state vector, $\boldsymbol{x}_0 \in \mathbb{R}^n$, and hovering equilibrium input vector, $\boldsymbol{u}_0 \in \mathbb{R}^m$

$$\dot{\boldsymbol{x}} = \left(\frac{\partial \boldsymbol{f}}{\partial \boldsymbol{x}}\right)_{\boldsymbol{x}_0,\boldsymbol{u}_0} \delta x + \left(\frac{\partial \boldsymbol{f}}{\partial \boldsymbol{u}}\right)_{\boldsymbol{x}_0,\boldsymbol{u}_0} \delta \boldsymbol{u}, \tag{3.5}$$

or in state space form

$$\delta \dot{\boldsymbol{x}} = \boldsymbol{A}\delta \boldsymbol{x} + \boldsymbol{B}\delta \boldsymbol{u}, \tag{3.6}$$

where $\delta \boldsymbol{x} \in \mathbb{R}^n$ and $\delta \boldsymbol{u} \in \mathbb{R}^m$ are small perturbations about the hovering equilibrium points, $\boldsymbol{x}_0$ and $\boldsymbol{u}_0$ respectively. The trim conditions used for obtaining the linearised hovering dynamics are

$$\boldsymbol{v}_0 = \boldsymbol{\omega}_0 = \begin{bmatrix} 0 & 0 & 0 \end{bmatrix}^T. \tag{3.7}$$

Note that other equilibrium states can also be used for obtaining linear models for level cruise flight, steady turns and helical trajectories (Mettler, 2003). The linearised equations of motion about the hovering equilibrium point are

$$
\begin{aligned}
\delta\dot{u} &= -w_0\delta q + \delta w q_0 + v_0\delta r + \delta v r_0 + \frac{\Delta X}{m}, \\
\delta\dot{v} &= -u_0\delta r + \delta u r_0 + w_0\delta p + \delta w p_0 + \frac{\Delta Y}{m}, \\
\delta\dot{w} &= -v_0\delta p + \delta v p_0 + u_0\delta q + \delta u q_0 + \frac{\Delta Z}{m}, \\
\delta\dot{p} &= \left(-q_0\delta r - \delta q r_0\right)\frac{J_{yy} - J_{zz}}{J_{xx}} + \frac{\Delta L}{J_{xx}}, \\
\delta\dot{q} &= \left(-p_0\delta r - \delta p r_0\right)\frac{J_{zz} - J_{xx}}{J_{yy}} + \frac{\Delta M}{J_{yy}}, \\
\delta\dot{r} &= \left(-p_0\delta q - \delta p q_0\right)\frac{J_{xx} - J_{yy}}{J_{zz}} + \frac{\Delta N}{J_{zz}}.
\end{aligned}
\tag{3.8}
$$

The change in forces, ΔX, ΔY and ΔZ, and the change in torques, ΔL, ΔM and ΔN, can be expressed using a Taylor series expansion (Taylor, 1715) (here, only the first order terms are considered)

$$
\begin{aligned}
\Delta X &= X_u\delta u + X_v\delta v + X_w\delta w + X_p\delta p + X_q\delta q + X_r\delta r \\
&\qquad + X_{lat}\delta_{lat} + X_{lon}\delta_{lon} + X_{col}\delta_{col} + X_{yaw}\delta_{yaw}, \\
\Delta Y &= Y_u\delta u + Y_v\delta v + Y_w\delta w + Y_p\delta p + Y_q\delta q + Y_r\delta r \\
&\qquad + Y_{lat}\delta_{lat} + Y_{lon}\delta_{lon} + Y_{col}\delta_{col} + Y_{yaw}\delta_{yaw}, \\
\Delta Z &= Z_u\delta u + Z_v\delta v + Z_w\delta w + Z_p\delta p + Z_q\delta q + Z_r\delta r \\
&\qquad + Z_{lat}\delta_{lat} + Z_{lon}\delta_{lon} + Z_{col}\delta_{col} + Z_{yaw}\delta_{yaw}, \\
\Delta L &= L_u\delta u + L_v\delta v + L_w\delta w + L_p\delta p + L_q\delta q + L_r\delta r \\
&\qquad + L_{lat}\delta_{lat} + L_{lon}\delta_{lon} + L_{col}\delta_{col} + L_{yaw}\delta_{yaw}, \\
\Delta M &= M_u\delta u + M_v\delta v + M_w\delta w + M_p\delta p + M_q\delta q + M_r\delta r \\
&\qquad + M_{lat}\delta_{lat} + M_{lon}\delta_{lon} + M_{col}\delta_{col} + M_{yaw}\delta_{yaw}, \\
\Delta N &= N_u\delta u + N_v\delta v + N_w\delta w + N_p\delta p + N_q\delta q + N_r\delta r \\
&\qquad + N_{lat}\delta_{lat} + N_{lon}\delta_{lon} + N_{col}\delta_{col} + N_{yaw}\delta_{yaw},
\end{aligned}
\tag{3.9}
$$

where the notation X_u represents the partial derivative $\partial X / \partial \delta u$ and δ_{lat}, δ_{lon}, δ_{yaw} and δ_{col} are changes in the lateral cyclic, longitudinal cyclic, collective and yaw pilot commands (measured relative to the hovering trim condition). Note that, for clarity, the difference operators, δ and Δ, are dropped for the remainder of this thesis (with the exception of the control inputs).

Partial derivatives in Equation (3.9) relating to helicopter states are referred to as *stability derivatives*. Partial derivatives in Equation (3.9) relating to helicopter control inputs are referred to as *control derivatives*. A large stability derivative value for a given state indicates that a large force or torque response will be generated by a small change in the state. A large control derivative value for a given control input indicates that a large force or torque response will be generated by a small change in the control input. When defining a helicopter model, it is important to ascertain which stability and control derivatives have the most significant effect on helicopter dynamics. Mettler (2003) has shown that the majority of the control and stability derivatives in Equation (3.9) have a negligible effect on helicopter hovering dynamics. By considering the dominant stability derivatives only, a state space representation of a helicopter's rigid body dynamics can be obtained

$$\boldsymbol{x} = \begin{bmatrix} u & v & p & q & \phi & \theta & w & r \end{bmatrix}^T,$$
$$\boldsymbol{A} = \begin{bmatrix} X_u & 0 & 0 & 0 & 0 & -g & 0 & 0 \\ 0 & Y_v & 0 & 0 & g & 0 & 0 & 0 \\ L_u & L_v & 0 & 0 & 0 & 0 & 0 & 0 \\ M_u & M_v & 0 & 0 & 0 & 0 & 0 & 0 \\ 0 & 0 & 1 & 0 & 0 & 0 & 0 & 0 \\ 0 & 0 & 0 & 1 & 0 & 0 & 0 & 0 \\ 0 & 0 & 0 & 0 & 0 & 0 & Z_w & Z_r \\ 0 & 0 & 0 & 0 & 0 & 0 & N_w & N_r \end{bmatrix}, \tag{3.10}$$

where $\boldsymbol{x}$, and $\boldsymbol{A}$ are the state vector and state matrix for a state space system of the form described by Equation (2.14). Note that in order to understand how the control derivatives affect hovering dynamics, it is necessary to first consider rotor dynamics, as outlined in Section 3.1.3.

3.1.3 Rotor Dynamics

As the rotor and helicopter body move, lift and drag forces acting at the blade cause flapping, feathering and lead-lagging (Johnson, 1980). For a hovering helicopter,

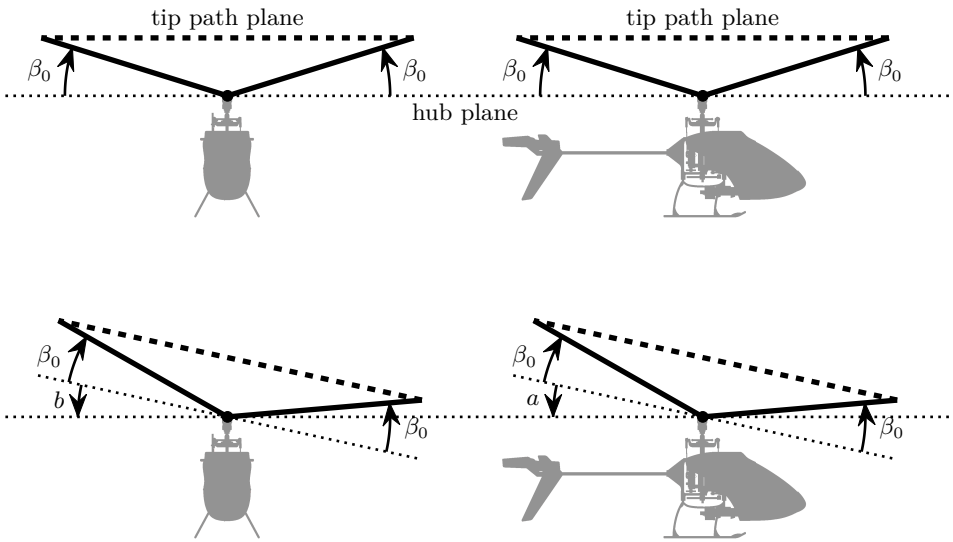

FIGURE 3.2: Schematic showing rotor coning and flapping about the lateral and longitudinal axes where β_0, a and b are coning angle, lateral flapping angle and longitudinal flapping angle respectively.

motion of the rotor relative to the helicopter body is dominated by flapping (Leishman, 2006). Flapping motion is the rotation of the entire rotor about its lateral and longitudinal axes, as illustrated in Figure 3.2 (note that rotor coning is also shown in this figure). The rigid body dynamics described by Equation (3.10) neglect dynamic coupling between rotor flapping and helicopter rigid body dynamics. It has been shown that neglecting this dynamic coupling yields poor model accuracy at high frequencies (Hansen, 1982). Therefore, to maintain model accuracy, it is necessary to extend the rigid body dynamics to include rotor flapping dynamics.

For the model used in this research, low frequency blade flapping dynamics are considered. The rotor blades are modelled as rigid bodies that are hinged at the rotor hub. By considering a tip path plane (TPP) model of the rotor, flapping dynamics can be described using a second order differential equation (Chen, 1980)

$$\begin{bmatrix} \ddot{a} \\ \ddot{b} \end{bmatrix} + \boldsymbol{D_f} \begin{bmatrix} \dot{a} \\ \dot{b} \end{bmatrix} + \boldsymbol{K_f} \begin{bmatrix} a \\ b \end{bmatrix} = \boldsymbol{F_f}, \tag{3.11}$$

where a, b, $\boldsymbol{D_f} \in \mathbb{R}^{2\times2}$, $\boldsymbol{K_f} \in \mathbb{R}^{2\times2}$ and $\boldsymbol{F_f} \in \mathbb{R}^2$ are the lateral flapping angle, longitudinal flapping angle, flapping damping term, flapping stiffness term and

flapping forcing term respectively. $\boldsymbol{D_f}$ and $\boldsymbol{K_f}$ can be described as

$$\begin{aligned}\boldsymbol{D_f} &= \Omega\begin{bmatrix}\frac{\gamma}{8} & 2\\ -2 & \frac{\gamma}{8}\end{bmatrix},\\ \boldsymbol{K_f} &= \Omega^2\begin{bmatrix}\frac{k_\beta}{J_\beta\Omega^2} & \frac{\gamma}{8}\\ \frac{\gamma}{8} & \frac{k_\beta}{J_\beta\Omega^2}\end{bmatrix},\end{aligned} \tag{3.12}$$

where, k_β, J_β and γ are blade spring stiffness, blade moment of inertia about the flapping axis and blade Lock number respectively, where (Mettler et al., 2002)

$$\gamma = \frac{\rho c C_l(\alpha) R^4}{J_\beta}. \tag{3.13}$$

The rotor forcing term, $\boldsymbol{F_f}$, can be defined using a first order TPP model

$$\boldsymbol{F_f} = \Omega^2\begin{bmatrix}\frac{\gamma}{8} & 0\\ 0 & \frac{\gamma}{8}\end{bmatrix}\begin{bmatrix}A_1\\ B_1\end{bmatrix} + \Omega\begin{bmatrix}-2 & -\frac{\gamma}{8}\\ -\frac{\gamma}{8} & 2\end{bmatrix}\begin{bmatrix}p\\ q\end{bmatrix} + \begin{bmatrix}0 & -1\\ -1 & 0\end{bmatrix}\begin{bmatrix}\dot{p}\\ \dot{q}\end{bmatrix}, \tag{3.14}$$

where A_1 and B_1 are lateral and longitudinal swashplate angles respectively. By dropping the second order term from Equation (3.11), first order TPP equations of motion can be obtained (Tischler and Cauffman, 1992; Mettler et al., 2002; Mettler, 2003)

$$\begin{aligned}\frac{16}{\gamma\Omega}\dot{a} &= -a - \frac{16}{\gamma\Omega}q + \frac{p}{\Omega} + \frac{8k_\beta}{\gamma\Omega^2 J_\beta}b - B_1,\\ \frac{16}{\gamma\Omega}\dot{b} &= -b - \frac{16}{\gamma\Omega}p + \frac{q}{\Omega} - \frac{8k_\beta}{\gamma\Omega^2 J_\beta}a - A_1.\end{aligned} \tag{3.15}$$

By defining the flapping time constant, τ_f, and augmented cyclic inputs, $A_{lat}\delta_{lat}$, $A_{lon}\delta_{lon}$, $B_{lat}\delta_{lat}$ and $B_{lon}\delta_{lon}$ as

$$\begin{aligned}\tau_f &= \frac{16}{\gamma\Omega},\\ A_{lat}\delta_{lat} + A_{lon}\delta_{lon} &= -B_1,\\ B_{lat}\delta_{lat} + B_{lon}\delta_{lon} &= -A_1,\end{aligned} \tag{3.16}$$

a simplified first order TPP approximation of rotor flapping dynamics can be obtained

$$\begin{aligned} \tau_f \dot{b} &= -b - \tau_f p - B_a a + B_{lat}\delta_{lat} + B_{lon}\delta_{lon}, \\ \tau_f \dot{a} &= -a - \tau_f q - A_b b + A_{lat}\delta_{lat} + A_{lon}\delta_{lon}, \end{aligned} \tag{3.17}$$

where $A_{b,lat,lon}$, $B_{a,lat,lon}$, and $\delta_{lat,lon}$ are lateral flapping derivatives, longitudinal flapping derivatives and cyclic control inputs respectively. This first order approximation captures the cross coupling between lateral and longitudinal cyclic control inputs, rotor flapping and rotation of the helicopter body. It has been used extensively in the literature by Tischler and Cauffman (1992), Mettler et al. (2002) and Mettler (2003). Note also that Mettler et al. (2002) have shown that Equation (3.17) can be extended to include stabiliser bar dynamics, however, this is not required for the test-bed used in this research.

3.1.4 Complete Hovering Dynamics Model with Exogenous Disturbance Dynamics

In this subsection, a complete linear model of a micro helicopter's hovering dynamics, of the form described by Equation (2.22), is outlined. The complete model includes the rotor flapping dynamics described by Equation (3.17). Additionally, the effect of exogenous force and torque disturbances on helicopter hovering dynamics are included in the model.

The state vector, $\boldsymbol{x}$, is extended to include the lateral and longitudinal flapping angle states, becoming

$$\boldsymbol{x} = \begin{bmatrix} u & v & p & q & \phi & \theta & a & b & w & r \end{bmatrix}^T. \tag{3.18}$$

Additionally, the state matrix, $\boldsymbol{A}$, is also extended to the include the flapping dynamics described by Equation (3.17)

$$\boldsymbol{A} = \begin{bmatrix} X_u & 0 & 0 & 0 & 0 & -g & X_a & 0 & 0 & 0 \\ 0 & Y_v & 0 & 0 & g & 0 & 0 & Y_b & 0 & 0 \\ L_u & L_v & 0 & 0 & 0 & 0 & 0 & L_b & 0 & 0 \\ M_u & M_v & 0 & 0 & 0 & 0 & M_a & 0 & 0 & 0 \\ 0 & 0 & 1 & 0 & 0 & 0 & 0 & 0 & 0 & 0 \\ 0 & 0 & 0 & 1 & 0 & 0 & 0 & 0 & 0 & 0 \\ 0 & 0 & 0 & -1 & 0 & 0 & \frac{-1}{\tau_f} & \frac{A_b}{\tau_f} & 0 & 0 \\ 0 & 0 & -1 & 0 & 0 & 0 & \frac{B_a}{\tau_f} & \frac{-1}{\tau_f} & 0 & 0 \\ 0 & 0 & 0 & 0 & 0 & 0 & Z_a & Z_b & Z_w & Z_r \\ 0 & 0 & 0 & 0 & 0 & 0 & 0 & 0 & N_w & N_r \end{bmatrix}, \tag{3.19}$$

where two additional rows and columns have been added to the state matrix previously shown in Equation (3.10) to account for rotor flapping dynamics. The input vector, $\boldsymbol{u}$, is made up of control commands provided by the pilot

$$\boldsymbol{u} = \begin{bmatrix} \delta_{lat} & \delta_{lon} & \delta_{yaw} & \delta_{col} \end{bmatrix}^T, \tag{3.20}$$

and the input matrix, $\boldsymbol{B_u}$, considers the dominant control derivatives (Mettler et al., 2002)

$$\boldsymbol{B_u} = \begin{bmatrix} 0 & 0 & 0 & 0 \\ 0 & 0 & 0 & 0 \\ 0 & 0 & 0 & 0 \\ 0 & 0 & 0 & 0 \\ 0 & 0 & 0 & 0 \\ 0 & 0 & 0 & 0 \\ \frac{A_{lat}}{\tau_f} & \frac{A_{lon}}{\tau_f} & 0 & 0 \\ \frac{B_{lat}}{\tau_f} & \frac{B_{lon}}{\tau_f} & 0 & 0 \\ 0 & 0 & 0 & Z_{col} \\ 0 & 0 & N_{yaw} & N_{col} \end{bmatrix}. \tag{3.21}$$

Finally, the disturbance vector, $\boldsymbol{d}$, is made up of the exogenous force and torque disturbances

$$\boldsymbol{d} = \begin{bmatrix} \overline{X} & \overline{Y} & \overline{Z} & \overline{L} & \overline{M} & \overline{N} \end{bmatrix}^T, \tag{3.22}$$

where the disturbance matrix, $\boldsymbol{B_d}$, is

$$\boldsymbol{B_d} = \begin{bmatrix} \frac{1}{m} & 0 & 0 & 0 & 0 & 0 \\ 0 & \frac{1}{m} & 0 & 0 & 0 & 0 \\ 0 & 0 & 0 & \frac{1}{J_{xx}} & 0 & 0 \\ 0 & 0 & 0 & 0 & \frac{1}{J_{yy}} & 0 \\ 0 & 0 & 0 & 0 & 0 & 0 \\ 0 & 0 & 0 & 0 & 0 & 0 \\ 0 & 0 & 0 & 0 & 0 & 0 \\ 0 & 0 & 0 & 0 & 0 & 0 \\ 0 & 0 & \frac{1}{m} & 0 & 0 & 0 \\ 0 & 0 & 0 & 0 & 0 & \frac{1}{J_{zz}} \end{bmatrix}, \tag{3.23}$$

where $\boldsymbol{B_d}$ describes how exogenous force and torque disturbances affect translational and rotational accelerations of the helicopter.

It is important to note that the helicopter hovering dynamics described in this subsection show that exogenous force and torque disturbances will directly alter translational and rotational acceleration states. In the case of helicopter hovering in a confined environment (i.e., in close proximity to planar surfaces), these force and torque disturbances will be induced by fluid interactions between the helicopter main rotor and nearby obstacles. An investigation of the physical nature of these disturbances is outlined in Chapters 4, 5, 6 and 7 and a method for estimating these disturbances during flight (based on the model derived in this section) is presented in Chapter 8.

3.1.5 Output Dynamics

As discussed in Chapter 1, this research relies on using MEMS inertial sensors to measure helicopter states. Translational accelerations and angular velocities can be directly measured using MEMS accelerometers and gyroscopes. Additionally, roll and pitch attitude angles can be readily estimated from the accelerometer and

gyroscope measurements, as will be shown in Section 3.2.2.1. With this in mind, the output vector for a helicopter relying only on inertial sensors will be

$$\boldsymbol{y} = \begin{bmatrix} \dot{u} & \dot{v} & \dot{w} & p & q & r & \phi & \theta \end{bmatrix}. \tag{3.24}$$

The associated output dynamics are governed by the output matrix

$$\boldsymbol{C} = \begin{bmatrix} X_u & 0 & 0 & 0 & 0 & -g & X_a & 0 & 0 & 0 \\ 0 & Y_v & 0 & 0 & g & 0 & 0 & Y_b & 0 & 0 \\ 0 & 0 & 0 & 0 & 0 & 0 & Z_a & Z_b & Z_w & Z_r \\ 0 & 0 & 1 & 0 & 0 & 0 & 0 & 0 & 0 & 0 \\ 0 & 0 & 0 & 1 & 0 & 0 & 0 & 0 & 0 & 0 \\ 0 & 0 & 0 & 0 & 0 & 0 & 0 & 0 & 0 & 1 \\ 0 & 0 & 0 & 0 & 1 & 0 & 0 & 0 & 0 & 0 \\ 0 & 0 & 0 & 0 & 0 & 1 & 0 & 0 & 0 & 0 \end{bmatrix}, \tag{3.25}$$

the input feed-through matrix

$$\boldsymbol{D_u} = \begin{bmatrix} 0 & 0 & 0 & 0 \\ 0 & 0 & 0 & 0 \\ 0 & 0 & 0 & Z_{col} \\ 0 & 0 & 0 & 0 \\ 0 & 0 & 0 & 0 \\ 0 & 0 & 0 & 0 \\ 0 & 0 & 0 & 0 \\ 0 & 0 & 0 & 0 \end{bmatrix}, \tag{3.26}$$

and the disturbance feed-through matrix

$$\boldsymbol{D_d} = \begin{bmatrix} \frac{1}{m} & 0 & 0 & 0 & 0 & 0 \\ 0 & \frac{1}{m} & 0 & 0 & 0 & 0 \\ 0 & 0 & \frac{1}{m} & 0 & 0 & 0 \\ 0 & 0 & 0 & 0 & 0 & 0 \\ 0 & 0 & 0 & 0 & 0 & 0 \\ 0 & 0 & 0 & 0 & 0 & 0 \\ 0 & 0 & 0 & 0 & 0 & 0 \\ 0 & 0 & 0 & 0 & 0 & 0 \end{bmatrix}. \tag{3.27}$$

Note that $\boldsymbol{D_u}$ and $\boldsymbol{D_d}$ are both non-zero because force control inputs and exogenous disturbances feed-through directly to measured acceleration states. As will be outlined in Chapter 8, it is important to consider this direct feed-through when designing a state or disturbance estimator for a micro helicopter that relies only on on-board inertial sensors.

3.2 Overview of Micro Helicopter Test-Bed

The micro helicopter test-bed used in this research is the commercially available Blade Nano CPX helicopter (Horizon Hobby, Inc., 2012). For the benefit of the reader, an overview of the test-bed is provided in this section. Model parameters for the test-bed are identified in Section 3.3. A detailed exploded view of the test-bed with major components labelled is provided in Figure 3.3. The test-bed has a single main rotor and a tail rotor. The main rotor has a radius of 103 mm and is powered by a micro brushed DC motor located in the main body of the fuselage. The tail rotor has a radius of 20 mm and is powered by a micro brushed DC motor located at the end of the tail boom. Thrust is controlled by varying the collective pitch of the main rotor and pitch/roll motion is controlled by varying the cyclic pitch of the main rotor. Three micro servos actuate the swashplate in a 120° collective-cyclic pitch mixing (CCPM) arrangement (Alexis et al., 2013) in order to control main rotor collective pitch and cyclic pitch simultaneously. Power to the helicopter is provided by a 3.7 V 150 mAh lithium polymer battery. The total mass of the

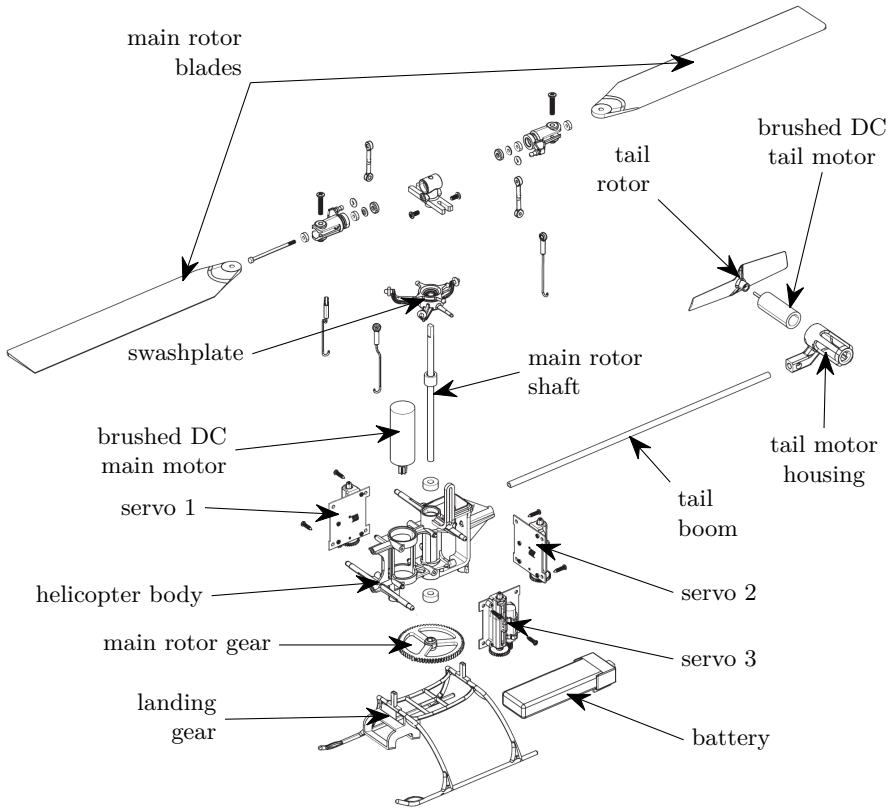

Figure 3.3: Exploded view of Blade Nano CPX helicopter (reproduced from Horizon Hobby, Inc. (2012)). Major components are labelled.

test-bed (including battery and the additional modifications listed in Section 3.2.1) is 35.62 g.

The test-bed is manually controlled by a human pilot via control commands that are input through a ground station computer. Accelerometer and gyroscope sensors on-board the test-bed are sampled at 200 Hz and are logged in real time at the ground station computer. Additionally, the test-bed can be tracked by a motion capture system to provide a high accuracy estimate of the test-bed's position and orientation.

3.2.1 Hardware Modifications

Modifications have been made to the Blade Nano CPX helicopter to allow for custom designed control systems to be implemented and to allow for position, orientation and inertial data to be logged in real time. Hardware modifications include:

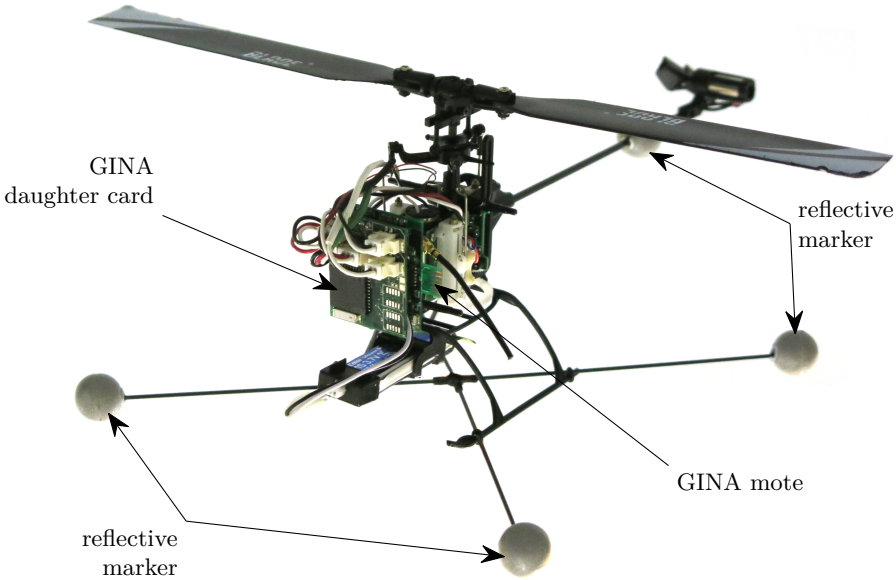

FIGURE 3.4: Photograph of micro helicopter test-bed with hardware modifications labelled. Note that there is a fifth reflective marker that is obscured by the body of the helicopter in this image.

1. Use of a Guidance and Inertial Navigation Assistant (GINA) mote to implement on-board control systems, MEMS sensor measurement and radio communication with the ground station computer (as outlined in Section 3.2.1.1).

2. Use of a GINA daughtercard to power and control the brushed DC motors and micro servos (as outlined in Section 3.2.1.2).

3. Use of reflective markers (as outlined in Section 3.2.1.3) to enable the use of an infra-red camera motion capture system for position and orientation measurement.

These modifications are outlined in detail throughout this subsection and are shown in the photograph provided in Figure 3.4.

3.2.1.1 Guidance and Inertial Navigation Assistant (GINA)

The GINA mote, developed by Mehta et al. (2012), has been selected as the primary avionics platform for this research. It is suitable for MAV inertial measurement and

control because it is ultra lightweight, fitting within the test-bed's small payload capacity, while still providing the required sensor, wireless communication, actuation and computation capabilities. Furthermore, the GINA firmware and software are fully open source and can therefore be modified to suit a range of different applications. The GINA mote is 26 mm by 27 mm, weighs 1.67 g and accommodates the following components:

- Texas Instruments MSP430F2618 microcontroller (Bierl, 2000)
- Kionix KXSD9-1026 triple axis digital accelerometer (Kionix, 2010)
- ST LIS344ALH triple axis analogue accelerometer (STMicroelectronics, 2008)
- InvenSense ITG3200 triple axis digital gyroscope (InvenSense, Inc., 2011)
- Honeywell HMC5843 triple axis digital magnetometer (Honeywell, 2010)
- Texas Instruments TMP20 analogue temperature sensor (Texas Instruments, 2009)
- Atmel AT86RF231 radio transceiver (Atmel Corporation, 2009)

Additionally, the GINA mote has 24 male pins for interfacing with the GINA daughter card, outlined in Section 3.2.1.2. Power is provided from a 3.7 V lithium polymer battery via the GINA daughter card. A photograph of the GINA mote is provided in Figure 3.5. The GINA mote is mounted to the front of the test-bed as shown in Figure 3.4.

3.2.1.2 GINA Daughter Card

The GINA daughter card is a 26 mm by 22 mm card with a mass of 1.89 g that interfaces directly with the GINA mote. The daughter card can pass three separate pulse width modulation (PWM) signals directly from the GINA mote to three servo motors. Additionally, the daughter card can pass two separate PWM signals directly to two Vishay SIA414DJ-T1 MOSFET transistors (Vishay Siliconix, 2012) which can regulate power supply to two brushed DC motors. A GPS chip is also accommodated on-board the daughter card, however, this is not utilised in this

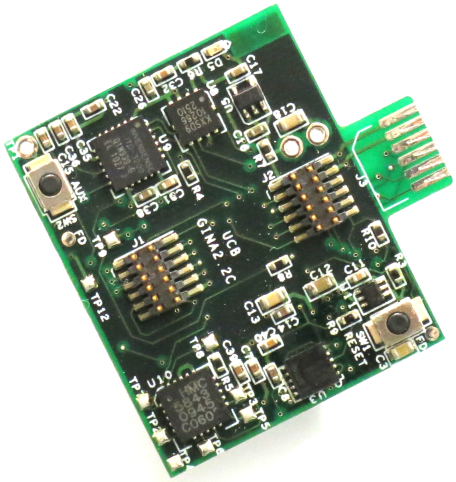

FIGURE 3.5: Photograph of Guidance and Inertial Navigation Assistant (GINA) mote.

research. A photograph of the daughter card is provided in Figure 3.6 and the position of the daughter card on top of the GINA mote is shown in Figure 3.4.

3.2.1.3 Reflective Markers

The final hardware modification is the inclusion of five reflective markers on-board the test-bed. These markers are designed to reflect infra-red light to allow the test-bed to be tracked by the motion capture camera system described in Section 3.2.4. The markers are spherical with a radius of 6 mm and are covered with 3M 7610 reflective tape (3M Industrial Business, 2003). Four of the markers are attached to a cross-shaped structure mounted to the test-bed's landing gear. The fifth marker is attached to the tail boom of the test-bed. This arrangement can be seen in the photograph provided in Figure 3.4.

3.2.2 Firmware

Firmware has been programmed to the micro controller on-board the GINA mote to manage the following key functions:

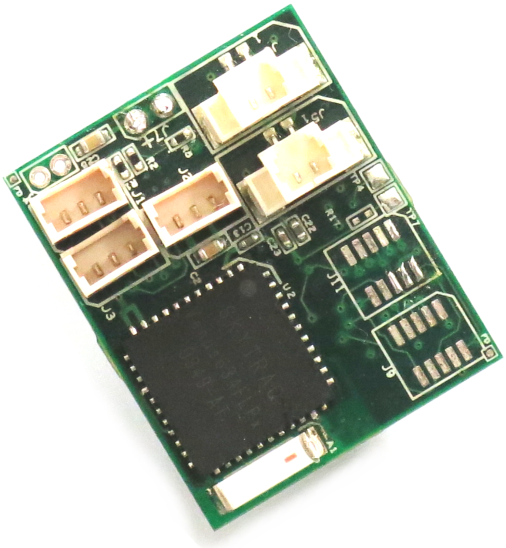

Figure 3.6: Photograph of Guidance and Inertial Navigation Assistant (GINA) daughter card.

- Calibrating sensor biases
- Reading sensor data
- Estimating attitude based on measured sensor data (outlined further in Section 3.2.2.1)
- Receiving pilot commands from the ground station computer
- Calculating attitude control output (outlined further in Section 3.2.2.2)
- Calculating yaw-rate control output (outlined further in Section 3.2.2.3)
- Updating servo and motor PWM signals based on pilot commands and sensor data (outlined further in Section 3.2.2.4)
- Transmitting sensor data back to the ground station computer

A flow chart illustrating the implementation of these tasks in the GINA mote firmware is provided in Figure 3.7. Note that the main control loop operates at 200 Hz. Data is sent to and received from the ground station computer every fourth

time the firmware enters the main control loop, i.e., at 50 Hz. The program starts when power is supplied to the GINA mote and will continue looping until power is disconnected. The firmware is written entirely in C and utilises the WARPWING libraries, developed at UC Berkeley (Mehta and Pister, 2010).

3.2.2.1 Attitude Filter

An attitude filter is a state estimation scheme that estimates roll and pitch angles based on gyroscope and accelerometer data. Such a filter is necessary on-board a micro helicopter in order to autonomously stabilise pitch and roll angles during flight. As previously outlined in Section 2.3.1, a variety of different state estimation techniques have been used in the literature for implementing attitude filters, including: complementary filtering, the gradient descent algorithm and Kalman filtering. In this research, the complementary filter is used, primarily because of its low computational cost and ease of implementation. The complementary filter first calculates separate attitude estimates from the accelerometer measurements and the gyroscope measurements

$$\begin{aligned}
\hat{\phi}_{k,\text{acc}} &= \text{atan}\left(\frac{a_y}{\sqrt{a_x^2 + a_z^2}}\right), \\
\hat{\theta}_{k,\text{acc}} &= \text{atan}\left(\frac{a_x}{\sqrt{a_y^2 + a_z^2}}\right), \\
\hat{\phi}_{k,\text{gyr}} &= \hat{\phi}_{k-1,\text{gyr}} + g_x \Delta t, \\
\hat{\theta}_{k,\text{gyr}} &= \hat{\theta}_{k-1,\text{gyr}} + g_y \Delta t,
\end{aligned} \tag{3.28}$$

where $\hat{\phi}_{\text{acc}}$, $\hat{\theta}_{\text{acc}}$, $\hat{\phi}_{\text{gyr}}$, $\hat{\phi}_{\text{gyr}}$, a_x, a_y, a_z, g_x, g_y, k, Δt are the accelerometer roll estimate, accelerometer pitch estimate, gyroscope roll estimate, gyroscope pitch estimate, x-axis accelerometer measurement, y-axis accelerometer measurement, z-axis accelerometer measurement, x-axis gyroscope measurement, y-axis gyroscope measurement, time-step number and time step size respectively. Note that the attitude estimates made from the accelerometer measurements are typically very noisy due to electromagnetic noise induced by the brushed DC motor. Additionally,

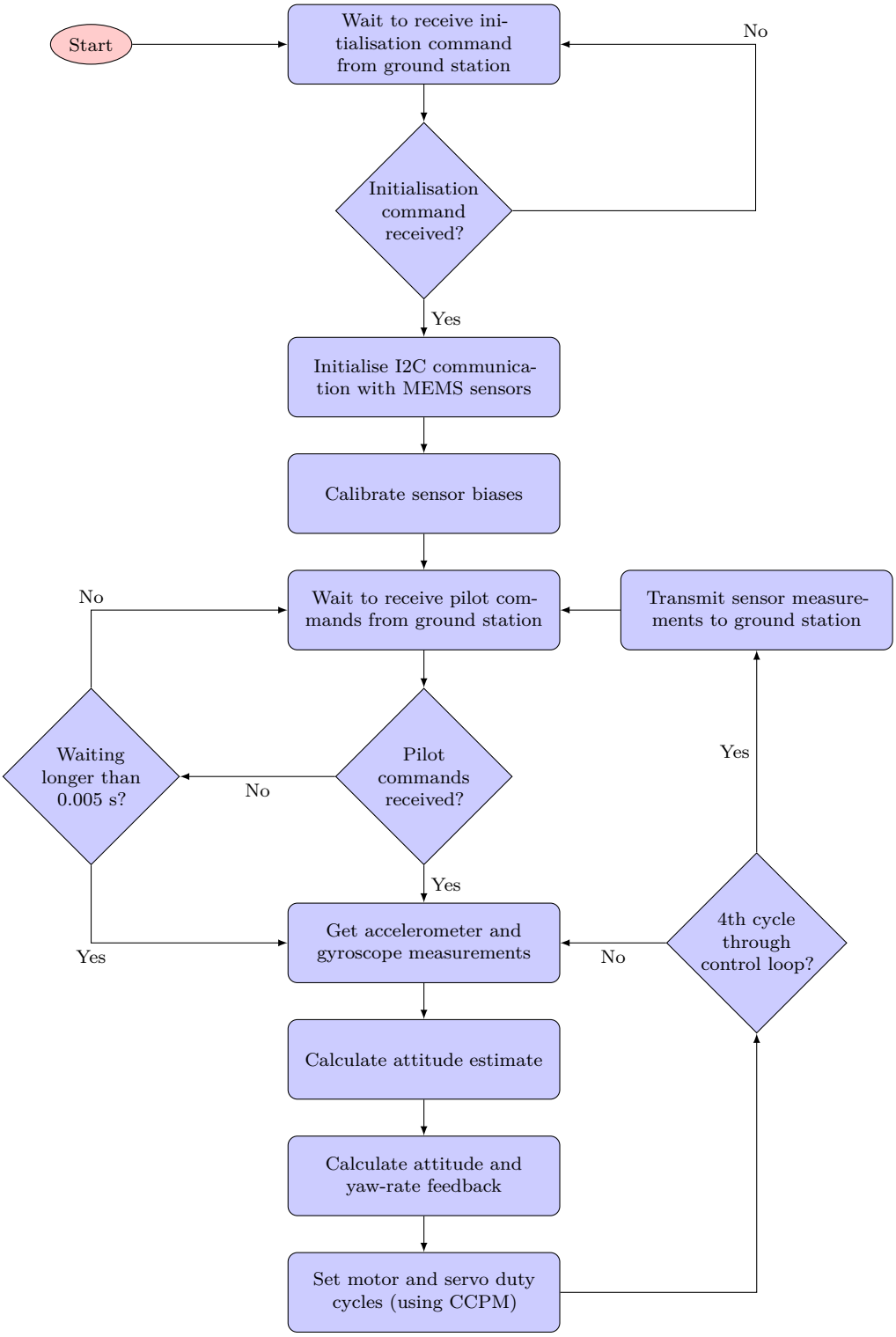

Figure 3.7: Flowchart illustrating the functions implemented in firmware on-board the GINA mote.

the attitude estimates made from the gyroscope measurements are susceptible to unbounded drift due to numerical integration of gyroscope biases. To address this, the complementary lter merges the two estimates by rst passing the accelerometer estimate through a low pass lter and the gyroscope estimate through a high pass lter

$$\begin{aligned} \hat{\ }_k &= {}_c\hat{\ }_{k\ 1} \quad 1 \quad {}_c\hat{\ }_{k;acc} \quad {}_c\hat{\ }_{k;gyr} \quad t; \\ \hat{\ }_k &= {}_c\hat{\ }_{k\ 1} \quad 1 \quad {}_c\hat{\ }_{k;acc} \quad {}_c\hat{\ }_{k;gyr} \quad t; \end{aligned} \tag{3.29}$$

where ^ and ^ are the complementary ltered roll estimate and complementary ltered pitch estimate respectively and

$$_c \quad \frac{2}{!_c \quad t} \quad 1 \quad \frac{2}{!_c \quad t} \quad ; \tag{3.30}$$

where the complementary lter cut-o frequency, $!_c$, is set to 2040 rad/s in order to maintain a balance between lter response time and noise attenuation.

The performance of the complementary lter has been assessed experimentally by recording complementary ltered attitude estimates during ight and comparing these with attitude measurements obtained using the motion capture system outlined in Section 3.2.4. Plots of pitch and roll estimates against time over 50 s of ight data are provided in Figures 3.8(a) and 3.8(b) respectively. For the roll estimate, root mean square (RMS) error and peak error are 0:05 rad and 0:30 rad respectively. For the pitch estimate, RMS error and peak error are 0:06 rad and 0:21 rad respectively.

3.2.2.2 Attitude Control

The low inertia of the micro helicopter test-bed, along with the fast response time provided by the variable pitch rotor will cause the micro helicopter test-bed to respond quickly to pilot inputs. Further to this, the test-bed does not have a stabiliser bar (commonly used on other micro helicopters (Conroy et al., 2011)) and, therefore, will not self-regulate its attitude. These factors make the test-bed inherently di cult for a human pilot to control. To address this, a simple decoupled proportional attitude feedback control law is used to regulate helicopter attitude

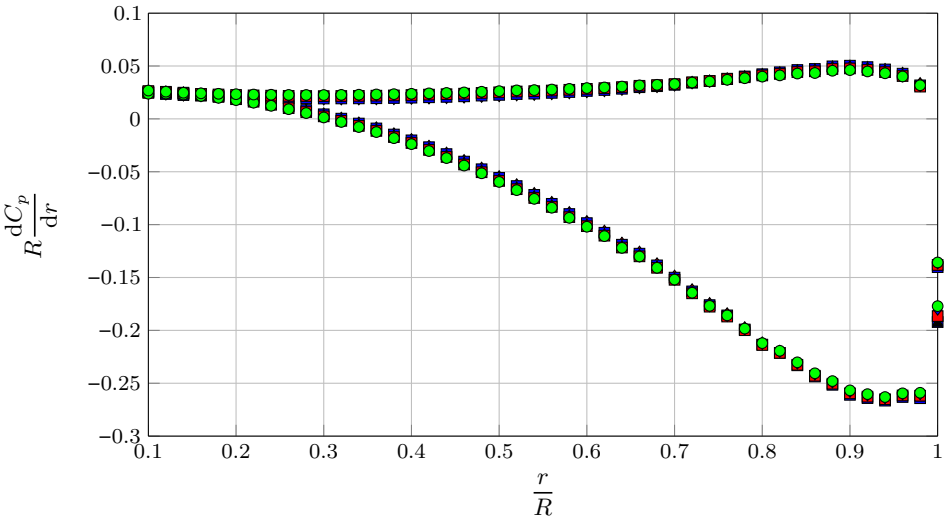

(a) Sectional pressure coefficient vs non-dimensionalised spanwise distance at ϕ_w = 0°.

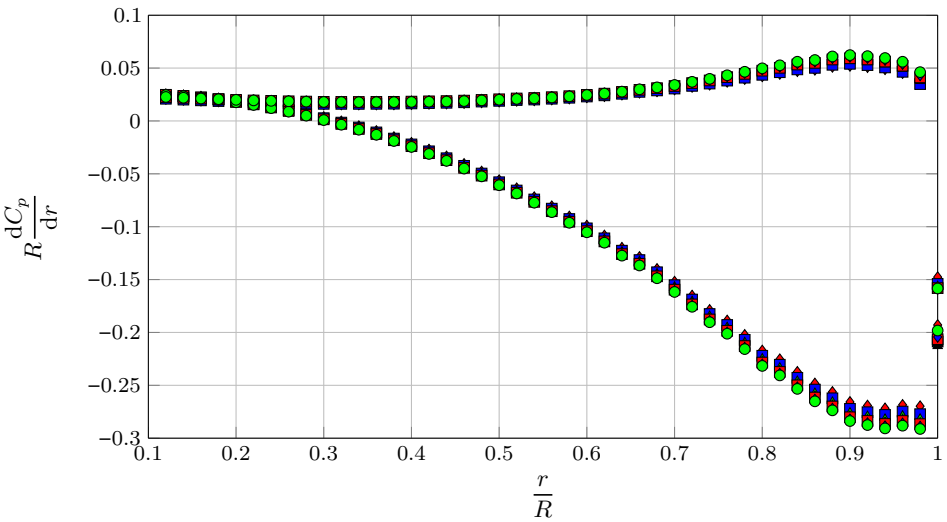

(b) Sectional pressure coefficient vs non-dimensionalised spanwise distance at ϕ_w = 180°.

Baseline ●	h_w/R = 3.14 ♦	h_w/R = 2.75 ■	h_w/R = 2.36 ▲
h_w/R = 2.17 ▲	h_w/R = 1.97 ■	h_w/R = 1.78 ♦	h_w/R = 1.58 ●

FIGURE 7.23: Effect of rotor-wall gap on sectional pressure coefficient. Positive pressure and negative pressure occur at bottom surface and top surface of the blade respectively.

in sectional thrust that occurs near the blade tip is driven by the increase in induced velocity and decrease in local effective angle of attack that occur near the blade tip. For the ϕ_w = 180° blade position, sectional thrust coefficient increases across the entire blade span. This is because the induced velocity decreases across the entire blade span at the far-wall side of the rotor disk. The increase in sectional thrust

is largest toward the blade tip. This occurs because the incident flow velocity is highest toward the blade tip. From Figures 7.24(a) and 7.24(b) it is clear that the fluid interactions with the wall induce an imbalance in thrust across the rotor disk. There is a significant increase in thrust at the far-wall side of the rotor, compared to a relatively minor change in blade loading at the near-wall side of the rotor. This thrust imbalance drives the change in torque ratio about the y-axis that was previously shown in Figure 7.7.

Sectional power coefficient for the $\phi_w = 0^\circ$ and $\phi_w = 180^\circ$ blade positions is plotted against non-dimensionalised spanwise distance in Figures 7.25(a) and 7.25(b) respectively. For the $\phi_w = 0^\circ$ blade position, there is a small increase in power coefficient across the entire blade span as rotor-wall gap decreases. At a spanwise distance of $r/R = 0.98$ and a rotor-wall gap of $h_w/R = 1.58$, the increase in sectional power coefficient is only 4%. For the $\phi_w = 180^\circ$ blade position, there is a more significant increase in power coefficient across the entire blade span as rotor-wall gap decreases. At a spanwise distance of $r/R = 0.98$ and a rotor-wall gap of $h_w/R = 1.58$, the increase in sectional power coefficient is 17%. These spanwise sectional power coefficient results show that the increase in power ratio previously shown in Figure 7.4(b) is dominated by an increase in blade power loading at the far-wall side of the rotor disk.

7.2 Discussion

7.2.1 Relationship Between Torque Disturbances and Rotor-Wall Gap

The thrust, power and torque results presented in Section 7.1.1 demonstrate that the dominant disturbance that is induced by fluid interactions between a hovering micro rotor and a wall plane is a torque disturbance about the global reference frame y-axis. In this section, the effect of changes in this torque disturbance on the helicopter hovering dynamics identified in Section 3.3 is discussed. This relationship between torque disturbance and hovering dynamics is important to understand in order to control a micro helicopter in close proximity to a wall plane. The variation

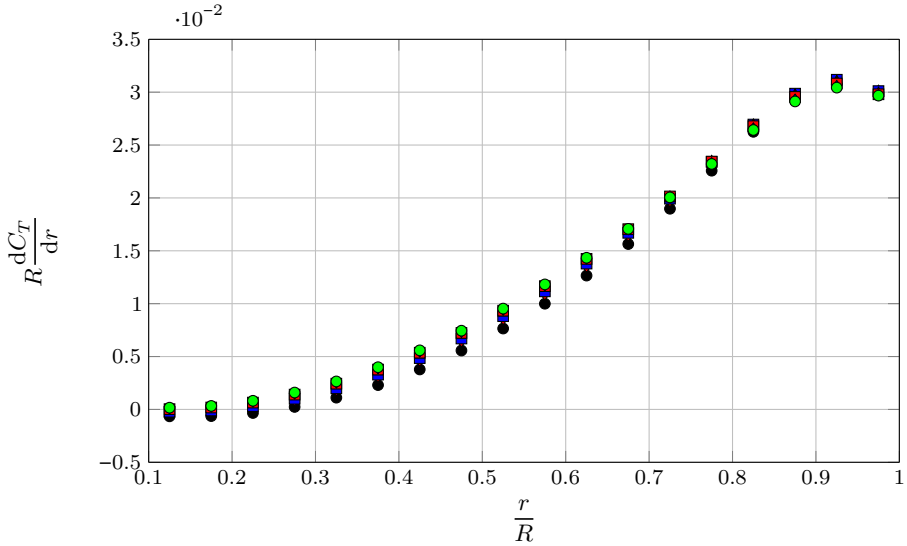

(a) Sectional thrust coefficient vs non-dimensionalised spanwise distance at $\phi_w = 0^\circ$.

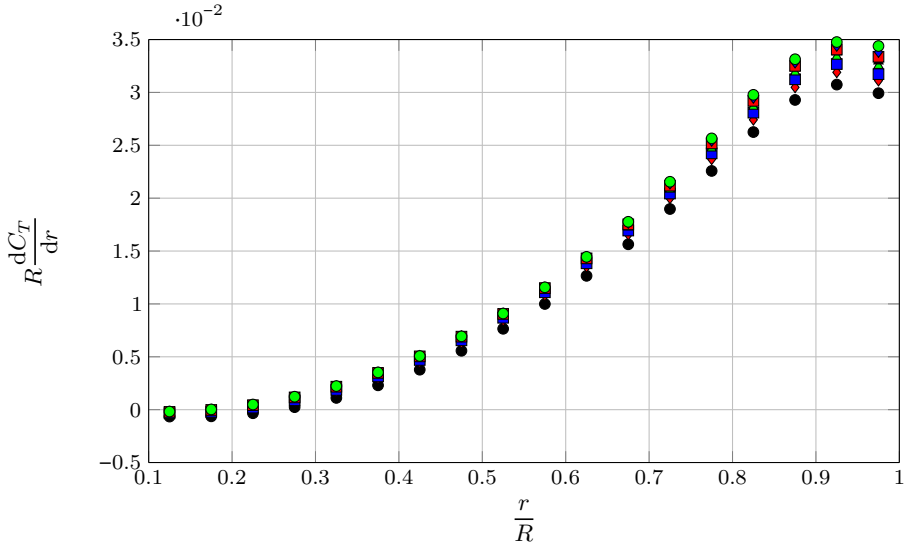

(b) Sectional thrust coefficient vs non-dimensionalised spanwise distance at $\phi_w = 180^\circ$.

Baseline ●	$h_w/R = 3.14$ ♦	$h_w/R = 2.75$ ■	$h_w/R = 2.36$ ▲
$h_w/R = 2.17$ ▲	$h_w/R = 1.97$ ■	$h_w/R = 1.78$ ♦	$h_w/R = 1.58$ ●

FIGURE 7.24: Effect of rotor-wall gap on sectional thrust across blade span.

in y-axis torque ratio shown in Figure 7.7(b) will generate torque disturbances about the helicopter's body-fixed x-axis, $\overline{L}$, and y-axis, $\overline{N}$, defined in Figure 2.14

$$\begin{aligned} \overline{L} &= \sin(\psi_w)\, Q_y, \\ \overline{M} &= \cos(\psi_w)\, Q_y, \end{aligned} \tag{7.3}$$

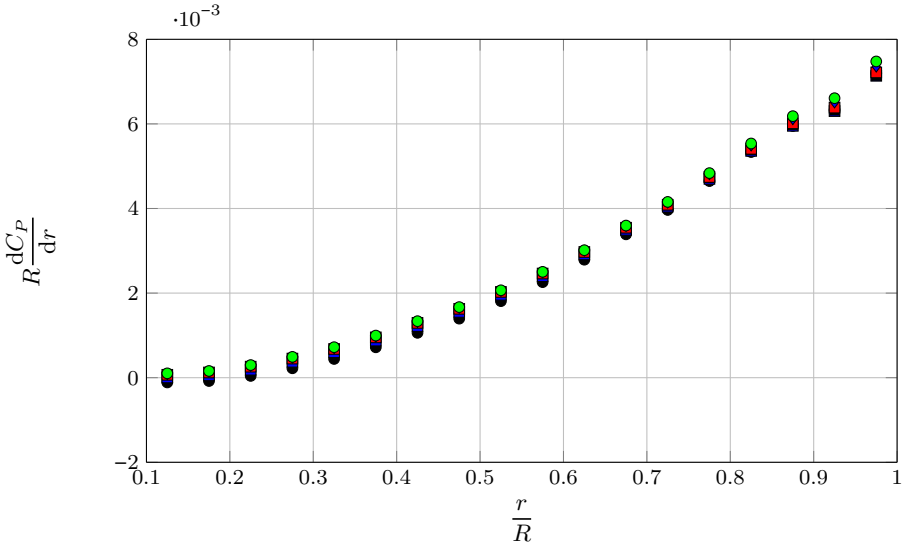

(a) Sectional power coefficient vs non-dimensionalised spanwise distance at ϕ_w = 0°.

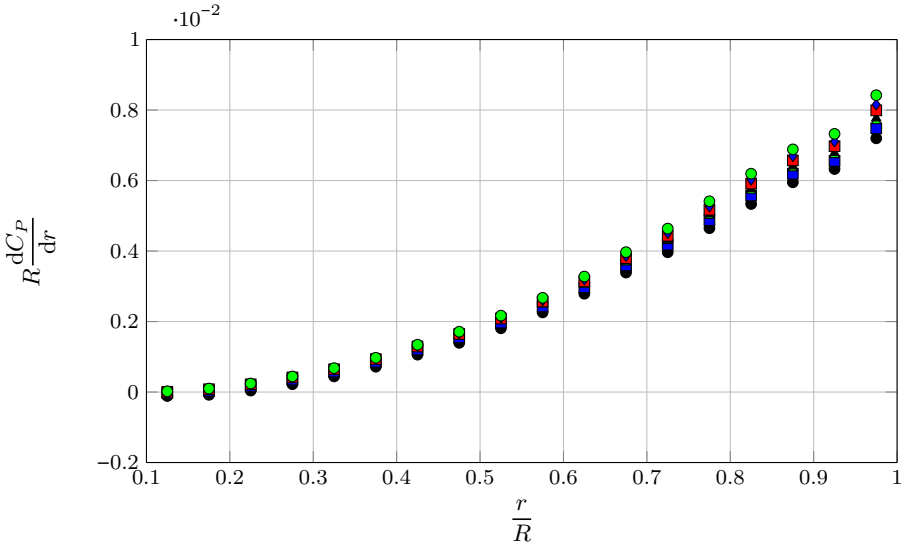

(b) Sectional power coefficient vs non-dimensionalised spanwise distance at ϕ_w = 180°.

Baseline ●	h_w/R = 3.14 ♦	h_w/R = 2.75 ■	h_w/R = 2.36 ▲
h_w/R = 2.17 ▲	h_w/R = 1.97 ■	h_w/R = 1.78 ♦	h_w/R = 1.58 ●

Figure 7.25: Effect of rotor-wall gap on sectional power across blade span.

where Q_y is transformed from the global reference frame to the helicopter body-fixed frame using the helicopter-wall angle, ψ_w, as defined in Figure 7.26. In order to quantify the effect that these exogenous disturbances will have on helicopter hovering dynamics, it is useful to characterise the relationship between $\overline{L}$, $\overline{M}$ and wall proximity

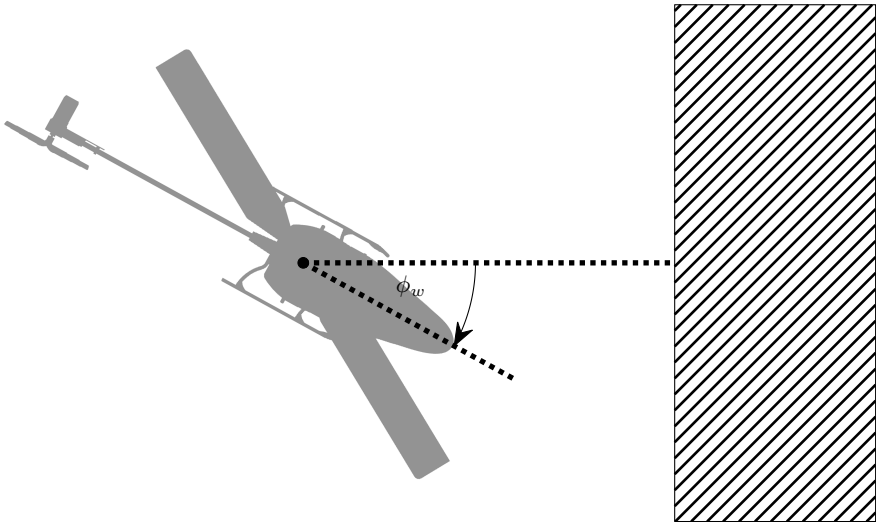

FIGURE 7.26: Schematic of helicopter-wall angle, ψ_w.

$$\begin{aligned} \overline{L} &\approx -\sin\left(\psi_w\right) Q' \cdot 0.1283 \left(\frac{h_w}{R} - 1\right)^{-1.164}, \\ \overline{M} &\approx -\cos\left(\psi_w\right) Q' \cdot 0.1283 \left(\frac{h_w}{R} - 1\right)^{-1.164}, \end{aligned} \tag{7.4}$$

where the power laws described by Equation (7.4) have been fitted to the CFD results using least squares regression with a R^2 value of 0.90776. Note that Equation (7.4) will tend to infinity as h_w tends to one. Clearly, this is a non physical result. With this in mind, it is important to acknowledge that the relationship described by Equation (7.4) will only be valid when the rotor is outside of the wall boundary layer.

As shown in Section 3.1.4, torque disturbances about a helicopter's body fixed x-axis and y-axis will feed-through directly to the roll-rate, p, and pitch-rate, q, states of the helicopter. Note also that the roll-rate and pitch-rate states are strongly coupled with a helicopter's horizontal translational velocities, u and v, and rotor flapping angles, a and b, through the stability derivatives X_a, Y_b, L_b and M_a. Therefore, exogenous torque disturbances induced by wall plane fluid interactions are likely to have a significant effect on a hovering helicopter's coupled lateral and longitudinal dynamics. Because a helicopter's horizontal translational velocity dynamics are unstable (as demonstrated by the unstable pair of eigenvalues listed in Table 3.2), these exogenous disturbances are likely to cause a helicopter

to collide with a wall plane if they are not adequately compensated for. As a first step toward implementing collision avoidance systems, in-flight estimation of exogenous disturbances induced by wall plane fluid interactions is outlined in detail in Section 8.3.3.

In the following subsections, the fluid interactions that drive the torque disturbance described by Equation (7.4) are discussed.

7.2.2 Blade Tip Vortex Interactions With a Wall Plane

As previously discussed in Section 6.2.2, it is important to understand the physical nature of fluid interactions between blade tip vortices and the wall plane because the induced velocity through the rotor disk is directly induced by vortex structures within the rotor wake. A representative schematic showing the effect that the near-wall flow field has on the structure of the blade tip vortex is provided in Figure 7.27. As highlighted in this figure, the blade tip vortex results previously presented in Section 7.1.3 show that there is an overall increase in the radial contraction and decrease in the vertical displacement of the blade tip vortex at the far-wall side of the rotor wake and there is a decrease in the radial contraction of the blade tip vortex at the near-wall side of the rotor wake. These changes in the blade tip vortex structure are driven by the near-wall flow field, i.e., flow moving predominantly parallel to the wall at the near-wall side of the flow field. At the far-wall side of the rotor, the increased radial contraction of the blade tip vortex induces a decrease in the vertical component of flow velocity near the blade tip. At the near-wall side of the rotor, the decreased radial contraction of the blade tip vortex causes an increase in the vertical component of induced velocity near the blade tip. Using BEMT (explained in detail in Section 2.2.3), these changes in induced velocity at opposite sides of the rotor can be shown to cause an increase in the thrust deficit across the rotor, i.e., more thrust will be generated at the far-wall side of the rotor. This deficit drives the torque about the global frame y-axis that was previously discussed in Section 7.2.1.

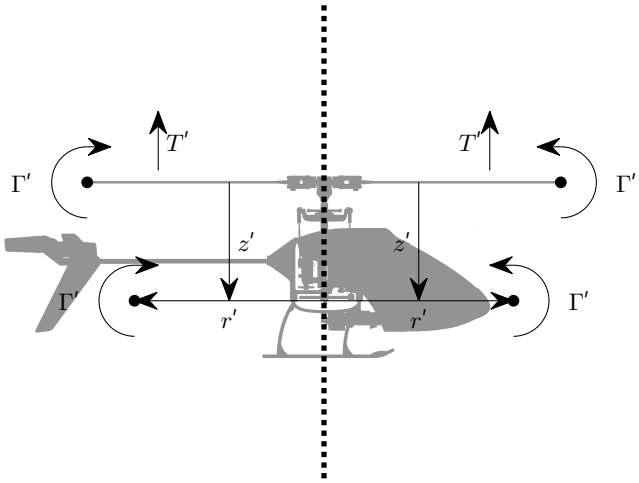

(a) Baseline case.

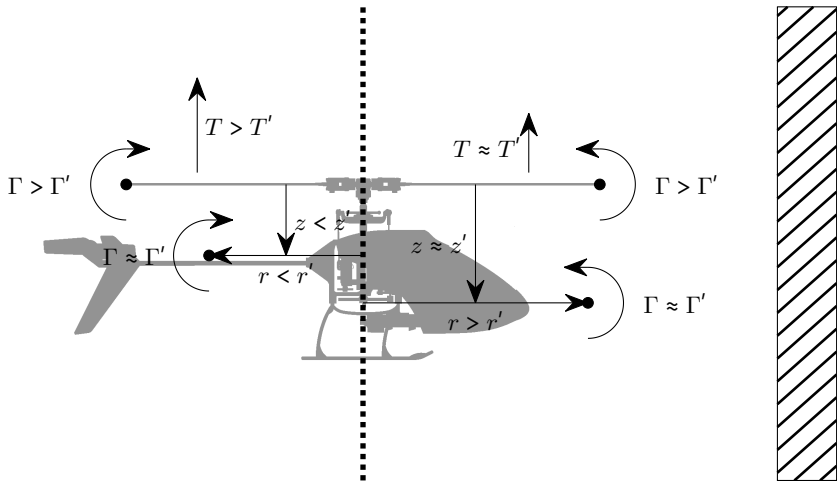

(b) Near-wall case.

FIGURE 7.27: Qualitative 2D schematic highlighting the relationship between the structure of the blade tip vortex and thrust for a hovering micro rotor in close proximity to a wall plane where T, Γ, r and z are thrust, circulation, radial position of vortex core, vertical position of vortex core and the superscript $(\cdot)'$ denotes values for the baseline case. The torque about the y-axis is generated by the imbalance between the thrust generated on opposite sides of the rotor.

7.2.3 Potential Flow Analysis of Near-Wall Flow Field

Further understanding of fluid interactions between a hovering micro rotor and an adjacent wall plane can be obtained by analysing the fundamental physical nature of a rotor wake near a wall. The flow field visualisations shown in Section 7.1.2 demonstrate that a wall plane in close proximity to a hovering micro rotor will alter the shape of the flow field through the rotor. In particular, when examining the flow

field through the rotor x-z plane (i.e., the vertical plane normal to the wall), the wall plane induces an increase in radial contraction of the flow field at the far-wall side of the wake and a decrease in radial contraction of the flow field at the near-wall side of the wake. In this section, the phase averaged flow (through the x-z plane) induced by a micro rotor hovering near to a wall plane has been approximated by a 2D laminar potential flow model. The boundary conditions used for the near-wall potential flow model are based on the source-sink boundary condition previously described in Section 4.4. If the flux through the rotor disk (in m^2/s) is denoted $\dot{V}$, then the velocity at the far-wall side of the domain (i.e., the left side of the domain shown in Figure 7.28) can be defined as

$$\begin{aligned} u_{in,far} &= -\dot{V}\frac{r}{\sqrt{r^2+z^2}}\frac{\pi}{\left(\pi - \operatorname{atan}\left(R/z_{d,2}\sqrt{2}\right)\right)}, \\ w_{in,far} &= -\dot{V}\frac{z}{\sqrt{r^2+z^2}}\frac{\pi}{\left(\pi - \operatorname{atan}\left(R/z_{d,2}\sqrt{2}\right)\right)}, \end{aligned} \tag{7.5}$$

where $z_{d,2}$ is the domain height below the rotor plane. The velocity at the near-wall side of the domain (i.e., the right side of the domain shown in Figure 7.28) can be defined as

$$\begin{aligned} u_{in,near} &= -\dot{V}\frac{r}{\sqrt{r^2+z^2}}\frac{\pi}{\left(\pi - \operatorname{atan}\left(R/z_{d,2}\sqrt{2}\right) - \operatorname{atan}\left(z_{d,1}/h_w\right) - \operatorname{atan}\left(z_{d,2}/h_w\right)\right)}, \\ w_{in,near} &= -\dot{V}\frac{z}{\sqrt{r^2+z^2}}\frac{\pi}{\left(\pi - \operatorname{atan}\left(R/z_{d,2}\sqrt{2}\right) - \operatorname{atan}\left(z_{d,1}/h_w\right) - \operatorname{atan}\left(z_{d,1}/h_w\right)\right)}, \end{aligned} \tag{7.6}$$

where $z_{d,1}$ is the domain height above the rotor plane. Note that the velocity at the near-wall boundaries will be larger than at the far-wall boundaries because the near-wall boundaries are smaller (due to the presence of the wall). Therefore, velocity at the near wall boundary must be larger in order to provide equal flux through both sides of the 2D domain. At the outlet directly below the rotor (with a radius equal to $R/\sqrt{2}$), the velocity can be defined as

$$\begin{aligned} u_{out,near} &= 0, \\ w_{out,near} &= -\dot{V}\frac{\pi}{\operatorname{atan}\left(R/z_{d,2}\sqrt{2}\right)}. \end{aligned} \tag{7.7}$$

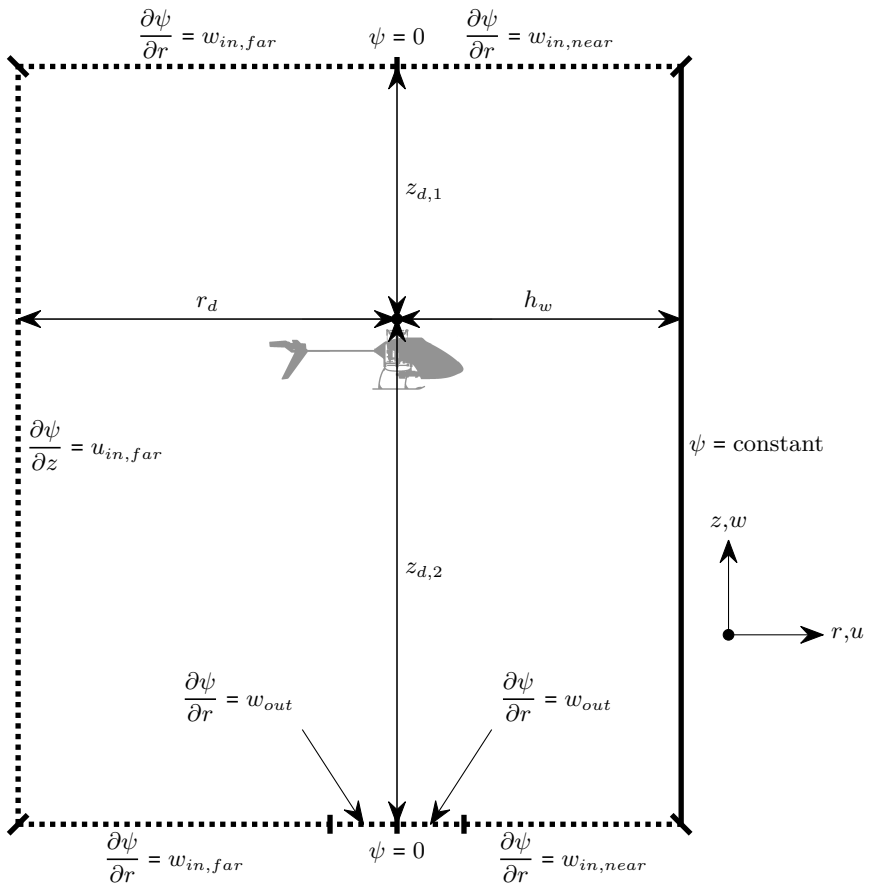

FIGURE 7.28: Schematic showing the boundary conditions used for the near-wall potential flow model, where $z_{d,1}$, $z_{d,2}$, r_d, ψ, r, z, h_w, u and w are domain height above rotor, domain height below rotor, domain radius, stream function, radial distance, vertical distance, rotor-wall gap, radial velocity and vertical velocity respectively.

Given that, for potential flow, velocity can be related to a stream function, ψ, using Equation (6.8), Neumann boundary conditions (Cheng and Cheng, 2005) can be prescribed at the far boundaries using Equations (7.5), (7.6) and (7.7). Note that ψ is defined as zero at the centre of the far boundaries, as shown in Figure 7.28. Finally, a Dirichlet boundary condition (Cheng and Cheng, 2005) is prescribed at the wall, i.e., ψ = constant. These boundary conditions are indicated on the schematic provided in Figure 7.28.

Unlike for the near-ceiling potential flow model described in Section 6.2.3, Laplace's Equation (6.9) cannot be readily solved analytically for the near-wall potential flow model due to the piece-wise nature of the far-field boundary condi-

tions. Instead, for this analysis, Laplace's Equation (6.9) is solved numerically across a discretised domain using finite differencing (White, 2003)

$$\psi_{i,j} \approx \frac{\psi_{i-1,j} + \psi_{i+1,j} + \beta\left(\psi_{i,j-1} + \psi_{i,j+1}\right)}{2\left(1+\beta\right)}, \tag{7.8}$$

where i and j are discrete node numbers in the radial and vertical direction respectively and

$$\beta = \left(\frac{\Delta r}{\Delta z}\right)^2, \tag{7.9}$$

where Δr and Δz are radial and vertical step size between discrete nodes. Equation (7.8) is applied by sweeping across all nodes in the domain and iterating until the solution converges. In this analysis, the domain dimensions, r_d, $z_{d,1}$ and $z_{d,2}$ are set equal to $5R$ and the domain is discretised using a square grid with $\Delta r = \Delta z = 0.05R$.

The stream function has been solved for across the discretised domain at non-dimensionalised rotor-wall gaps of h_w/R = 3.00, 2.50, 2.00, 1.75 and 1.50. Streamlines through the domain have been obtained by interpolating the domain at constant ψ. The resulting streamlines for each rotor-wall gap (and the baseline result) are plotted in Figure 7.29. For the baseline case, the streamlines are symmetric on either side of the domain and convect inward radially downstream of the rotor. As the rotor-wall gap decreases, the streamlines at the near-wall side of the rotor move closer to parallel with the wall. At the far-wall side of the rotor, the radial contraction of the streamlines increases as rotor-wall gap decreases. This is qualitatively consistent with the CFD and 2D FV flow field results previously shown in Figures 7.8, 7.9, 7.10 and 7.11. The mechanism that drives this fluid interaction becomes clear when the boundary conditions illustrated in Figure 7.28 are examined. The near-wall boundaries prescribe an inward radial component of flow velocity that decreases in magnitude as rotor-wall gap decreases, i.e.,

$$\lim_{h_w \to 1} u_{in,near} = 0. \tag{7.10}$$

This forces the flow to have a predominantly vertical component of velocity at the near-wall side of the domain as rotor-wall gap decreases, i.e., fluid flows predominantly

parallel to the wall at the near-wall side of the rotor as rotor-wall gap decreases. In contrast, the boundary condition prescribed at the far-wall boundary remains constant as rotor-wall gap decreases. Therefore, radial contraction of the flow field will always occur at the far-wall side of the domain. In fact, this radial contraction at the far-wall side of the domain will increase with decreasing rotor-wall gap because the radial component of momentum at the near-wall side of the domain (opposing the radial contraction at the far-wall side) is decreasing. This demonstrates that the fluid interactions between the rotor and the wall are primarily driven by the wall plane reducing the component of flow momentum in the direction normal to the wall plane.

As previously highlighted in Figure 7.27, the forces acting at the rotor are directly related to vortex structures in the rotor wake and the induced velocity field through the rotor. The induced velocity can be related to the potential flow model using Equation (6.8). Note that the velocities obtained using this equation are indicative only as the potential flow model does not explicitly model the rotor within the fluid domain. The potential flow model has been used to compute the radial and vertical components of velocity at $r = \pm R$ and $z = 0$. These velocities have been non-dimensionalised by the baseline velocity and plotted against non-dimensionalised rotor-wall gap in Figure 7.30. For the radial component of velocity, the potential flow model predicts a significant increase relative to the baseline result at the far-wall side of the rotor (i.e., at $r = -R$). In contrast, the potential flow model predicts a reverse in the direction of the radial component of velocity at the near-wall side of the rotor (i.e., at $r = R$). In addition to this, the potential flow model predicts that the vertical component of velocity at the near-wall side of the rotor will be larger than at the far-wall side of the rotor. The deficit in the vertical component of velocity across the rotor increases in magnitude as rotor-wall gap decreases. Here, the vertical component of velocity is analogous to the induced velocity previously discussed in Section 7.1.4. This result demonstrates that the changes in induced velocity that the drive the thrust deficit across the rotor are directly cause by fluid interactions between the rotor and the wall across the vertical plane that is normal to the wall (i.e., the x-z plane).

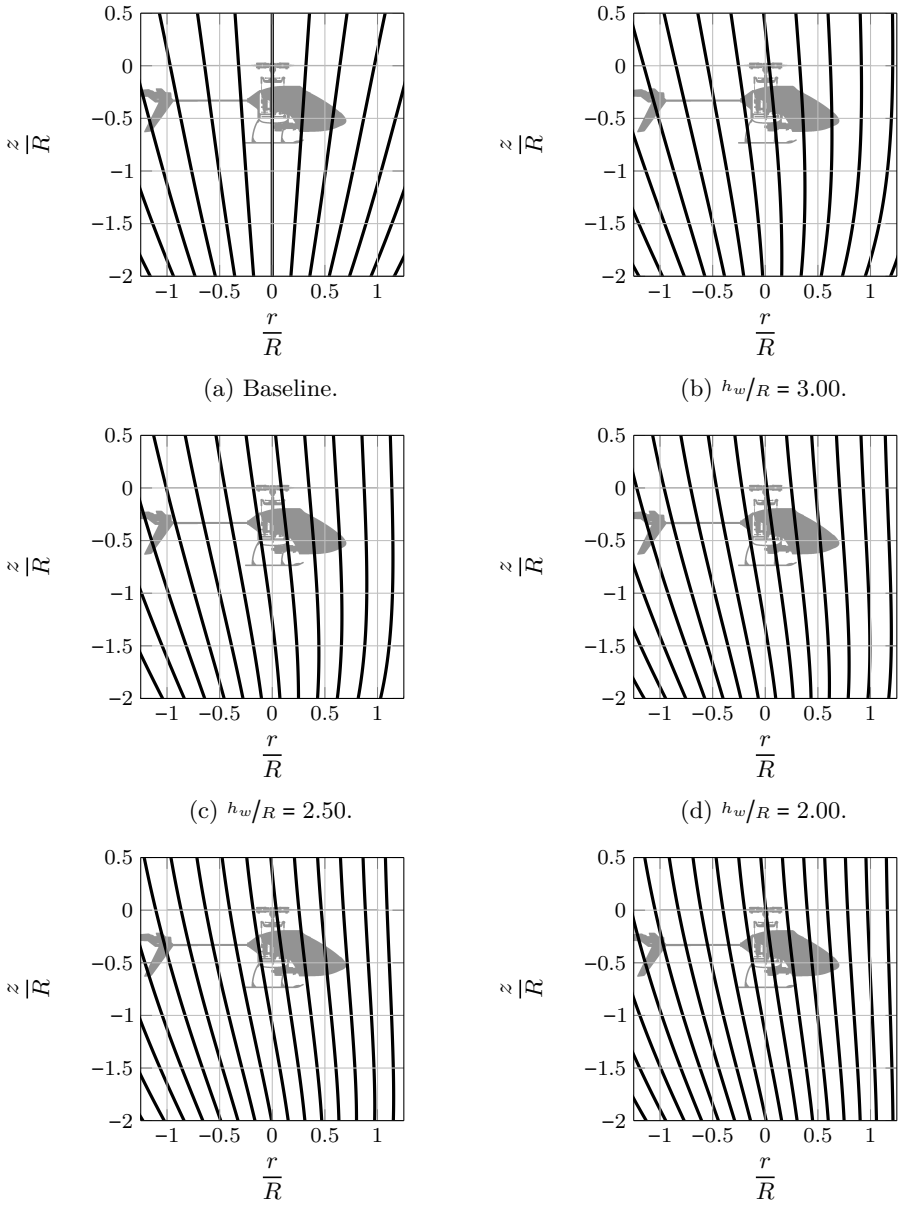

(a) Baseline.

(b) h_w/R = 3.00.

(c) h_w/R = 2.50.

(d) h_w/R = 2.00.

(e) h_w/R = 1.75.

(f) h_w/R = 1.50.

Figure 7.29: Streamlines showing two dimensional flow through a micro rotor in close proximity to a wall. Streamlines have been obtained using the finite differencing stream function method.

7.2.4 Comparison with Near-Ground and Near-Ceiling Fluid Interactions

Several parallels can be drawn between hovering micro rotor fluid interactions with a wall plane and fluid interactions with a ground or ceiling plane. In each of these

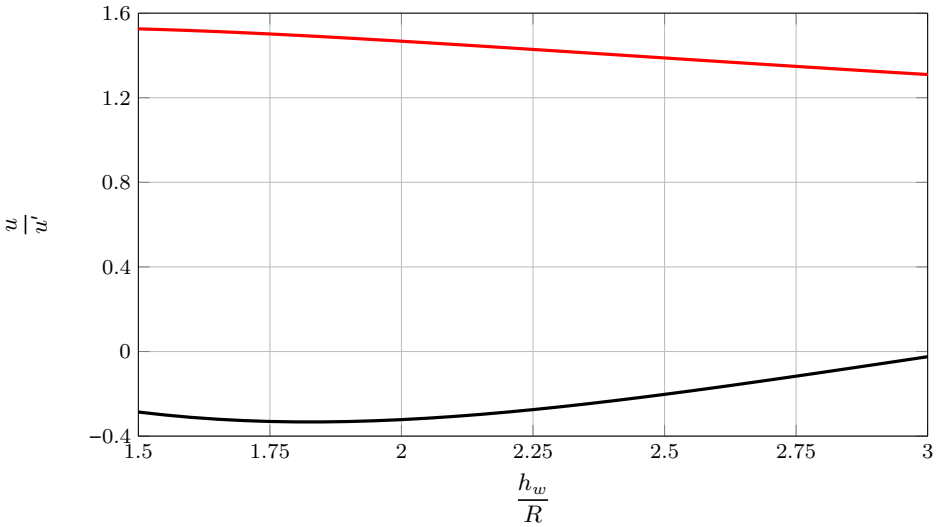

(a) Plot of non-dimensionalised radial component of velocity vs non-dimensionalised rotor-wall gap.

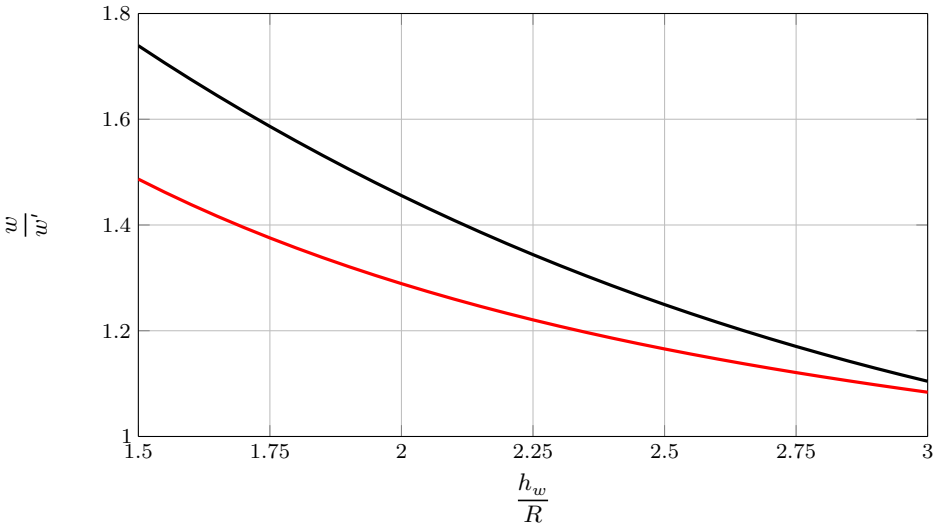

(b) Plot of non-dimensionalised vertical component of velocity vs non-dimensionalised rotor-wall gap.

$r = R$, i.e., $\phi_w = 0^\circ$ ——— $r = -R$, i.e., $\phi_w = 180^\circ$ ———

FIGURE 7.30: Effect of fluid interactions with the wall plane on radial and vertical components of velocity through the rotor disk. Results shown here have been computed using the near-wall potential flow model.

cases, the planar surface forces a decrease the in the component of fluid momentum in the direction normal to the planar surface. This effect becomes more prominent as proximity to the surface decreases; within the boundary layer of the planar surface, the component of fluid momentum normal to the surface will be close to zero. Because of this fluid interaction, the structure of the flow field through a micro

rotor will alter when in close proximity to a planar surface. For the near-ground and near-ceiling cases, the vertical component of velocity through the rotor decreases due to proximity to the planar surface. For the near-wall case, the radial component of flow velocity at the near-wall side of the flow field decreases. Where these fluid interactions occur, the component of momentum parallel to the surface must increase in order for momentum to be conserved. For the near-ground and near-ceiling cases, this causes an increase and a decrease in radial wake expansion respectively. For the near-wall case, this causes the induced velocity to increase through the near-wall side of the rotor. In all cases, changes in the induced velocity alter the effective angle of attack of the rotor. This, in turn, drives changes in the loading at the blade surface.

7.3 Summary

The results presented in this section show that the presence of a vertical wall plane in close proximity to a micro rotor will reduce the component of fluid momentum in the direction normal to the wall on the near-wall side of the rotor. For momentum to be conserved, induced velocity must therefore accelerate near the blade tip. On the far-wall side of the rotor, the rate of radial contraction of the wake increases as rotor-wall gap decreases due to the fact that there is a decreasing component of radial momentum on the near-wall side to oppose the wake on the far wall side. This increasing radial component of fluid velocity at the far-wall side of the wake causes a decrease in induced velocity. These induced velocity effects cause local effective angle of attack to increase at the far-wall side of the rotor and decrease near the blade tip at the near-wall side of the rotor. These changes in local effective angle of attack drive a significant increase in y-axis torque ratio as rotor-wall gap decreases.

A y-axis torque that is induced by proximity to a wall plane is likely to have a significant adverse effect on helicopter stability. The torque will rotate the helicopter rotor resulting in a horizontal component of rotor thrust accelerating the helicopter toward the wall. If this is not compensated for, the helicopter will collide with the wall plane. As a first step toward implementing micro helicopter control and collision avoidance schemes for near-wall operations, a scheme for estimating the

disturbances that are induced by wall proximity is postulated in Chapter 8.

Chapter 8

In-Flight Estimation of Aerodynamic Disturbances Induced by Micro Rotor Fluid Interactions with Planar Surfaces

As shown in Chapters 5, 6 and 7, a hovering micro rotor in close proximity to a planar surface will experience exogenous disturbances due to aerodynamic proximity effects. For a hovering micro helicopter in close proximity to a ground or ceiling plane, a vertical force disturbance will be experienced. For a hovering micro rotor in close proximity to a wall plane, a torque about the horizontal axis parallel to the wall will be experienced (i.e., a torque about the y-axis defined in Figure 7.5). These exogenous disturbances have been shown to increase in magnitude as proximity to the planar surface decreases, according to the relationships defined by Equations (A.1), (6.7) and (7.4). In order to robustly compensate for these disturbances, it is necessary to estimate them during flight. Furthermore, given that the relationship between proximity and disturbance magnitude is known *a priori*, it is possible to use the disturbance estimate to passively estimate proximity. Passive proximity estimation is

a key contribution of this research as it demonstrates that it is feasible to implement navigation and collision avoidance systems using measurements provided by on-board inertial sensors only - mitigating the need for micro helicopters to accommodate additional exteroceptive proximity sensors. This will, in turn, free-up power and payload capacity that are already limited at a micro scale.

To obtain accurate estimates of aerodynamic disturbances induced by proximity effects, a novel simultaneous state and disturbance estimator is postulated in this chapter. The estimator is designed to handle direct feed-through of exogenous force disturbances to accelerometer measurements (previously discussed in Section 2.3.3). A derivation of the estimator is outlined in Section 8.1 and the estimator is applied to the micro helicopter test-bed in Section 8.2. Finally, the performance of the estimator, as well as the passive proximity estimation scheme, is evaluated using experimental flight tests in Section 8.3.

8.1 Simultaneous State and Disturbance Estimator

As previously discussed in Section 2.3, disturbance estimators from the existing literature that have been applied to MAVs typically rely on having access to all of the system states (typically obtained using an external motion capture system or GPS). For operation within a confined environment, such systems are not likely to be feasible. Under these conditions, a MAV will have to rely on on-board inertial sensors and, as such, will not have direct access to the complete state vector. Therefore, in order to estimate exogenous disturbances acting on a micro helicopter in confined environments, it is necessary to simultaneously estimate the states, i.e., simultaneous state and disturbance estimation. In addition to this, exogenous force disturbances will feed-through directly to MEMS accelerometer measurements. As discussed in Section 2.3.3, direct feed-through of exogenous disturbances to measured outputs is not addressed by simultaneous state and disturbance estimators in the existing literature. To address this, a novel linear simultaneous state and disturbance estimator for systems with direct feed-through of known inputs and/or unknown exogenous disturbances is postulated in this section.

8.1.1 Estimator Derivation

The estimator relies on having *a priori* knowledge of the system's dynamics in the form described by Equation (2.22). The goal of the simultaneous state and disturbance estimation problem is to accurately estimate $\boldsymbol{x}$ and $\boldsymbol{d}$ based on the known system dynamics and $\boldsymbol{u}$ and $\boldsymbol{y}$. Given a system in the form described by Equation (2.22) the unknown states, $\boldsymbol{x}$, can be estimated from (Luenberger, 1966)

$$\dot{\hat{\boldsymbol{x}}} = \boldsymbol{A}\hat{\boldsymbol{x}} + \boldsymbol{B}_{\boldsymbol{u}}\boldsymbol{u} + \boldsymbol{B}_{\boldsymbol{d}}\boldsymbol{d} + \boldsymbol{L}_{\boldsymbol{x}}\left(\boldsymbol{y} - \boldsymbol{C}\hat{\boldsymbol{x}} - \boldsymbol{D}_{\boldsymbol{u}}\boldsymbol{u} - \boldsymbol{D}_{\boldsymbol{d}}\boldsymbol{d}\right), \tag{8.1}$$

where $\boldsymbol{L}_{\boldsymbol{x}} \in \mathbb{R}^{n\times p}$ is the state estimator gain and the notation ˆ denotes the estimated value of a vector.

The unknown disturbances, $\boldsymbol{d}$, can be estimated by introducing an additional state vector, $\boldsymbol{z} \in \mathbb{R}^{q}$ (Li et al., 2014)

$$\begin{aligned} \dot{\boldsymbol{z}} &= -\boldsymbol{L}_{\boldsymbol{d}}\left(\boldsymbol{A}\boldsymbol{x} + \boldsymbol{B}_{\boldsymbol{u}}\boldsymbol{u} + \boldsymbol{B}_{\boldsymbol{d}}\hat{\boldsymbol{d}}\right), \\ \hat{\boldsymbol{d}} &= \boldsymbol{z} + \boldsymbol{L}_{\boldsymbol{d}}\boldsymbol{x}, \end{aligned} \tag{8.2}$$

where $\boldsymbol{L}_{\boldsymbol{d}} \in \mathbb{R}^{q\times n}$ is the disturbance estimator gain.

For the simultaneous state and disturbance estimation problem, both $\boldsymbol{x}$ and $\boldsymbol{d}$ are unknown. As such, neither Equations (8.1) nor (8.2) can be realised. To address this, a simultaneous state and disturbance estimator, based on a hybrid of Equations (8.1) and (8.2), is proposed

$$\begin{aligned} \dot{\hat{\boldsymbol{x}}} &= \boldsymbol{A}\hat{\boldsymbol{x}} + \boldsymbol{B}_{\boldsymbol{u}}\boldsymbol{u} + \boldsymbol{B}_{\boldsymbol{d}}\hat{\boldsymbol{d}} + \boldsymbol{L}_{\boldsymbol{x}}\left(\boldsymbol{y} - \boldsymbol{C}\hat{x} - \boldsymbol{D}_{\boldsymbol{u}}\boldsymbol{u} - \boldsymbol{D}_{\boldsymbol{d}}\hat{\boldsymbol{d}}\right), \\ \dot{\boldsymbol{z}} &= -\boldsymbol{L}_{\boldsymbol{d}}\left(\boldsymbol{A}\hat{\boldsymbol{x}} + \boldsymbol{B}_{\boldsymbol{u}}\boldsymbol{u} + \boldsymbol{B}_{\boldsymbol{d}}\hat{\boldsymbol{d}}\right), \\ \hat{\boldsymbol{d}} &= \boldsymbol{z} + \boldsymbol{L}_{\boldsymbol{d}}\hat{\boldsymbol{x}}. \end{aligned} \tag{8.3}$$

Note that, because this estimator does not assume that $\boldsymbol{D}_{\boldsymbol{u}}$ and $\boldsymbol{D}_{\boldsymbol{d}}$ are zero, it is particularly useful for cases where direct feed-through of inputs and disturbances to sensor measurements cannot be ignored. The estimator can be expressed in state space form as

$$\begin{bmatrix} \dot{\hat{\boldsymbol{x}}} \\ \dot{\boldsymbol{z}} \end{bmatrix} = \begin{bmatrix} \boldsymbol{A} + \boldsymbol{B}_d\boldsymbol{L}_d - \boldsymbol{L}_x\boldsymbol{C} - \boldsymbol{L}_x\boldsymbol{D}_d\boldsymbol{L}_d & \boldsymbol{B}_d - \boldsymbol{L}_x\boldsymbol{D}_d \\ -\boldsymbol{L}_d\boldsymbol{A} - \boldsymbol{L}_d\boldsymbol{B}_d\boldsymbol{L}_d & -\boldsymbol{L}_d\boldsymbol{B}_d \end{bmatrix} \begin{bmatrix} \hat{\boldsymbol{x}} \\ \boldsymbol{z} \end{bmatrix}$$

$$+ \begin{bmatrix} \boldsymbol{B}_u - \boldsymbol{L}_x\boldsymbol{D}_u & \boldsymbol{L}_x \\ -\boldsymbol{L}_d\boldsymbol{B}_u & \boldsymbol{0}_{q\times p} \end{bmatrix} \begin{bmatrix} \boldsymbol{u} \\ \boldsymbol{y} \end{bmatrix}, \tag{8.4}$$

$$\begin{bmatrix} \hat{\boldsymbol{x}} \\ \hat{\boldsymbol{d}} \end{bmatrix} = \begin{bmatrix} \boldsymbol{I}_{n\times n} & \boldsymbol{0}_{n\times q} \\ \boldsymbol{L}_d & \boldsymbol{I}_{q\times q} \end{bmatrix} \begin{bmatrix} \hat{\boldsymbol{x}} \\ \boldsymbol{z} \end{bmatrix} + \begin{bmatrix} \boldsymbol{0}_{(n+q)\times(m+p)} \end{bmatrix} \begin{bmatrix} \boldsymbol{u} \\ \boldsymbol{y} \end{bmatrix}.$$

8.1.2 Estimator Error Dynamics

The estimator error dynamics are governed by

$$\begin{bmatrix} \dot{\boldsymbol{e}}_x \\ \dot{\boldsymbol{e}}_d \end{bmatrix} = \overline{\boldsymbol{A}} \begin{bmatrix} \boldsymbol{e}_x \\ \boldsymbol{e}_d \end{bmatrix} + \begin{bmatrix} \boldsymbol{0}_{n\times q} \\ -\boldsymbol{I}_{q\times q} \end{bmatrix} \begin{bmatrix} \dot{\boldsymbol{d}} \end{bmatrix}, \tag{8.5}$$

where

$$\begin{bmatrix} \boldsymbol{e}_x \\ \boldsymbol{e}_d \end{bmatrix} = \begin{bmatrix} \hat{\boldsymbol{x}} \\ \hat{\boldsymbol{d}} \end{bmatrix} - \begin{bmatrix} \boldsymbol{x} \\ \boldsymbol{d} \end{bmatrix}, \tag{8.6}$$

and

$$\overline{\boldsymbol{A}} = \begin{bmatrix} \boldsymbol{A} - \boldsymbol{L}_x\boldsymbol{C} & \boldsymbol{B}_d - \boldsymbol{L}_x\boldsymbol{D}_d \\ -\boldsymbol{L}_d\boldsymbol{L}_x\boldsymbol{C} & -\boldsymbol{L}_d\boldsymbol{L}_x\boldsymbol{D}_d \end{bmatrix}. \tag{8.7}$$

The estimator error dynamics will be bounded-input bounded-output (BIBO) stable if $\overline{\boldsymbol{A}}$ is Hurwitz. Additionally, the estimator error dynamics will be asymptotically stable if $\overline{\boldsymbol{A}}$ is Hurwitz and the disturbance, $\boldsymbol{d}$, tends to a constant value.

8.1.3 Observability

The estimator error dynamics, $\overline{\boldsymbol{A}}$, can be rewritten as

$$\overline{\boldsymbol{A}} = \begin{bmatrix} \boldsymbol{A} & \boldsymbol{B}_d \\ \boldsymbol{0}_{q\times n} & \boldsymbol{0}_{q\times q} \end{bmatrix} - \boldsymbol{L} \begin{bmatrix} \boldsymbol{C} & \boldsymbol{D}_d \end{bmatrix}, \tag{8.8}$$

where

$$\boldsymbol{L} = \begin{bmatrix} \boldsymbol{L_1} \\ \boldsymbol{L_2} \end{bmatrix} \equiv \begin{bmatrix} \boldsymbol{L_x} \\ \boldsymbol{L_d L_x} \end{bmatrix}, \tag{8.9}$$

where $\boldsymbol{L_1} \in \mathbb{R}^{n \times p}$ and $\boldsymbol{L_2} \in \mathbb{R}^{q \times p}$. From Equation (8.8) it follows that $\boldsymbol{x}$ and $\boldsymbol{d}$ will be observable if the pair

$$\left(\begin{bmatrix} \boldsymbol{A} & \boldsymbol{B_d} \\ \boldsymbol{0}_{q \times n} & \boldsymbol{0}_{q \times q} \end{bmatrix}, \begin{bmatrix} \boldsymbol{C} & \boldsymbol{D_d} \end{bmatrix} \right), \tag{8.10}$$

is observable. Note that the gain, $\boldsymbol{L}$, can be designed using direct pole placement and $\boldsymbol{L_x}$ and $\boldsymbol{L_d}$ can be computed from

$$\begin{aligned} \boldsymbol{L_x} &= \boldsymbol{L_1}, \\ \boldsymbol{L_d} &= \boldsymbol{L_2 L_1}^T \left(\boldsymbol{L_1 L_1}^T \right)^{-1}. \end{aligned} \tag{8.11}$$

8.1.4 H_∞ Synthesis

In this research, H_∞ synthesis has been selected to obtain the gain values $\boldsymbol{L_x}$ and $\boldsymbol{L_d}$. H_∞ synthesis is particularly well suited to helicopter dynamics because of its applicability to multi-input multi-output (MIMO) systems with dynamic coupling between states (Skogestad and Postlethwaite, 2001). To use H_∞ synthesis, the dependency of the error vector, $[\boldsymbol{e_x}^T \ \boldsymbol{e_d}^T]^T$, on the rate of change of the exogenous disturbance, $\dot{\boldsymbol{d}}$, is expressed in state space form as

$$\begin{aligned} \begin{bmatrix} \dot{\boldsymbol{e_x}} \\ \dot{\boldsymbol{e_d}} \end{bmatrix} &= \overline{\boldsymbol{A}} \begin{bmatrix} \boldsymbol{e_x} \\ \boldsymbol{e_d} \end{bmatrix} + \begin{bmatrix} \boldsymbol{0}_{n \times q} \\ -\boldsymbol{I}_{q \times q} \end{bmatrix} \begin{bmatrix} \dot{\boldsymbol{d}} \end{bmatrix}, \\ \begin{bmatrix} \boldsymbol{e_x} \\ \boldsymbol{e_d} \end{bmatrix} &= \begin{bmatrix} \boldsymbol{I}_{(n+q) \times (n+q)} \end{bmatrix} \begin{bmatrix} \boldsymbol{e_x} \\ \boldsymbol{e_d} \end{bmatrix} + \begin{bmatrix} \boldsymbol{0}_{(n+q) \times q} \end{bmatrix} \begin{bmatrix} \dot{\boldsymbol{d}} \end{bmatrix}. \end{aligned} \tag{8.12}$$

To obtain $\boldsymbol{L_x}$ and $\boldsymbol{L_d}$ using H_∞ synthesis, the H_∞ norm ($\|H\|_\infty$) of the closed loop system described by Equation (8.12) has been minimised using the non-smooth optimisation method of Apkarian and Noll (2006), where the H_∞ norm has been

calculated using the algorithm of Bruisma and Steinbuch (1990). In principle, this estimator synthesis process minimises the effect that exogenous disturbances have on state and disturbance estimate errors.

8.2 Application of Estimator to Micro Helicopter Test-Bed Hovering Dynamics

Note that the closed loop helicopter hovering dynamics identified in Section 3.3 fail to meet the observability criteria described in Section 8.1.3, i.e.,

$$\operatorname{rank}\left(\operatorname{obsv}\left(\begin{bmatrix} \boldsymbol{A} & \boldsymbol{B_d} \\ \mathbf{0}_{q\times n} & \mathbf{0}_{q\times q} \end{bmatrix}, \begin{bmatrix} \boldsymbol{C} & \boldsymbol{D_d} \end{bmatrix}\right)\right) \neq n + q, \tag{8.13}$$

where the functions $\operatorname{rank}(\cdot)$ and $\operatorname{obsv}(\cdot,\cdot)$ determine the rank of a matrix and the observability matrix for a pair of matrices respectively. Because the complete dynamics are not observable, it is not possible to implement a single simultaneous state and disturbance estimator for the full helicopter hovering dynamics. Instead, in this section, it is assumed that helicopter heave-yaw hovering dynamics are only weakly coupled with lateral-longitudinal hovering dynamics. This dynamic coupling is governed by the stability derivatives Z_a and Z_b and can, therefore, be neglected if the rotor flapping angles are very near to zero. This assumption is valid for the helicopter hovering state. Once decoupled, separate estimators can be implemented for both the heave-yaw and lateral-longitudinal dynamics, as outlined in Sections 8.2.1 and 8.2.2 respectively.

8.2.1 Heave-Yaw Estimator

The micro helicopter test-bed's closed loop heave-yaw hovering dynamics can be expressed in the generalised state space form described by Equation (2.22) as

$$\dot{\boldsymbol{x}} = \begin{bmatrix} Z_w & Z_r \\ N_w & N_r - K_{p,yaw}N_{yaw} \end{bmatrix}\boldsymbol{x} + \begin{bmatrix} 0 & Z_{col} \\ K_{P,yaw}N_{yaw} & N_{col} \end{bmatrix}\boldsymbol{u} + \begin{bmatrix} \frac{1}{m} \\ 0 \end{bmatrix}\boldsymbol{d},$$
$$\boldsymbol{y} = \begin{bmatrix} Z_w & Z_r \\ 0 & 1 \end{bmatrix}\boldsymbol{x} + \begin{bmatrix} 0 & Z_{col} \\ 0 & 0 \end{bmatrix}\boldsymbol{u} + \begin{bmatrix} \frac{1}{m} \\ 0 \end{bmatrix}\boldsymbol{d}, \tag{8.14}$$

where

$$\boldsymbol{x} = \begin{bmatrix} w \\ r \end{bmatrix}, \qquad \boldsymbol{u} = \begin{bmatrix} \delta_{yaw} \\ \delta_{col} \end{bmatrix}, \qquad \boldsymbol{d} = \begin{bmatrix} \overline{Z} \end{bmatrix}, \qquad \boldsymbol{y} = \begin{bmatrix} \dot{w} \\ r \end{bmatrix}. \tag{8.15}$$

Note that force in the z direction is the only exogenous disturbance considered by the heave-yaw dynamics model. Furthermore, the output vector, $\boldsymbol{y}$, contains both the heave acceleration and yaw-rate, as both of these states can be readily measured by on-board MEMS accelerometers and gyroscopes. Note also that the model described by Equation (8.14) meets the observability criteria specified in Section 8.1.3.

Using this model structure and the model parameters identified for the micro helicopter test-bed in Section 3.3, the following estimator gains are obtained using the H_∞ synthesis technique described in Section 8.1.4

$$\boldsymbol{L_x} = \begin{bmatrix} -11.5683 & 30.4180 \\ 63.9445 & 152.4868 \end{bmatrix}, \qquad \boldsymbol{L_d} = \begin{bmatrix} -4.3873 & 0.0345 \end{bmatrix}. \tag{8.16}$$

These estimator gains are used to estimate aerodynamic disturbances induced by ground and ceiling proximity effects in Section 8.3.1 and 8.3.2 respectively.

8.2.2 Lateral-Longitudinal Estimator

The micro helicopter test-bed's closed loop lateral-longitudinal hovering dynamics can be expressed in the generalised state space form described by Equation (2.22) as

$$
\dot{\boldsymbol{x}} = \begin{bmatrix}
X_u & 0 & 0 & 0 & 0 & -g & X_a & 0 \\
0 & Y_v & 0 & 0 & g & 0 & 0 & Y_b \\
L_u & L_v & 0 & 0 & 0 & 0 & 0 & L_b \\
M_u & M_v & 0 & 0 & 0 & 0 & M_a & 0 \\
0 & 0 & 1 & 0 & 0 & 0 & 0 & 0 \\
0 & 0 & 0 & 1 & 0 & 0 & 0 & 0 \\
0 & 0 & 0 & -1 & \frac{K_{P,\phi}A_{lat}}{\tau_f} & \frac{K_{P,\theta}A_{lon}}{\tau_f} & \frac{-1}{\tau_f} & \frac{A_b}{\tau_f} \\
0 & 0 & -1 & 0 & \frac{K_{P,\phi}B_{lat}}{\tau_f} & \frac{K_{P,\theta}A_{lon}}{\tau_f} & \frac{B_a}{\tau_f} & \frac{-1}{\tau_f}
\end{bmatrix} \boldsymbol{x}
$$

$$
+ \begin{bmatrix}
0 & 0 \\
0 & 0 \\
0 & 0 \\
0 & 0 \\
0 & 0 \\
0 & 0 \\
\frac{K_{P,u_{lat}}A_{lat}}{\tau_f} & \frac{K_{P,u_{lon}}A_{lon}}{\tau_f} \\
\frac{K_{P,u_{lat}}B_{lat}}{\tau_f} & \frac{K_{P,u_{lon}}B_{lon}}{\tau_f}
\end{bmatrix} \boldsymbol{u} + \begin{bmatrix}
0 & 0 \\
0 & 0 \\
\frac{1}{J_{xx}} & 0 \\
0 & \frac{1}{J_{yy}} \\
0 & 0 \\
0 & 0 \\
0 & 0 \\
0 & 0
\end{bmatrix} \boldsymbol{d}, \tag{8.17}
$$

$$
\boldsymbol{y} = \begin{bmatrix}
X_u & 0 & 0 & 0 & 0 & -g & X_a & 0 \\
0 & Y_v & 0 & 0 & g & 0 & 0 & Y_b \\
0 & 0 & 1 & 0 & 0 & 0 & 0 & 0 \\
0 & 0 & 0 & 1 & 0 & 0 & 0 & 0 \\
0 & 0 & 0 & 0 & 1 & 0 & 0 & 0 \\
0 & 0 & 0 & 0 & 0 & 1 & 0 & 0
\end{bmatrix} \boldsymbol{x} + \begin{bmatrix} 0_{p\times m} \end{bmatrix} \boldsymbol{u} + \begin{bmatrix} 0_{p\times q} \end{bmatrix} \boldsymbol{d},
$$

where the moment of inertia terms, J_{xx} and J_{yy}, are $1.14 \cdot 10^{-4}$ kgm^2 and $1.42 \cdot 10^{-4}$ kgm^2 respectively and

$$\boldsymbol{x} = \begin{bmatrix} u \\ v \\ p \\ q \\ \phi \\ \theta \\ a \\ b \end{bmatrix}, \qquad \boldsymbol{u} = \begin{bmatrix} \delta_{lat} \\ \delta_{lon} \end{bmatrix}, \qquad \boldsymbol{d} = \begin{bmatrix} \overline{L} \\ \overline{M} \end{bmatrix}, \qquad \boldsymbol{y} = \begin{bmatrix} \dot{u} \\ \dot{v} \\ p \\ q \\ \phi \\ \theta \end{bmatrix}. \tag{8.18}$$

Note that torques about the x-axis and y-axis are the only exogenous disturbances considered by the lateral-longitudinal dynamics model. The output vector, $\boldsymbol{y}$, contains the x-axis and y-axis accelerations and angular velocities, as these states can be readily measured by on-board MEMS accelerometers and gyroscopes. In addition to this, pitch and roll rotation angles are included in the output vector as these are estimated on-board the micro helicopter test-bed using the attitude filter outlined in Section 3.2.2.1. Note also that the model described by Equation (8.17) meets the observability criteria specified in Section 8.1.3.

Using this model structure and the model parameters identified for the micro helicopter test-bed in Section 3.3, the following estimator gains are obtained using the H_∞ synthesis technique described in Section 8.1.4

$$\boldsymbol{L_x} = \begin{bmatrix} 0.9974 & -0.0005 & 0 & 0.0001 & -0.0039 & -0.0094 \\ -0.0001 & 0.9976 & -0.0002 & 0.0001 & 0.0077 & 0.0048 \\ -0.1216 & 27.2947 & 0.8784 & 0.0099 & -266.4193 & -1.2505 \\ -30.9645 & 0.2997 & 0.0104 & 0.5634 & -2.8775 & -305.5636 \\ -0.0052 & 0.0003 & 0.9993 & -0.0007 & 0.4776 & 0.0050 \\ -0.0048 & -0.0046 & 0.0012 & 1.0008 & 0.0030 & 0.9387 \\ 1.2335 & -0.0463 & -0.0017 & -0.9983 & -0.8198 & 8.7874 \\ 0.4829 & -1.2213 & -0.9941 & -0.0028 & 7.7471 & 5.7351 \end{bmatrix}, \tag{8.19}$$

$$\boldsymbol{L_d} = \begin{bmatrix} -0.0049 & 0.0016 & 0.0003 & 0.0001 & \cdots & 0.0032 & -0.0056 & -0.0056 & 0.0030 \\ 0.0016 & -0.0046 & 0 & 0.0001 & \cdots & -0.0047 & 0.0016 & 0.0016 & -0.0046 \end{bmatrix}^T.$$

These estimator gains are used to estimate aerodynamic disturbances induced by wall proximity effects in Section 8.3.3.

8.3 Flight Test Results

In this section, the simultaneous state and disturbance estimator's ability to accurately estimate aerodynamic disturbances is evaluated using experimental flight tests. Three separate flight tests have been performed:

1. Hovering near to a ground plane (outlined in Section 8.3.1).
2. Hovering near to a ceiling plane (outlined in Section 8.3.2).
3. Hovering near to a wall plane (outlined in Section 8.3.3).

For each flight test, flight data has been collected by manually piloting the micro helicopter test-bed. Aerodynamic disturbances induced by proximity to the ground, ceiling or wall plane are estimated at the ground station computer. Note that the heave-yaw estimator is used to estimate disturbances induced by ground and ceiling proximity and the lateral-longitudinal estimator is used to estimate disturbances

induced by wall proximity. For each of the three cases tested, the estimator's ability to estimate helicopter states and disturbances is evaluated. Additionally, the disturbance estimate is used to provide passive estimates of ground, ceiling and wall proximity.

Further discussion of the results presented in this section is provided in Section 8.4.

8.3.1 Near-Ground Flight Test Results

For the near-ground flight test, the decoupled heave-yaw dynamics described by Equation (8.14) and the heave-yaw estimator gains provided in Equation (8.16) have been used to estimate the heave velocity and yaw-rate states as well as the exogenous vertical force disturbance that is induced by proximity to the ground plane. The state and disturbance estimation performance, as well as the passive ground proximity estimate, are evaluated in this section.

Heave velocity and yaw-rate state estimates made across 8 s of near-ground flight data are plotted in Figure 8.1. Both estimated states show very good agreement with the actual data measured using the motion capture camera system. RMS and peak errors for the heave velocity estimate are 0.0142 m/s and 0.0347 m/s respectively. RMS and peak errors for the yaw-rate estimate are 0.0130 rad/s and 0.0465 rad/s respectively. This high accuracy is expected for the yaw-rate state estimate, as the yaw-rate has been directly measured using the z-axis gyroscope on-board the micro helicopter test-bed, i.e., the error present in the yaw-rate estimate is consistent with the expected error of the z-axis gyroscope. The high accuracy of the heave-velocity estimate is an interesting result, as velocity estimates made from acceleration measurements are typically subject to unbounded error due to the numerical integration of accelerometer biases[1]. However, in the case of a hovering micro helicopter, heave velocity is strongly coupled with yaw-rate via the stability derivatives Z_r and N_w. Because this dynamic coupling is known *a priori* from the system identification conducted in Section 3.3 and because yaw-rate can be measured directly on-board the micro helicopter test-bed, it is possible to obtain a heave velocity estimate with bounded error - as is shown in Figure 8.1(a).

[1]This process is commonly referred to as *dead reckoning*.

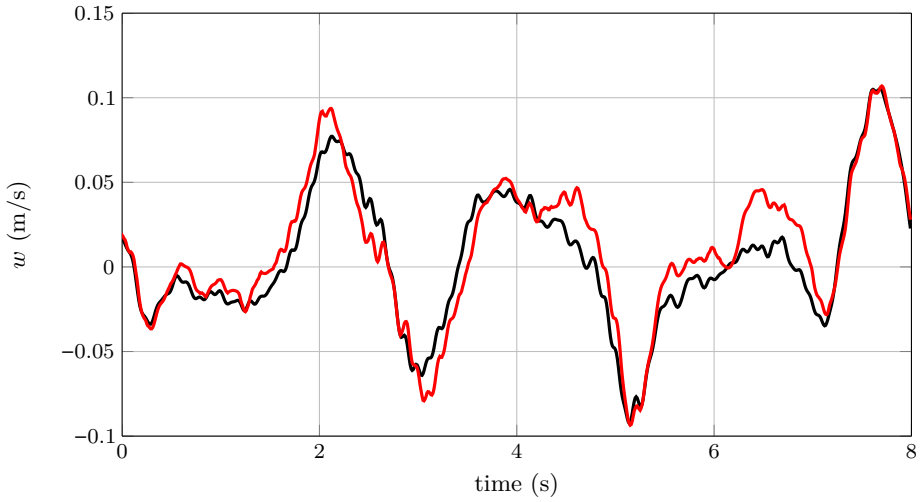

(a) Plot of heave velocity vs time.

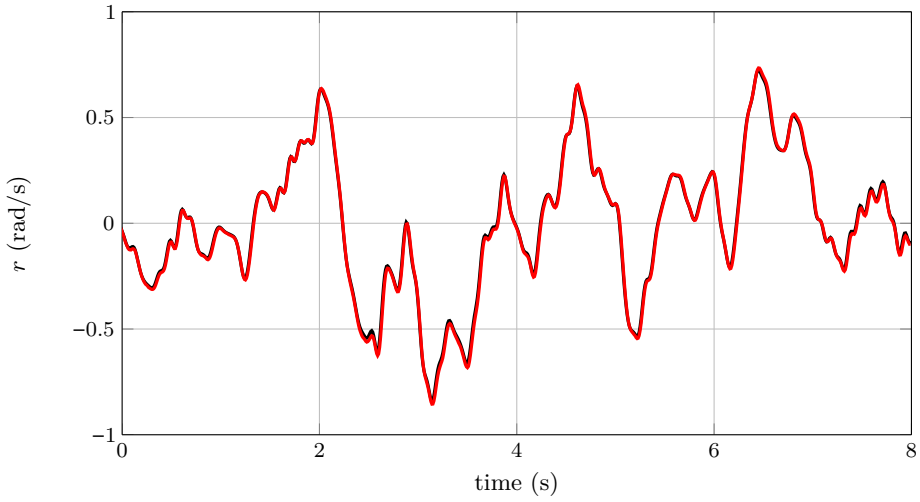

(b) Plot of yaw-rate vs time.

State measurement — State estimate

Figure 8.1: Comparison between actual and estimated heave/yaw states for a micro helicopter hovering in close proximity to a ground plane.

The estimate of the vertical force disturbance that is induced by aerodynamic ground proximity effects is plotted in Figure 8.2. Note that the actual vertical force disturbance that is experienced by the helicopter cannot be measured during flight. As such, it is not possible to directly validate the disturbance estimate result presented in this figure. Nonetheless, the accuracy of the disturbance estimate can be indirectly validated by using the disturbance estimate to obtain a passive estimate of ground proximity; the ground proximity estimate can then be directly compared

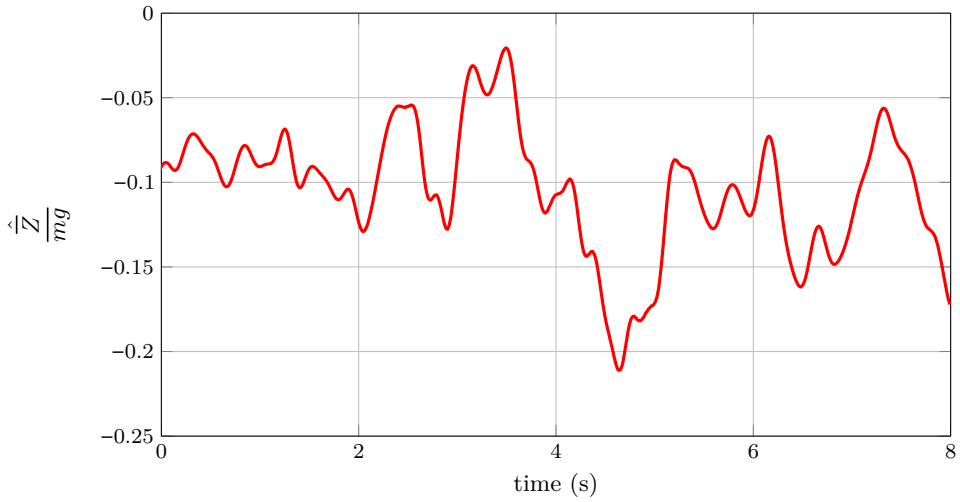

FIGURE 8.2: Plot of the estimate of the vertical force disturbance acting on a micro helicopter hovering in close proximity to a ground plane vs time.

with ground proximity measured using the motion capture camera system. Note also that further evaluation of the disturbance estimate accuracy is made by comparison with CFD results in Section 8.4.2.

If it is assumed that the results presented in Figure 8.2 provide a fair estimate of the vertical force disturbance induced by ground proximity, and the relationship between ground proximity and vertical force disturbance is known based on the CFD results (see Equation (A.1)), proximity to the ground can be passively estimated in-flight from

$$\hat{h}_g \approx \left(\frac{-0.0996mg}{\hat{\bar{Z}}} \right)^{(1/1.34)} . \tag{8.20}$$

Note, however, that Equation (8.20) will tend to infinity as the disturbance estimate tends to zero. This numerical instability may introduce large errors in the proximity estimate if the disturbance estimate is small. To account for this, an augmented proximity estimate can be made by adding a constant, α_g, to the denominator

$$\hat{h}_g \approx \left(\frac{-0.0996mg}{\hat{\bar{Z}} + \alpha_g} \right)^{(1/1.34)} . \tag{8.21}$$

A plot of the passive ground proximity estimate vs time is provided in Figure 8.3, where the augmented proximity estimate is made by setting $\alpha_g = -0.01$. Both passive

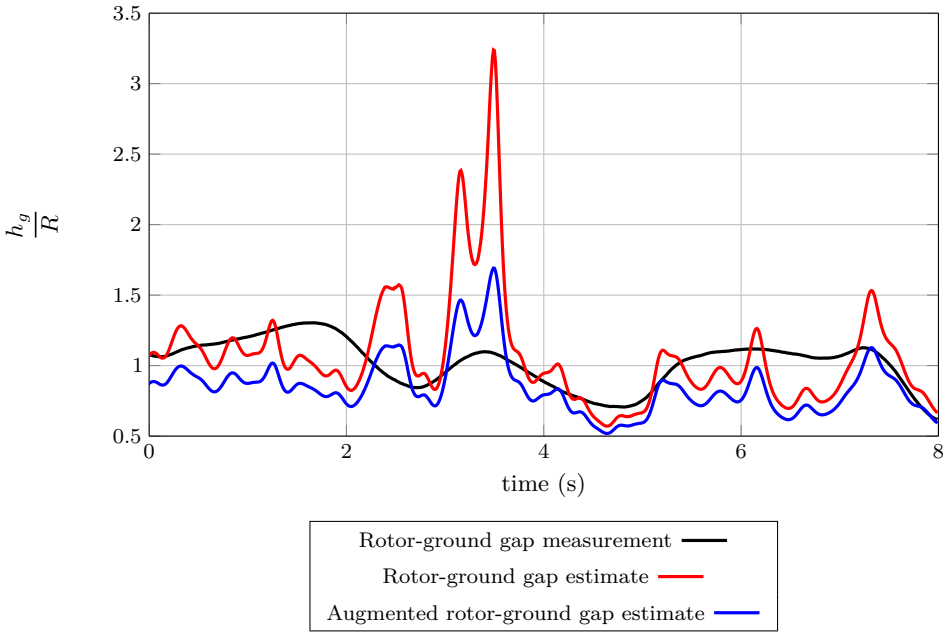

Figure 8.3: Comparison between actual and estimated ground proximity for a micro helicopter hovering in close proximity to a ground plane. Plot shows non-dimensionalised rotor-ground gap vs time.

ground proximity estimates show fair agreement with the proximity measurement obtained using the motion capture camera system. The proximity estimate made using Equation (8.20) has a RMS error and peak error of $0.3859R$ and $2.1498R$ respectively. As expected, the large peak error coincides with the disturbance estimate being near to zero at 3.53 s. In contrast, the augmented proximity estimate made using Equation (8.21) has a RMS error and peak error of $0.2725R$ and $0.6037R$ respectively. This 72% decrease in peak error clearly demonstrates that the augmented proximity estimate can mitigate numerical instability in the solution when the disturbance is small. Note, however, that this will come at the expense of estimation accuracy when the disturbance is large, i.e., when the helicopter is in very close proximity to the ground. Overall, the fair agreement shown between the augmented ground proximity estimate and the data measured using the motion capture camera system demonstrates that it is feasible to estimate ground proximity in-flight using only measurements provided from inertial sensors. The implications of this result are discussed in more detail in Section 8.4.

8.3.2 Near-Ceiling Flight Test Results

For the near-ceiling flight test, the decoupled heave-yaw dynamics described by Equation (8.14) and the heave-yaw estimator gains provided in Equation (8.16) have been used to estimate the heave velocity and yaw-rate states as well as the exogenous vertical force disturbance that is induced by proximity to the ceiling plane. The state and disturbance estimation performance, as well as the passive ceiling proximity estimate, are evaluated in this subsection.

Heave velocity and yaw-rate state estimates made across 8 s of near-ceiling flight data are plotted in Figure 8.4. Both estimated states show very good agreement with the actual data measured using the motion capture camera system. RMS and peak errors for the heave velocity estimate are 0.0327 m/s and 0.0653 m/s respectively. RMS and peak errors for the yaw-rate estimate are 0.0230 rad/s and 0.0549 rad/s respectively. For both the heave velocity and yaw-rate estimates, RMS error is consistent with the near-ground state estimate errors outlined in Section 8.3.1. As was previously observed for the near-ground state estimates, the high accuracy of the yaw-rate estimate can be attributed to the fact that yaw-rate is directly measured on-board the micro helicopter test-bed using the z-axis gyroscope. Further to this, the high accuracy of the heave velocity estimate can be attributed to the strong dynamic coupling that exists between the heave velocity and yaw-rate states.

The estimate of the vertical force disturbance that is induced by aerodynamic ceiling proximity effects is plotted in Figure 8.5. Once again, this disturbance estimate cannot be directly validated because the actual disturbance that is induced by ceiling proximity cannot be directly measured during flight. Nonetheless, the accuracy of this disturbance estimate can be indirectly evaluated by using it to obtain a passive ceiling proximity estimate. Additionally, the accuracy of the disturbance estimate is further evaluated by comparison against CFD results in Section 8.4.2.

If it is assumed that a fair estimate of the vertical force disturbance induced by ceiling proximity has been made in Figure 8.5, and the relationship between ceiling proximity and vertical force disturbance is known based on the CFD results (see Equation (6.7)), the in-flight disturbance estimate can be used to passively estimate ceiling proximity from

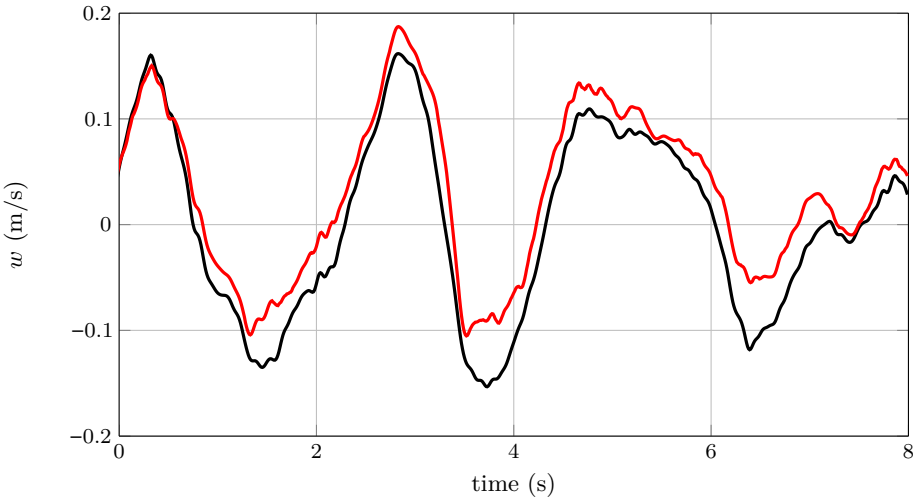

(a) Plot of heave velocity vs time.

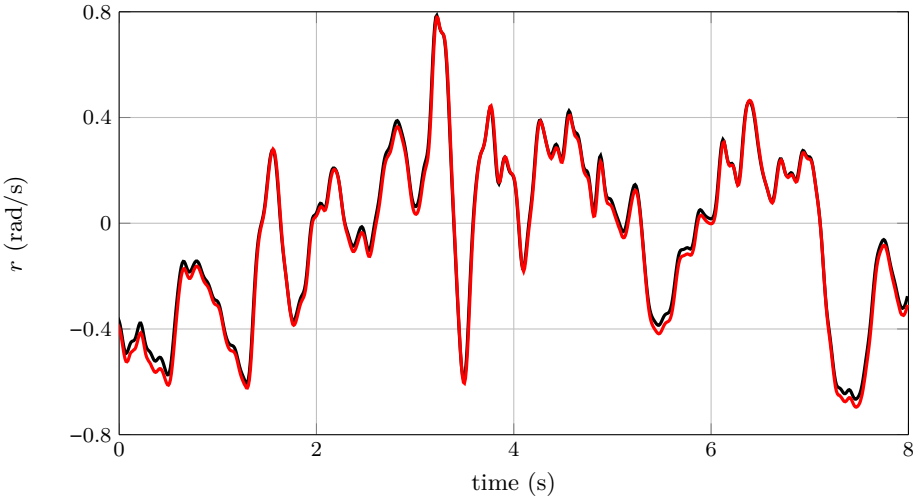

(b) Plot of yaw-rate vs time.

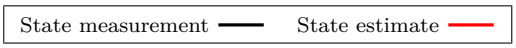

Figure 8.4: Comparison between actual and estimated heave/yaw states for a micro helicopter hovering in close proximity to a ceiling plane.

$$\hat{h}_c \approx \left(\frac{-0.056mg}{\hat{\bar{Z}}} \right)^{(1/1.619)} . \tag{8.22}$$

Once again, a constant, α_c, can be introduced into the denominator of Equation (8.22) to prevent numerical instability from driving the proximity estimate toward infinity as the disturbance estimate tends to zero

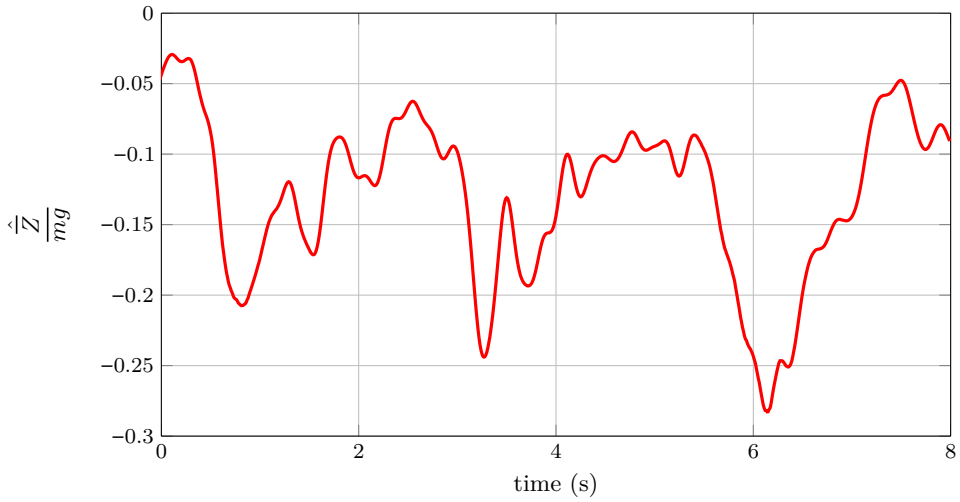

FIGURE 8.5: Plot of the estimate of the vertical force disturbance acting on a micro helicopter hovering in close proximity to a ceiling plane vs time.

$$\hat{h}_c \approx \left(\frac{-0.056mg}{\hat{\bar{Z}} + \alpha_c} \right)^{(1/1.619)} . \tag{8.23}$$

A plot of the passive ceiling proximity estimates vs time is provided in Figure 8.6, where the augmented proximity estimate is made by setting $\alpha_c = -0.01$. Both passive ceiling proximity estimates show fair agreement with the proximity measurement obtained using the motion capture camera system. For the ceiling proximity estimate made using Equation 8.22, the RMS error and peak error are $0.4230R$ and $1.3538R$ respectively. As expected, the large peak error is caused by the disturbance estimate nearing zero at 0.28 s. In contrast, for the ceiling proximity estimate made using Equation 8.23, the RMS error and peak error are $0.4133R$ and $0.9374R$ respectively. The 31% decrease in peak error demonstrates that augmenting the proximity estimate reduces sensitivity to numerical instability when the disturbance estimate nears zero. As was previously demonstrated for the near-ground case, the results presented in this subsection demonstrate the feasibility of using on-board inertial sensors to passively estimate proximity to a ceiling plane.

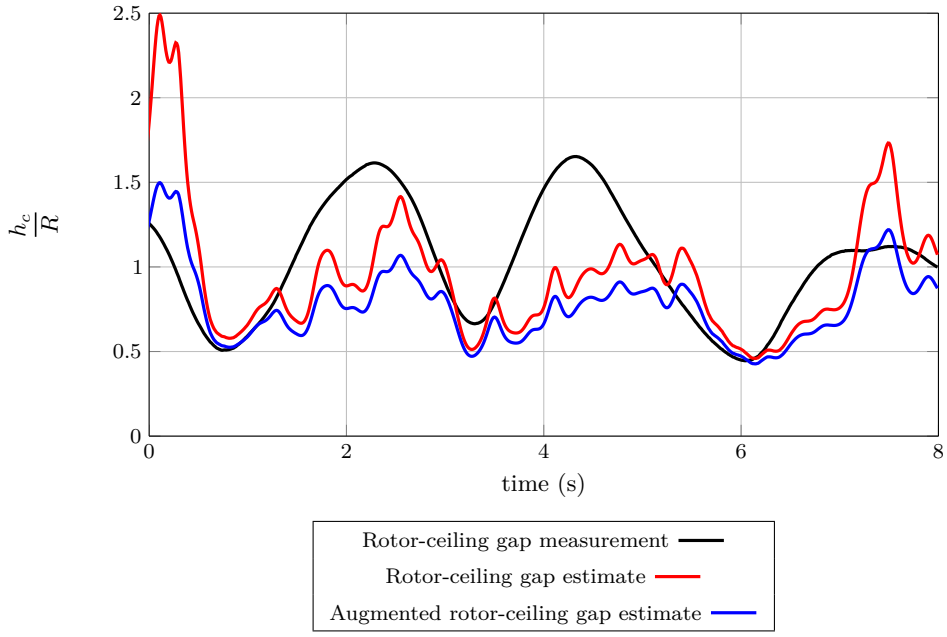

Figure 8.6: Comparison between actual and estimated ceiling proximity for a micro helicopter hovering in close proximity to a ceiling plane. Plot shows non-dimensionalised rotor-ceiling gap vs time.

8.3.3 Near-Wall Flight Test Results

For the near-wall flight test, the decoupled lateral-longitudinal dynamics described by Equation (8.17) and the lateral-longitudinal estimator gains provided in Equation (8.19) have been used to estimate the lateral and longitudinal states as well as the exogenous torque disturbances that are induced by proximity to a wall plane. The state and disturbance estimation performance, as well as the passive wall proximity estimate, are evaluated in this subsection.

In-flight estimates of longitudinal velocity, u, and lateral velocity, v, are plotted across 8 s of near-wall flight data in Figure 8.7. Measurements made using the motion capture camera system are also included for comparison. Both the longitudinal and lateral velocity estimates show fair agreement with the measured velocity data. RMS and peak errors for the longitudinal velocity estimate are 0.3266 m/s and 0.6839 m/s respectively. RMS and peak errors for the lateral velocity estimate are 0.2151 m/s and 0.4852 m/s respectively. Note that this accuracy is relatively poor when compared with the heave velocity estimates made in Sections 8.3.1 and 8.3.2. This can be attributed to uncertainty in the model parameters for the micro

helicopter test-bed that were previously identified in Section 3.3. In particular, identifying the stability derivatives that govern lateral and longitudinal velocity (X_u and Y_v) is difficult in practice, owing to the unstable nature of helicopter translational dynamics (Mettler, 2003). This model uncertainty contributes directly to the observed inaccuracies in the longitudinal and lateral velocity estimates, i.e., a more accurate model is required in order to improve the accuracy of translational velocity state estimates. Despite this, both the longitudinal and lateral velocity estimates have a bounded error, i.e., they are not subject to the unbounded drift that typically occurs when numerically integrating accelerometer measurements to obtain velocity estimates. As with the heave-yaw dynamics, strong coupling between translation velocities, rotor dynamics and helicopter attitude (which can be estimated on-board the helicopter) allows the simultaneous state and disturbance estimator to correct for drift in velocity estimates. This is a positive result, as it means that errors in the translation velocity state estimates will not cause significant error in the remaining state and disturbance estimates.

As was previously observed for the near-ground and near-ceiling flight tests, estimates of angular velocities show very close agreement with flight data collected using the motion capture camera system for the near-wall case. This is shown in Figure 8.8, where roll-rate and pitch-rate estimates are plotted across 8 s of near-wall flight data. For the roll-rate estimate, RMS error and peak error are 0.0722 rad/s and 0.2522 rad/s respectively. For the pitch-rate estimate, RMS error and peak error are 0.1903 rad/s and 0.6753 rad/s respectively. Once again, this error is consistent with the yaw-rate estimate errors shown in Sections 8.3.1 and 8.3.2 and is also consistent with the expected error of the gyroscopes on-board the micro helicopter test-bed.

The roll angle and pitch angle estimates obtained in-flight for a micro-helicopter hovering in close proximity to a wall plane show good agreement with measurements made using the motion capture camera system. This is shown in Figure 8.9, where roll angle and pitch angle estimates are plotted across 8 s of near-wall flight data. For the roll angle estimate, RMS error and peak error are 0.0492 rad and 0.1554 rad respectively. For the pitch angle estimate, RMS error and peak error are 0.1185 rad

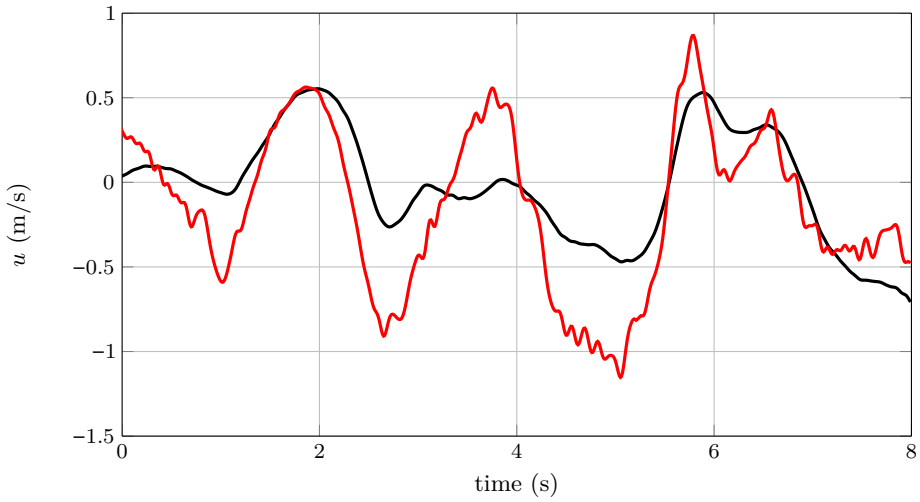

(a) Plot of longitudinal velocity vs time.

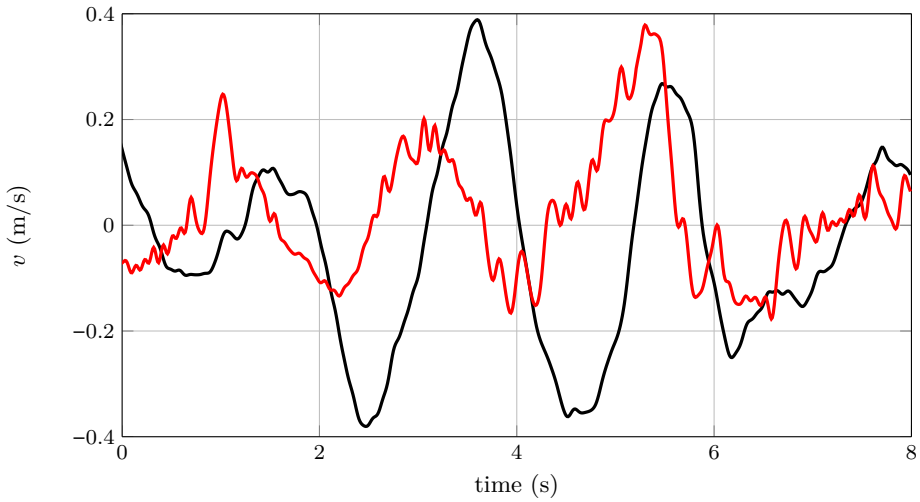

(b) Plot of lateral velocity vs time.

State measurement — State estimate

Figure 8.7: Comparison between actual and estimated lateral and longitudinal velocities for a micro helicopter hovering in close proximity to a wall plane.

and 0.2462 rad respectively. The good accuracy observed here is expected because roll and pitch angles are computed directly from accelerometer and gyroscope data on-board the micro helicopter test-bed, using the attitude filter outlined in Section 3.2.2.1. Note that there is a small offset in the pitch angle estimate of approximately −0.09 rad. This is most likely caused by a bias in the expected direction of the gravity vector due to minor misalignment of the on-board accelerometer. Nonetheless, roll angle and pitch angle estimation performance is adequate for the purposes of the research

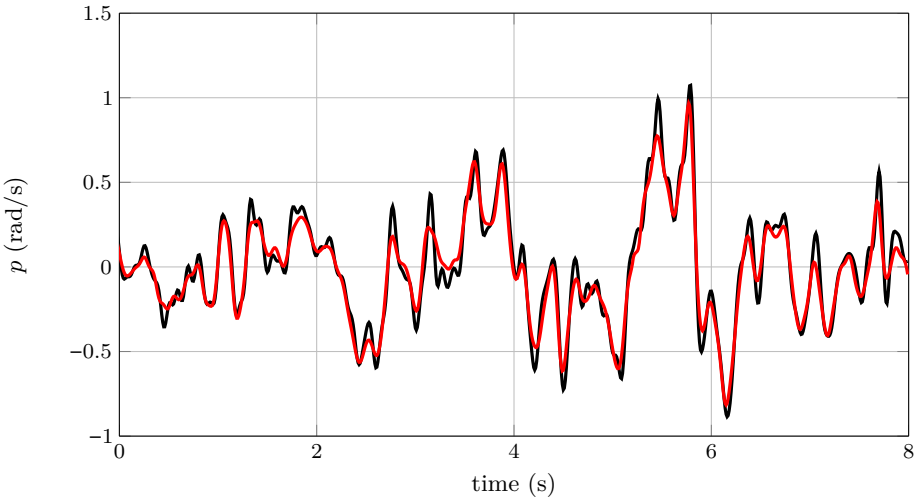

(a) Plot of roll-rate vs time.

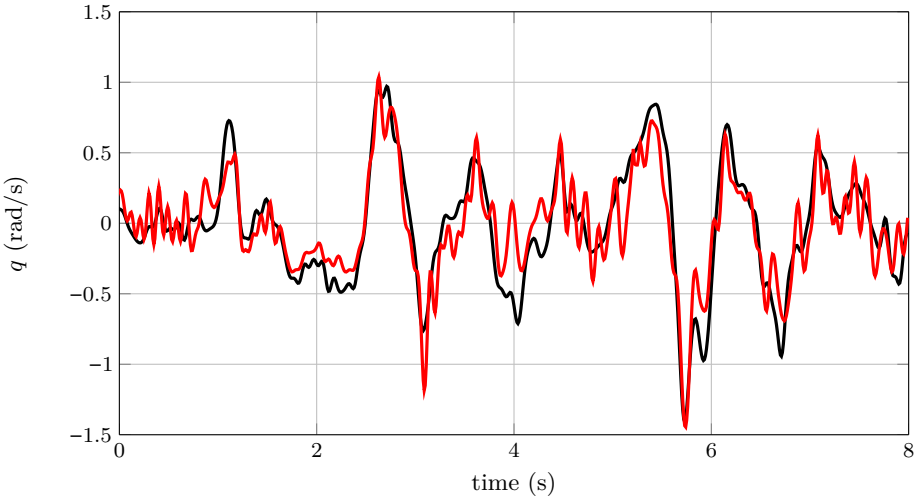

(b) Plot of pitch-rate vs time.

State measurement — State estimate

FIGURE 8.8: Comparison between actual and estimated roll-rate and pitch-rate for a micro helicopter hovering in close proximity to a wall plane.

outlined in this thesis.

Finally, estimates of the aerodynamic disturbances induced by proximity to the wall plane are plotted in Figure 8.10. Note that significant disturbances are detected about the both the x-axis and y-axis (in the helicopter's body-fixed frame). This is because these torque disturbances vary as a function of helicopter-wall angle, as previously defined in Equation (7.4). Note also that these disturbance estimates cannot be directly validated because the actual disturbances cannot be readily

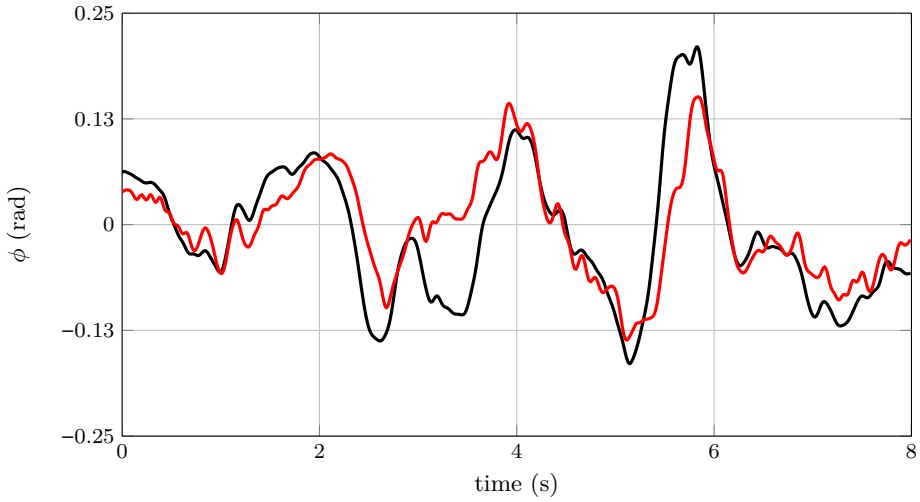

(a) Plot of roll angle vs time.

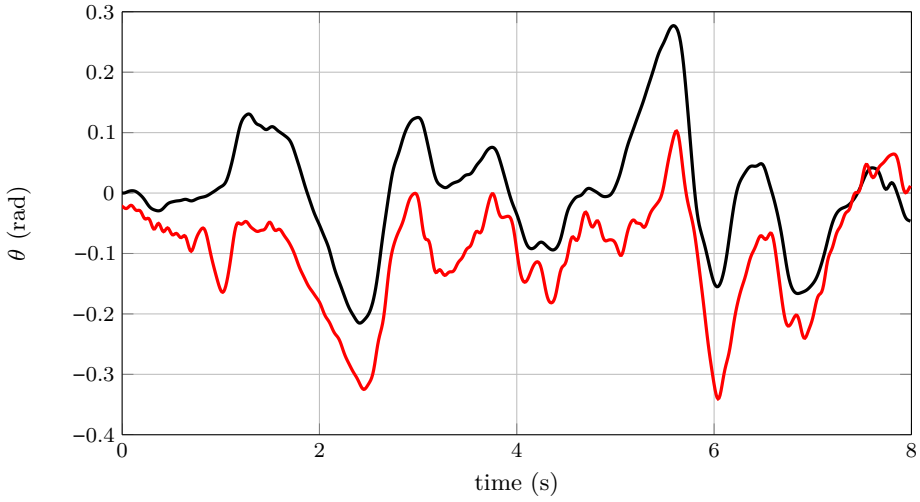

(b) Plot of pitch angle vs time.

State measurement — State estimate

Figure 8.9: Comparison between actual and estimated roll angle and pitch angle for a micro helicopter hovering in close proximity to a wall plane.

measured during flight. The accuracy of the disturbance estimates can, however, be evaluated indirectly by using the disturbance estimates to obtain passive proximity estimates. Additional evaluation of the accuracy of these disturbance estimates is conducted by comparison against CFD results in Section 8.4.2.

If it is assumed that fair estimates of the torque disturbances induced by wall proximity have been made in Figure 8.10, and the relationship between wall proximity and torque disturbances are known based on the CFD results (see Equation (7.4)),

the in-flight disturbance estimate can be used to passively estimate wall proximity and helicopter-wall angle from

$$\begin{aligned}\hat{h}_w &\approx R\left(1+\left(\frac{0.1283Q'}{\sqrt{\hat{\overline{L}}^2+\hat{\overline{M}}^2}}\right)^{(1/1.164)}\right),\\ \hat{\phi}_w &\approx -2\text{atan}\left(\frac{\hat{\overline{M}}+\sqrt{\hat{\overline{L}}^2+\hat{\overline{M}}^2}}{\hat{\overline{L}}}\right).\end{aligned} \tag{8.24}$$

As was previously outlined in Sections 8.3.1 and 8.3.2, Equation (8.24) will also encounter large errors when estimated disturbances are close to zero. Once again, to address this issue, a constant, α_w, has been included in Equation (8.24) to become

$$\begin{aligned}\hat{h}_w &\approx R\left(1+\left(\frac{0.1283Q'}{\sqrt{\left(\hat{\overline{L}}+\alpha_w\right)^2+\left(\hat{\overline{M}}+\alpha_w\right)^2}}\right)^{(1/1.164)}\right),\\ \hat{\phi}_w &\approx -2\text{atan}\left(\frac{\hat{\overline{M}}+\sqrt{\hat{\overline{L}}^2+\hat{\overline{M}}^2}}{\hat{\overline{L}}+\alpha_w}\right).\end{aligned} \tag{8.25}$$

Using Equations (8.24) and (8.25), passive estimates of wall proximity and helicopter-wall angle have been made in-flight when hovering in close proximity to a wall, where the augmented estimates are made by setting $\alpha_w = -3\cdot 10^{-5}$. These passive estimates are plotted across 8 s of flight data in Figure 8.11. For the estimate of rotor-wall gap made using Equation 8.24, RMS error and peak error are $1.6253R$ and $9.0192R$ respectively. This reduces to a RMS error and peak error of $1.4518R$ and $3.1185R$ respectively when using the augmented Equation 8.25 to estimate wall proximity. For the passive estimate of helicopter-wall angle made using Equation 8.24, RMS error and peak error are 25.7486° and 78.9120° respectively. This reduces to a RMS error and peak error of 13.8367° and 43.2604° respectively when using the augmented Equation 8.25 to estimate helicopter-wall angle. This result demonstrates that the augmented passive estimation method can reduce the large error that occurs

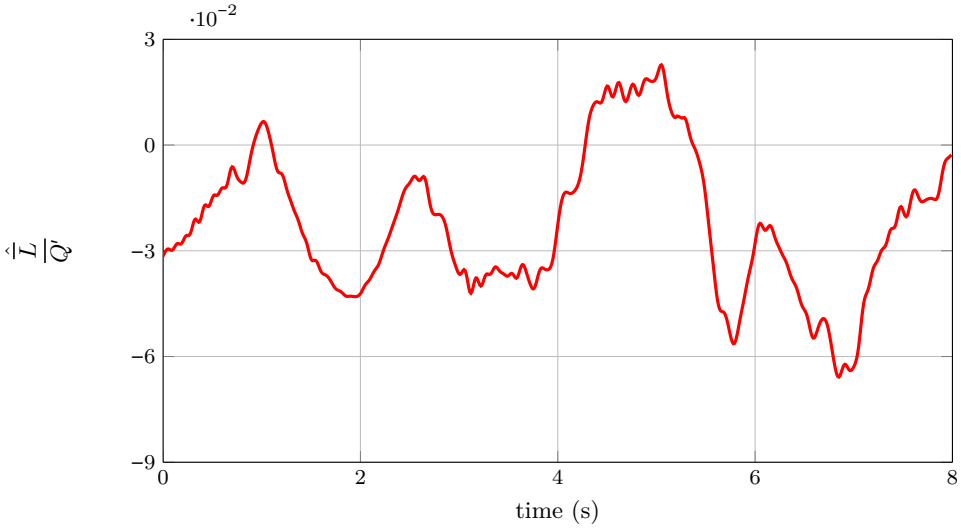

(a) Plot of x-axis torque disturbance vs time.

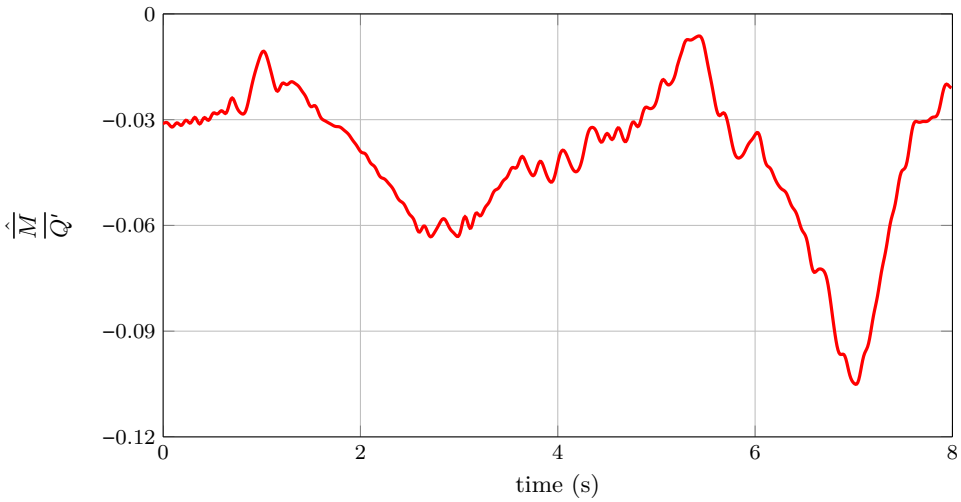

(b) Plot of y-axis torque disturbance vs time.

Figure 8.10: Estimates of the x-axis and y-axis torque disturbances acting on a micro helicopter hovering in close proximity to a wall plane.

when the disturbance estimates are close to zero. Overall, the augmented passive estimation method provides fair agreement with data measured experimentally using the motion capture camera system. Further discussion of this result is provided in Section 8.4.3.

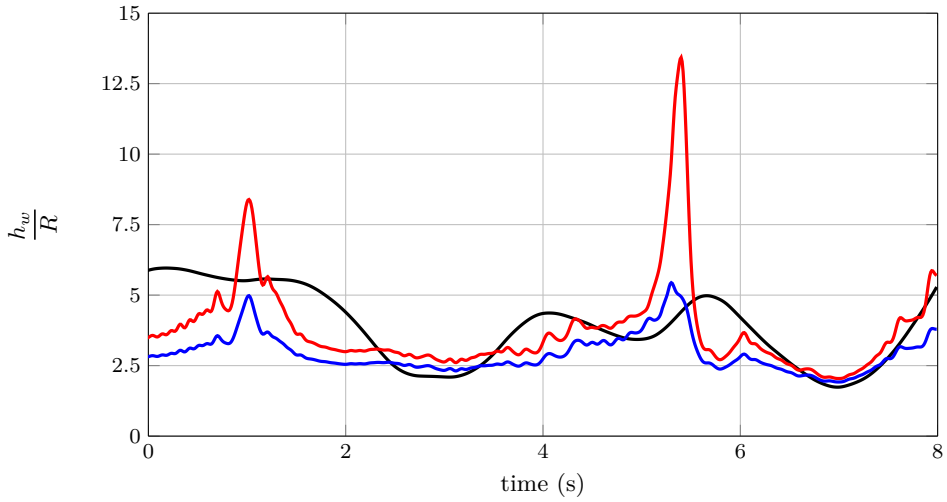

(a) Plot of rotor-wall gap vs time.

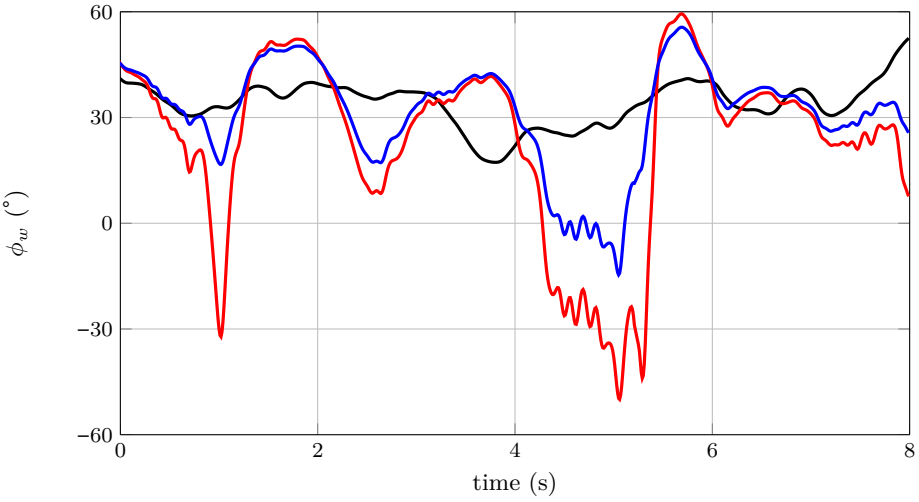

(b) Plot of helicopter-wall angle vs time.

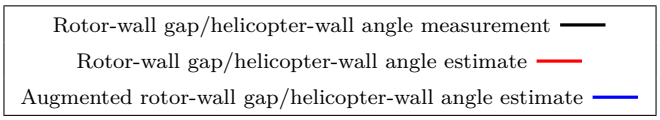

FIGURE 8.11: Comparison between actual and estimated wall proximity and helicopter-wall angle for a micro helicopter hovering in close proximity to a wall plane.

8.4 Discussion

8.4.1 State Estimation Performance

With the exception of the lateral and longitudinal velocity estimation performance, all the in-flight state estimation results presented in Figures 8.1, 8.4, 8.8 and 8.9

show good agreement with the state measurements made using the motion capture camera system. For the roll-rate, pitch-rate and yaw-rate state estimates, the high accuracy can be attributed to the fact that angular rates are measured directly on-board the micro helicopter test-bed. In this case, the state estimate accuracy is primarily limited by the accuracy of the MEMS gyroscope sensor used to obtain these measurements. Similarly, for the roll angle and pitch angle state estimates, the good estimation accuracy can be attributed to the fact that helicopter attitude is estimated on-board the micro helicopter test-bed using the attitude filter previously outlined in Section 3.2.2.1. Note that the performance of this attitude filter degrades as the helicopter deviates away from the hovering trim condition. Nonetheless, good attitude estimation accuracy is expected when the helicopter is close to its hovering state. Because angular rates and attitude angles are measured or estimated on-board the micro helicopter test-bed, estimates of these states will be largely unaffected by uncertainty in the model parameters identified in Section 3.3. In contrast, estimation of the heave velocity, longitudinal velocity and lateral velocity relies on having *a priori* knowledge of the cross coupling between different helicopter hovering states/dynamics. Knowledge of this cross coupling is required in order to correct for unbounded drift of velocity estimates due to numerical integration of accelerometer biases. In the case of the heave velocity, good estimation accuracy has been achieved, as shown in Figures 8.1(a) and 8.4(a). State estimation accuracy degrades slightly for the longitudinal velocity and lateral velocity results presented in Figure 8.8. As explained in Section 8.3.3, this degradation in translational velocity estimation performance occurs because helicopter horizontal translational dynamics are unstable and are, therefore, relatively difficult to identify accurately. A more accurate model of the translational dynamics would be required in order to improve the accuracy of these state estimates. Despite this, fair agreement is still shown between the horizontal translational velocity estimates and the data obtained using the motion capture camera system. This estimation accuracy has been deemed adequate for the purposes of the research outlined in this thesis.

8.4.2 Disturbance Estimation Performance

As previously stated, the disturbance estimation results presented in Figures 8.2, 8.5 and 8.10 cannot be directly validated because the actual disturbances that are induced by aerodynamic proximity effects cannot be readily measured during flight. Instead, in this subsection, the disturbance estimates are validated indirectly by comparison against CFD results. In Figure 8.12, the near-ground, near-ceiling and near-wall disturbance estimates are plotted against empirical fits to the CFD results (i.e., Equations (A.1), (6.7) and (7.4)). All of the disturbance estimate results show fair agreement with the CFD results, demonstrating that it is feasible to make in-flight estimates of disturbances that are induced by aerodynamics proximity effects. The discrepancy between the disturbance estimates and CFD results can be partially explained by noting that the CFD disturbance estimates assume that the helicopter is stationary. In practice, small deviations away from the hovering trim condition will cause some change in the disturbances that are induced by aerodynamic proximity effects. These deviations away from the hovering trim condition are not considered by the CFD method outlined in Chapter 4 - this will contribute to some of the discrepancy between the CFD disturbance estimate and the in-flight disturbance estimate. This discrepancy can also be further explained by examining the estimator error dynamics described by Equation (8.5), which show that the disturbance estimate error, $\boldsymbol{e_d}$, is dependant on the rate of change of the disturbance. In the case of a helicopter hovering in close proximity to a planar surface, the disturbance induced by aerodynamic proximity effects will vary as proximity varies. This suggests that the disturbance estimate error should increase as the helicopter moves away from the hovering trim condition. As demonstrated by the results presented in this chapter, the estimator can tolerate some deviation away from the hovering trim condition while still producing a fair estimate of the disturbance. Although not covered under the scope of this thesis, an interesting extension of this research would be to determine how far the helicopter can deviate from the hovering trim condition before the disturbance estimate becomes unusable.

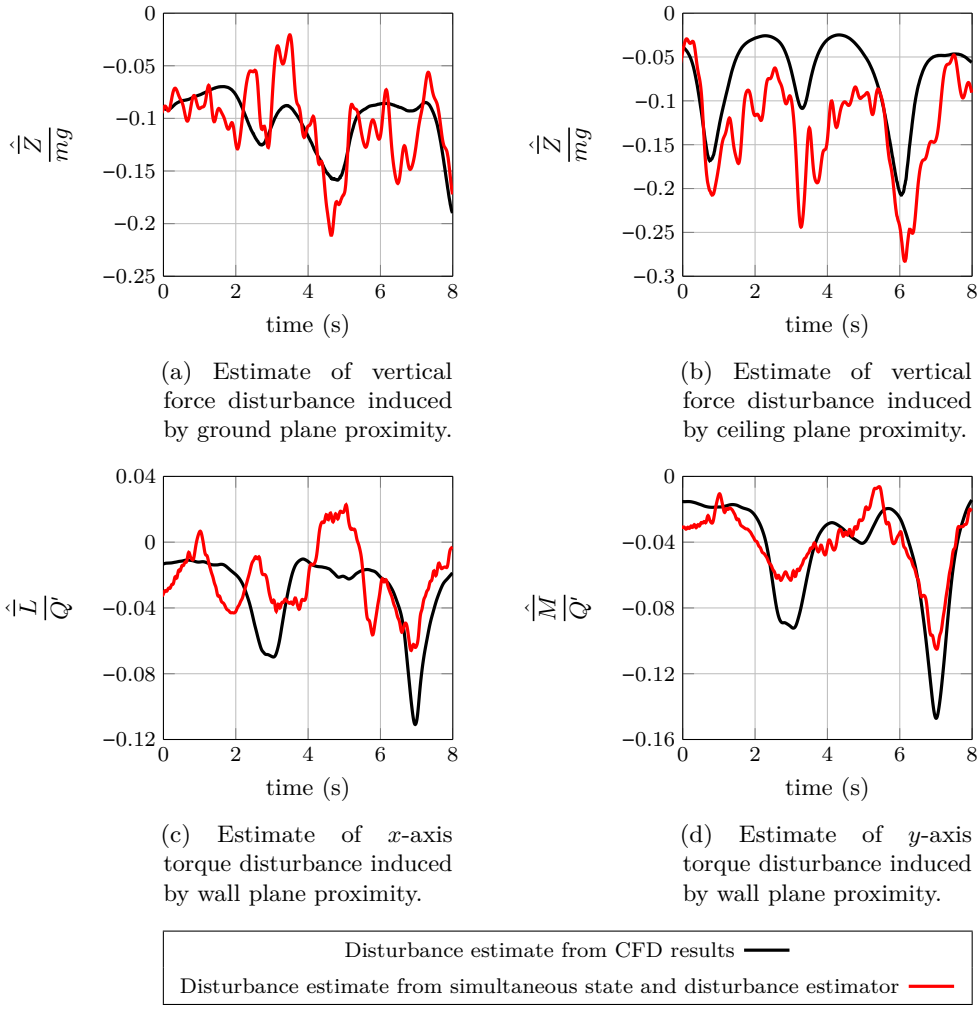

(a) Estimate of vertical force disturbance induced by ground plane proximity.

(b) Estimate of vertical force disturbance induced by ceiling plane proximity.

(c) Estimate of x-axis torque disturbance induced by wall plane proximity.

(d) Estimate of y-axis torque disturbance induced by wall plane proximity.

Figure 8.12: Comparison between in-flight disturbance estimates and disturbance estimates obtained from CFD results.

8.4.3 Passive Proximity Estimation Performance

The passive proximity estimation results presented in Figures 8.3, 8.6 and 8.11 provide strong evidence that it is feasible to estimate micro helicopter proximity to planar surfaces using only measurements obtained using on-board inertial sensors and *a priori* knowledge of the relationship between proximity and disturbance magnitude. For the near-ground, near-ceiling and near-wall cases tested experimentally in this chapter, fair proximity estimation accuracy is achieved. However, for all cases, large proximity estimate errors occur when the disturbance estimate is close to zero. This is because the passive proximity estimate will tend to infinity as the disturbance

estimate tends to zero. This means that a small error in the disturbance estimate (when the actual disturbance is close to zero) can result in a large error in the passive proximity estimate. This numerical instability has been mitigated by introducing a constant into the proximity estimation equations, as shown in Equations (8.21), (8.23) and (8.25). This error may also be compensated for by filtering the passive proximity estimate with an additional proximity measurement provided by an on-board proximity sensor (note that implementing such an augmented system is beyond the scope of this research). Alternatively, for some applications it may be necessary to only utilise the proximity estimate when it is below a pre-defined threshold. This may allow for collision avoidance systems to be activated once the micro-helicopter is deemed to be in close proximity to a planar surface.

A final important limitation to consider is the fact that, in its current formulation, the heave-yaw estimator is not able to distinguish between exogenous vertical force disturbances that are generated by a ground or ceiling plane. In practice, it will be necessary to estimate the disturbance at least two different rotor-ground or rotor-ceiling gaps to ascertain whether the disturbance has been induced by a ground plane or a ceiling plane.

8.4.4 Further Applications

Although outside the scope of this research, it is important to consider how the disturbance and passive proximity estimates obtained in this chapter may be used to improve the performance of micro helicopters when operating in confined environments. Given that the disturbance estimates show fair agreement with validated CFD results, as shown in Figure 8.12, it is feasible to use the disturbance estimates to compensate for the disturbance. Such disturbance estimator-based control systems have been applied to MAVs in the existing literature. In particular, Liu et al. (2012) successfully demonstrated that a non-linear disturbance estimator-based control system may be used to compensate for wind gust disturbances acting on a quad rotor. In its simplest form, a disturbance estimator-based control system would seek to generate a control input that compensates for the disturbance

$$\boldsymbol{u} = -\boldsymbol{K}\hat{\boldsymbol{d}}, \tag{8.26}$$

where the controller gain, $\boldsymbol{K}$, can be computed from

$$\boldsymbol{K} = \left(\boldsymbol{B_u}^T \boldsymbol{B_u}\right)^{-1} \boldsymbol{B_u}^T \boldsymbol{B_d}. \tag{8.27}$$

Using such a control system to autonomously compensate for disturbances that are induced by aerodynamic proximity effects will reduce the risk of colliding with obstacles, improving the overall performance of micro helicopters within confined environments.

As an extension to this, the passive proximity estimates may be used as a basis for implementing collision avoidance systems. For example, the micro helicopter may be programmed to perform an evasive manoeuvre if the proximity estimate falls below a pre-defined threshold. In addition to this, with some refinement to the proximity estimate accuracy, it may be feasible to use the proximity estimate to maintain hover at a fixed distance away from a ground, ceiling or wall plane. Note also that, at present, existing collision avoidance systems typically rely on exteroceptive proximity sensors or GPS in order to detect obstacles. A major contribution of the research outlined in this chapter is the demonstration of the feasibility of using on-board inertial sensors only to estimate proximity to obstacles. This is an important development for micro helicopters, that already have strict payload constraints owing to their small size. The passive proximity estimation technique outlined in this chapter mitigates the need for accommodating additional sensors, which will, in turn, improve the flight time and payload capacity for micro helicopters.

8.5 Summary

This chapter postulates a novel linear simultaneous state and disturbance estimator for estimating exogenous disturbances acting on a micro helicopter due to aerodynamic proximity effects. The estimator relies only on measurements provided from on-board inertial sensors (i.e., MEMS accelerometers and gyroscopes) and consid-

ers the effects of direct feed-through of exogenous force disturbances to measured acceleration outputs. The estimator is applied to the micro helicopter test-bed dynamics previously identified in Section 3.3 by ignoring the weak coupling that exists between hovering heave-yaw dynamics and hovering lateral-longitudinal dynamics. The estimator's performance has been evaluated using experimental flight data obtained while hovering the micro helicopter test-bed near to a ground plane, ceiling plane and wall plane. The estimator has been shown to produce accurate estimates of helicopter states and the disturbance estimates show fair agreement with the validated CFD results. Finally, the disturbance estimates, along with *a priori* knowledge of how the disturbance varies with ground, ceiling or wall proximity have been used to obtain passive estimates of proximity to a ground plane, ceiling plane or wall plane. The passive proximity estimates show fair agreement with measurements made using the motion capture camera system. This is a key contribution of this research, as it demonstrates the feasibility of using only on-board inertial sensors for detecting planar obstacles during flight.

Chapter 9

Conclusions and Recommendations for Future Work

This thesis investigates the aerodynamic disturbances that act on a hovering micro helicopter due to fluid interactions between the main rotor and nearby planar surfaces. The fluid dynamics that drive these aerodynamic disturbances have been modelled computationally and a disturbance estimation scheme has been postulated for estimating these disturbances during flight. Concluding remarks and key findings are presented in Section 9.1 and recommendations for future work are presented in Section 9.2 of this chapter.

9.1 Conclusions

For a hovering micro rotor in close proximity to a ceiling plane, the CFD results presented in Chapter 6 demonstrate that the ceiling plane will obstruct the vertical component of fluid momentum upstream of the rotor. To compensate for this, upstream flow is drawn into the rotor by moving predominantly parallel to the ceiling plane, i.e., in the inward radial direction. This effect drives an increase in the radial contraction of the downstream wake with decreasing rotor-ceiling gap. The transfer of fluid momentum from the vertical to the radial direction also causes

a decrease in the induced velocity through the rotor disk. For a given rotor, it is shown that the change in induced velocity is inversely proportional to the rotor-ceiling gap. The decrease in induced velocity with decreasing rotor-ceiling gap causes an increase in the local effective angle of attack along the rotor blades. In addition to this, an increase in the localised curl in the velocity field as flow moving predominantly parallel to the ceiling plane is drawn into the wake causes an increase in the circulation within the blade tip vortex. The increases in local effective angle of attack and circulation are the primary mechanisms that drive an increase in rotor thrust with decreasing rotor-ceiling gap. The relationship between thrust and rotor-ceiling gap can be fitted to a power-law curve. Note also that rotor thrust increases faster than rotor power, i.e., rotor efficiency will improve with decreasing rotor-ceiling gap.

For a hovering micro rotor in close proximity to a wall plane, the CFD results presented in Chapter 7 demonstrate that the wall plane will obstruct the component of fluid momentum in the direction normal to the wall at the near-wall side of the flow field. To conserve momentum, flow through the near-wall side of the rotor disk moves predominantly parallel to the wall plane. The decrease in the radial component of fluid momentum near the wall means that there is less momentum opposing radial contraction at the far-wall side of the flow field. This drives an increase in the radial component and a decrease in the vertical component of flow velocity through the far-wall side of the rotor disk. Ultimately, these changes in the vertical component of flow velocity that are induced by the wall plane cause a significant increase in the local effective angle of attack at the far-wall rotor blade. This creates a thrust imbalance across the rotor-disk, generating a torque about the horizontal axis parallel to the wall (defined as the y-axis in this thesis). The magnitude of the torque increases with decreasing rotor-wall gap. This torque is particularly problematic for micro helicopters as it will likely rotate the micro helicopter, which will in turn generate a horizontal component of thrust, accelerating the helicopter directly toward the wall.

The novel simultaneous state and disturbance estimator postulated in Chapter 8 demonstrates that the aerodynamic disturbances that are induced by proximity to

a ground plane, ceiling plane or wall plane can be estimated in-flight using only measurement provided by on-board inertial sensors. Note also that the estimator can be applied to any linear system, providing that the observability criteria described in Section 8.1.3 holds. A novel contribution of the estimator is that it accounts for direct feed-through of exogenous force disturbances to measured accelerations. The flight test results presented in Section 8.3, clearly demonstrate that a fair estimate of proximity effect disturbances can be obtained using the simultaneous state and disturbance estimator. Note also that good estimates of translational velocity can also be obtained, because cross coupling between angular velocity states and translational velocity states can be used to correct for unbounded drift in velocity estimates.

Finally, the flight test results demonstrate that the disturbance estimate, along with *a priori* knowledge of the relationship between the disturbance and proximity to a planar surface, can be used to passively estimate proximity to a planar surface. While the accuracy of the passive proximity estimate will encounter some numerical instability when far from the planar surface, it is nonetheless still valuable for implementing micro helicopter collision avoidance systems. This is a major contribution of the research outlined in this thesis, as it demonstrates that proximity detection and collision avoidance systems can be feasibly implemented on-board a micro helicopter without requiring additional exteroceptive proximity sensors. Mitigating the need for additional sensors will free-up power and payload capacity, improving the effectiveness of micro helicopters in confined environments.

In summary, and with reference to the research objectives outlined in Section 1.2, the key findings of this research are:

- Fluid interactions between a hovering micro rotor and a horizontal ceiling plane will drive an increase in rotor thrust and an increase in aerodynamic efficiency as rotor-ceiling gap decreases.

- Fluid interactions between a hovering micro rotor and a vertical wall plane will induce asymmetry in the wake which will generate a torque about the horizontal axis parallel to the wall (i.e., the global frame y-axis defined in

Figure 7.5). This torque will increase in magnitude as rotor-wall gap decreases.

- By treating the changes in force/torque that are induced by proximity to a planar surface as exogenous disturbances, the changes in force/torque may be estimated in-flight using measurements obtained from on-board inertial sensors.

- The disturbance estimate, along with *a priori* knowledge of how the disturbance varies with proximity to a planar surface, may be used to obtain a passive estimate of proximity to a planar surface.

9.2 Recommendations for Future Work

While this thesis addresses the fundamentals of modelling and estimation of aerodynamic disturbances that are induced by micro rotor proximity to planar surfaces, the author acknowledges that future work is required in order to build on the body of research outlined in this thesis:

- In addition to ground, ceiling and wall planes, a micro helicopter will likely encounter inclined surfaces as well as irregular shaped obstacles when operating within a confined environment. Therefore, an important extension of this research would be the investigation of fluid interactions between a micro rotor and inclined surfaces or irregular obstacles. In addition to this, it is also important to investigate fluid interactions for a non-hovering rotor. This body of research would help to understand the full range of fluid phenomena that a micro rotor will encounter within a confined environment.

- Multi rotor helicopters are rapidly growing in popularity, in particular at a micro scale where their mechanical simplicity is favoured. Therefore, it is likely that the research outlined in this thesis will need to be extended to the multi rotor case. This will introduce additional complexity to the fluid interactions, as multiple blade tip vortices will be passing near each other and near to the planar surface obstacle.

- The error dynamics of the simultaneous state and disturbance estimator is governed by the rate of change of the disturbance. For a micro helicopter in close proximity to a planar surface, the induced disturbance will vary as the helicopter translates/rotates. Therefore, the accuracy of the disturbance estimate will degrade as the velocity of the helicopter increases. An important addition to this research would be the design of a non-linear simultaneous state and disturbance estimator that accounts for changes in the disturbance.

- Finally, the accuracy of the passive proximity estimation scheme may be improved by filtering the passive proximity estimate with an additional proximity measurement. An interesting extension of this research would be to use a low-weight/low-cost proximity sensor to improve the accuracy of the passive proximity estimate.

References

3M Industrial Business. *3M Scotchlite High Gain Reflective Sheeting 7610*. 3M Industrial Business, 2003.

Ira H. Abbott and Albert E. Von Doenhoff. *Theory of Wing Sections: Including a Summary of Airfoil Data*. Dover Publications, Inc., 1959.

Bilal Ahmed and Hemanshu Roy Pota. Dynamic compensation for control of a rotary wing uav using positive position feedback. *Journal of Intelligent and Robotic Systems*, 61(1):43–56, 2011.

K. Alexis, C. Huerzeler, and R. Siegwart. Hybrid modeling and control of a coaxial unmanned rotorcraft interacting with its environment through contact. In *2013 IEEE International Conference on Robotics and Automation*, pages 5417–5424, 2013.

ANSYS, Inc. *ANSYS CFX - Solver Theory Guide*. ANSYS, Inc., 275 Technology Drive, Canonsburg, PA 15317, 15.0 edition, November 2013.

A. F. Antoniadis, D. Drikakis, B. Zhong, G. Barakos, R. Steijl, M. Biava, L. Vigevano, A. Brocklehurst, O. Boelens, M. Dietz, M. Embacher, and W. Khier. Assessment of cfd methods against experimental flow measurements for helicopter flows. *Aerospace Science and Technology*, 19:86–100, 2012.

P. Apkarian and D. Noll. Nonsmooth h-infinity synthesis. *IEEE Transactions on Automatic Control*, 51(1):71–86, 2006.

Atmel Corporation. *AVR2015: RZRAVEN Quick Start Guide*. Atmel Corporation, 2007.

Atmel Corporation. *ATMEL AVR Low Power 2.4 GHz Transceiver for ZigBee, IEEE 802.15.4, 6LoWPAN, RF4CE, SP100, WirelessHART, and ISM Applications*. Atmel Corporation, 2009.

Atmel Corporation. *ATmega48A/PA/88A/PA/168A/PA/328/P*. Atmel Corporation, 2014.

Chenyuan Bai and Zinui Wu. Generalized kutta-juokowski theorem for multi-vortex and multi-airfoil flow (a lumped vortex model). *Chinese Journal of Aeronautics*, 27(1):34–39, 2014.

Lenaick Besnard, Yuri B. Shtessel, and Brian Landrum. Control of a quadrotor vehicle using sliding mode disturbance observer. In *2007 American Control Conference*, 2007.

M. J. Bhagwat and J. G. Leishman. Accuracy of straight-line segmentation applied to curvilinear vortex filaments. *Journal of the American Helicopter Society*, 46(2): 166–169, 2001.

Lutz Bierl. Msp430 family mixed-signal microcontroller application reports. Technical report, Texas Instruments, 2000.

F. Bohorquez, P. Samuel, J. Sirohi, D. Pines, L. Rudd, and R. Perel. Design, analysis and hover performance of a rotary wing micro air vehicle. *Journal of the American Helicopter Society*, 48:80–90, 2003a.

Felipe Bohorquez and Darryll Pines. Hover performance of rotor blades at low reynolds numbers for rotary-wing micro air vehicles. In *"Unmanned Unlimited" Systems, Technologies, and Operations*, 2003.

Felipe Bohorquez, Falcon Rankins, James D. Baeder, and Darryll Pines. Hover performance of rotor blades at low reynolds numbers for rotary wing micro air vehicles - an experimental and cfd study. In *21st Applied Aerodynamics Conference*, 2003b.

N.A. Bruisma and M. Steinbuch. A fast algorithm to compute the h_∞-norm of a transfer function matrix. *System Control Letters*, 14:287–293, 1990.

A. Bry, A. Bachrach, and N. Roy. State estimation for aggressive flight in gps-denied environments using onboard sensing. In *2012 IEEE International Conference on Robotics and Automation*, 2012.

F. X. Caradonna and C. Tung. Experimental and analytical studies of a model helicopter rotor in hover. Technical Report NASA-TM-81232, National Aeronautics and Space Administration, 1981.

J. C. Cheeseman and W. E. Bennett. The effect of the ground on a helicopter rotor in forward flight. Technical report, Ministry of Supply - Aeronautical Research Council Reports and Memoranda, 1955.

H. C. Chen, V. C. Patel, and S. Ju. Solutions of reynolds-averaged navier-stokes equations for three-dimensional incompressible flows. *Journal of Computational Physics*, 88(2):305–336, 1990.

J. Chen, R. J. Patton, and H. Zhang. Design of unknown input observers and robust fault detection filters. *International Journal of Control*, 63(1):85–105, 1995.

Li Chen and Phillip McKerrow. Modelling the lama coaxial helicopter. In *Proceedings of the Australian Conference on Robotics and Automation*, 2007.

R. Chen. Effects of primary rotor parameters on flapping dynamics. Technical Report TP-1431, NASA, 1980.

A. Cheng and D. T. Cheng. Heritage and early history of the boundary element method. *Engineering Analysis with Boundary Elements*, 29:268–302, 2005.

Siu-Wing Cheng, Tamal Krishna Dey, and Jonathan Richard Shewchuk. *Delaunay Mesh Generation.* CRC Press, 2012.

Wooyoung Choi, Seunghoon Lee, Jiyoung Jung, and Soogab Lee. New far-field boundary and initial conditions for computation of rotors in vertical flight using vortex tube model. *Journal of the American Helicopter Society*, 53:382–397, 2008.

Marco La Civita, George Papageorgiou, William Messner, and Takeo Kanade. Design and flight testing of a high-bandwidth h-infinity loop shaping controller for a

robotic helicopter. In *AIAA Guidance, Navigation, and Control Conference and Exhibit*, 2002.

Joseph Conroy, Sean Humbert, and Darryll Pines. System identification of a rotary-wing micro air vehicle. *Journal of the American Helicopter Society*, 56: 025001–1–025001–4, 2011.

J. Cooley, P. Lewis, and P. Welch. The finite fourier transform. *IEEE Transactions on Audio and Electroacoustics*, 17(2):77–85, 1969.

M. Costes, T. Renaud, and B. Rodriguez. Rotorcraft simulations: a challenge for cfd. *International Journal of Computational Fluid Dynamics*, 26:383–405, 2012.

H. C. Curtiss, M. Sun, W. F. Putman, and E. J. Hanker. Rotor aerodynamics in ground effect at low advance ratios. *Journal of the American Helicopter Society*, 29(1):48–55, 1984.

Mark Cutler, N. Kemal Ure, Bernard Michini, and Jonathan P. How. Comparison of fixed and variable pitch actuators for agile quadrotors. In *AIAA Guidance, Navigation, and Control Conference*, 2011.

Dacell. *Load Cell and Torque*. Dacell, 2014.

Hector Garcia de Marina, Felipe Espinosa, and Carlos Santos. Adaptive uav attitude estimation employing unscented kalman filter, foam and low-cost mems sensors. *Sensors*, 12:9566–9585, 2012.

J. Meijer Drees and W. P. Hendal. Airflow patterns in the neighbourhood of helicopter rotors: A description of some smoke tests carried out in a wind-tunnel at amsterdam. *Aircraft Engineering and Aerospace Technology*, 23(4):107–111, 1951.

K. Duraisamy and J. Baeder. High resolution wake capturing methodology for hovering rotors. *Journal of the American Helicopter Society*, 52(2):110–122, 2007.

K. Duraisamy, M. Ramasamy, J. Baeder, and G. Leishman. High resolution computational and experimental investigation of hovering rotor tip vortex formation. *AIAA Journal*, 45(11):2593–2602, 2007.

Karthikeyan Duraisamy. *Studies in Tip Vortex Formation, Evolution and Control.* PhD thesis, University of Maryland at College Park, 2005.

Fairchild Semi Conductor Corporation. *QRE1113, QRE1113GR Miniature Reflective Object Sensor.* Fairchild Semi Conductor Corporation, 2015.

F. W. Fairman, S. S. Mahil, and L. Luk. Disturbance decoupled observer design via single value decomposition. *IEEE Transactions on Automatic Control*, 29(1): 84–86, 1984.

Caizhi Fan, Shengpeng Guo, Dongxu Li, and Yunhui Liu. Nonlinear predictive attitude control with a disturbance observer of an unmanned helicopter on the test bench. In *IEEE 5th International Conference on Robotics, Automation and Mechatronics*, 2011.

P. Fankhauser, S. Bouabdallah, S. Leutenegger, and R. Siegwart. Modeling and decoupling control of the coax micro helicopter. In *Intelligent Robots and Systems (IROS), 2011 IEEE/RSJ International Conference on*, pages 2223 –2228, 2011.

W. Froude. On the elementary relation between pitch, slip and propulsive efficiency. *Transactions of the Institute of Naval Architects*, 19:47–57, 1878.

G. P. Galdi. *An Introduction to the Mathematical Theory of the Navier-Stokes Equations.* Springer New York, 2011.

H. Glauert. *Airplane Propellers.* Springer Verlag, 1935.

J. Grauer, J. Conroy, J. Hubbard, J. Humbert, and D. Pines. System identification of a miniature helicopter. *Journal of Aircraft*, 46(4):1260–1269, 2009.

Mohinder S. Grewal and Angus P. Andrews. Applications of kalman filtering in aerospace 1960 to present. *IEEE Control Systems Magazine*, 3:69–78, 2010.

Daniel A. Griffiths, Shreyas Ananthan, and J. Gordon Leishman. Predictions of rotor performance in ground effect using a free-vortex method. *Journal of the American Helicopter Society*, 50(4):302–214, 2005.

B. Guerreiro, C. Silvestre, R. Cunha, and D. Antunes. Trajectory tracking h2 controller for autonomous helicopters: An application to industrial chimney inspection. In *17th IFAC Symposium on Automatic Control in Aerospace*, 2007.

S. Guntur and N. N. Sorensen. An evaluation of several methods of determining the local angle of attack on wind turbine blades. *Journal of Physics: Conference Series*, 555, 2014.

F. B. Gustafson and A. Gessow. Effect of rotor tip speed on helicopter rotor performance and maximum forward speed. Technical Report NACA ARR No. L6A16, National Advisory Committee for Aeronautics (NACA), 1946.

Anna Haggstrom. Connecting thrust and torque with the wake tip vortex geometry - application to wind turbines and propellers. Technical report, Swedish Defence Research Agency, 2001.

Jeremiah Hall. Low reynolds number aerodynamics for micro aerial vehicles. Master's thesis, University of Colorado, 2004.

J. Han. A class of extended state observers for uncertain systems. *Control and Decision*, 10(1):85–88, 1995.

R. S. Hansen. Toward a better understanding of helicopter stability derivatives. *Journal of the American Helicopter Society*, 29(1):15–24, 1982.

N. Hariharan, A. Wissink, M. Steffen, and M. Potsdam. Tip vortex field resolution using an adaptive dual-mesh computational paradigm. In *49th AIAA Aerospace Sciences Meeting*, 2011.

J. S. Hayden. The effect of the ground on helicopter hovering power required. In *32nd Annual National V/STOL Forum of The American Helicopter Society*, 1976.

W. T. Higgins. A comparison of complementary and kalman filtering. *IEEE Transactions of Aerospace and Electronic Systems*, 11(3):321–325, 1975.

Honeywell. *3-Axis Digital Compass IC HMC5843*. Honeywell, 2010.

Horizon Hobby, Inc. *Blade Nano CPX Instruction Manual.* Horizon Hobby, Inc., Champaign, IL USA, August 2012.

A. Hurwitz. Ueber die bedingungen, unter welchen eine gleichung nur wurzeln mit negativen reellen teilen besitzt. *Mathematische Annalen Nr.*, 46, 1895.

InvenSense, Inc. *ITG-3200 Product Specification Revision 1.7.* InvenSense, Inc., 2011.

S. Iqbal, C. Edwards, and A. I. Bhatti. Robust feedback linearization using higher order sliding mode observer. In *50th IEEE Conference on Decision and Control and European Control Conference*, 2011.

Javier Irizarry, Masoud Gheisari, and Bruce N. Walker. Usability assessment of drone technology as safety inspection tools. *Journal of Information Technology in Construction*, 17:194–212, 2012.

W. Johnson. *Helicopter Theory.* Princeton University Press, 1980.

S. J. Julier and J. K. Uhlmann. A new extension of the kalman filter to nonlinear systems. In *Aerosense: The 11th International Symposium on Aerospace/Defense Sensing, Simulation and Controls*, 1997.

R. E. Kalman. A new approach to linear filtering and prediction problems. *Transactions of the ASME Journal of Basic Engineering*, 82:35–45, 1960.

Tarandeep S. Kalra. *CFD Modeling and Analysis of Rotor Wake in Hover Interacting with a Ground Plane.* PhD thesis, University of Maryland, 2014.

K. Kalsi, J. Lian, S. Hui, and S. H. Zak. Sliding-mode observers for systems with unknown inputs: a high-gain approach. *Automatica*, 46:347–353, 2010.

Joseph Katz and Allen Plotkin. *Low-Speed Aerodynamics.* Cambridge University Press, 2001.

M. Khalid and D. J. Jones. Navier-stokes investigation of blunt trailing-edge airfoils using o grids. *Journal of Aircraft*, 30(5):797–800, 1993.

Kionix. *± 2g Tri-axis Digital Accelerometer Specifications*. Kionix, 2010.

V. Klein and E. Morelli. *Aircraft System Identification Theory and Practice*. American Institute of Aeronautics and Astronautics, Inc., 2006.

Arnaud Koehl, Hugues Rafaralahy, Mohamed Boutayeb, and Bastien Martinez. Aerodynamic modelling and experimental identification of a coaxial-rotor uav. *Journal of Intelligent and Robotic Systems*, 68:53–68, 2012.

Vijay Kumar and Nathan Michael. Opportunities and challenges with autonomous micro aerial vehicles. *The International Journal of Robotics Research*, 31:1279–1291, 2012.

S. Kwon and W. K. Chung. Combined synthesis of state estimator and perturbation observer. *Journal of Dynamic Systems, Measurement and Control*, 125:85–105, 2003.

SangJoo Kwon and Wan Kyun Chung. *Perturbation Compensator based Robust Tracking Control and State Estimation of Mechanical Systems*. Springer, 2004.

Vinod K. Lakshminarayan. *Computational Investigation of Micro-Scale Coaxial Rotor Aerodynamics in Hover*. PhD thesis, University of Maryland, 2009.

Vinod K. Lakshminarayan and James D. Baeder. High-resolution computational investigation of trimmed coaxial rotor aerodynamics in hover. *Journal of the American Helicopter Society*, 54:042008–1–042008–21, 2009.

Vinod K. Lakshminarayan and James D. Baeder. Computational investigation of micro hovering rotor aerodynamics. *Journal of the American Helicopter Society*, 55:022001–1–022001–25, 2010a.

Vinod K. Lakshminarayan and James D. Baeder. Computational investigation of microscale coaxial-rotor aerodynamics in hover. *Journal of Aircraft*, 47(3):940–955, 2010b.

Vinod K. Lakshminarayan, Tarandeep S. Kalra, and James D. Baeder. Detailed computational investigation of a hovering microscale rotor in ground effect. *AIAA Journal*, 51(4):893–909, 2013.

Peter Lancaster and Leiba Rodman. *Algebraic Riccati Equations.* Oxford University Press, 1995.

Anton J. Landgrebe. The wake geometry of a hovering helicopter rotor and its influence on rotor performance. *Journal of the American Helicopter Society*, 17 (1):3–15, 1972.

Anton J. Landgrebe and Elton D. Bellinger. An investigation of the quantitative applicability of model helicopter rotor wake patterns obtained from a water tunnel. Technical Report 71-69, United States Army Air Mobility Research and Development Laboratory, 1971.

Pierre-Simon Laplace. Mémoire sur la théorie de l'anneau de saturne. *Hist. Acad. Sci. Paris*, 1787.

E. Lee, H. Shim, H. Park, and K. Lee. Design of hovering attitude controller for a model helicopter. In *Proceedings of society of instrument and control engineers*, 1993.

Timothy Lee, J. Gordon Leishman, and Manikandan Ramasamy. Fluid dynamics of interacting blade tip vortices with a ground plane. *Journal of the American Helicopter Society*, 55(2):22005–1–22005–16, 2010.

J. Gordon Leishman. *Principles of Helicopter Aerodynamics.* Cambridge University Press, 2006.

J. Gordon Leishman and Bradley Johnson. Engineering analysis of the 1907 cornu helicopter. *Journal of the American Helicopter Society*, 54(3), 2009.

J. Gordon Leishman, Mahendra J. Bhagwat, and Ashish Bagai. Free-vortex filament methods for the analysis of helicopter rotor wakes. *Journal of Aircraft*, 39(5): 759–775, 2002.

Shihua Li, Jun Yang, Wen-Hua Chen, and Xisong Chen. *Disturbance Observer-Based Control: Methods and Applications.* CRC Press, 2014.

J. S. Light. Tip vortex geometry of a hovering helicopter rotor in ground effect. In *45th Annual Forum Proceedings of the American Helicopter Society*, 1989.

George Limnaios and Nikos Tsourveloudis. Fuzzy logic controller for a mini coaxial indoor helicopter. *Journal of Intelligent and Robotic Systems*, 65:187–201, 2012.

P. B. S. Lissaman. Low-reynolds-number airfoils. *Annual Review of Fluid Mechanics*, 15:223–239, 1983.

Chia-Shang Liu and Huei Peng. Inverse dynamics based state and disturbance observers for linear time-invariant systems. *Journal of Dynamic Systems, Measurement and Control*, 124:375–381, 2002.

Cunjia Liu, Wen-Hua Chen, and John Andrews. Tracking control of small-scale helicopters using explicit nonlinear mpc augmented with disturbance observers. *Control Engineering Practice*, 20:258–268, 2012.

Z. Liu, R. Albertani, J. M. Moschetta, C. Thipyopas, and M. Xu. Experimental and computational evaluation of small microcoaxial rotor in hover. *Journal of Aircraft*, 48(1):220–229, January 2011.

Lennart Ljung. *System Identification Theory for the User*. Prentice Hall, second edition, 1999.

Lennart Ljung. *System Identification Toolbox - User's Guide*. The MathWorks, Inc., 2015.

D. G. Luenberger. Observers for multivariable systems. *IEEE Transactions on Automatic Control*, 11(2):190–197, 1966.

Sebastian O. H. Madgwick, Andrew J. L. Harrison, and Ravi Vaidyanathan. Estimation of imu and marg orientation using a gradient descent algorithm. In *International Conference on Rehabilitation Robotics*, 2011.

P. Marantos, Y. Koveos, and K. L. Kyriakopoulos. Uav state estimation using adaptive complementary filters. *IEEE Transactions on Control Systems Technology*, 2015.

John McCalmont, James Utt, Michael Deschenes, Michael Taylor, Richard Sanderson, Joel Montgomery, Randal S. Johnson, and David McDermott. Sense and avoid

technology for unmanned aircraft systems. In *Proceedings of SPIE 6566, Automatic Target Recognition XVII*, 2007.

Bruce A. McElhoe. An assessment of the navigation and course corrections for a manned flyby of mars or venus. *IEEE Transactions of Aerospace and Electronic Systems*, AES-2(4):613–623, 1966.

Ankur Mehta and Kristofer Pister. Warpwing: A complete open source control platform for miniature robots. In *The 2010 IEEE/RSJ International Conference on Intelligent Robots and Systems*, 2010.

Ankur Mehta, Branko Kerkez, Steven Glaser, and Kristofer Pister. Tdma-based dual-mode communication of mobile wireless sensors networks. *Sensors*, 12:16194–16210, 2012.

Bernard Mettler. *Identification Modeling and Characteristics of Miniature Rotorcraft*. Springer Science+Business Media, 2003.

Bernard Mettler, Mark Tischler, and Takeo Kanade. System identification modeling of a small-scale unmanned rotorcraft for flight control design. *Journal of the American Helicopter Society*, 47:50–63, 2002.

R. J. Miller and R. Mukundan. On designing reduced-order observer for linear time-invariant systems subjected to unknown inputs. *International Journal of Control*, 35(1):183–188, 1982.

Rajat Mittal and Gianluca Iaccarino. Immersed boundary methods. *Annual Review of Fluid Mechanics*, 37:239–261, 2005.

Parvis Moin and Krishnan Mahesh. Direct numerical simulation: A tool in turbulence research. *Annual Review of Fluid Mechanics*, 30:539–578, 1998.

F. Morales and K. D. Squires. Simulation of rotor vortex interactions with a particle-laden turbulent boundary layer. In *29th AIAA Applied Aerodynamics Conference*, 2011.

P. Mukherjee and S. L. Waslander. Modeling and multivariable control techniques for small coaxial helicopters. In *Proceedings of the AIAA Guidance, Navigation and Control Conference and Exhibit*, Portland, OR, USA, August 2011.

P. C. Muller. Indirect measurements of nonlinear effects by state observers. In *Proceedings IUTAB Symposium Nonlinear Dynamics in Engineering Systems*, 1990.

Max M. Munk. General theory of thin wing sections. Technical Report NACA-TR-142, National Advisory Committee for Aeronautics, 1923.

Enrico Natalizio, Rosario Surace, Valeria Loscri, Francesca Guerriero, and Tommaso Melodia. Filming sport events with mobile camera drones: Mathematical modeling and algorithms. 2013.

OptiTrack. *Flex 13*. OptiTrack, 2012a.

OptiTrack. *Tracking Tools 2.4.0 User Guide*. OptiTrack, 2012b.

Gareth D. Padfield. *Helicopter Flight Dynamics: The Theory and Application of Flying Qualities and Simulation Modeling*. American Institute of Aeronautics and Astronautics, 2007.

Robert Porter, Bjian Shirinzadeh, and Man Ho Choi. Experimental analysis of variable collective-pitch rotor systems for multirotor helicopter applications. *Journal of Intelligent & Robotic Systems*, 2015.

Caitlin Powers, Daniel Mellinger, Aleksandr Kushleyev, Bruce Kothmann, and Vijay Kumar. *Experimental Robotics*, chapter Influence of Aerodynamics and Proximity Effects in Quadrotor Flight, pages 289–302. Springer International Publishing, 2013.

Pygame Developers. *Pygame Documentation - Release 1.9.2*. Pygame Developers, 2015.

A. Radke and Zhiqiang Gao. A survey of state and disturbance observers for practitioners. In *American Control Conference, 2006*, 2006.

Manikandan Ramasamy, Timoth E. Lee, and J. Gordon Leishman. Flowfield of a rotating-wing micro air vehicle. *Journal of Aircraft*, 44(4):1236–1244, 2007.

Manikandan Ramasamy, Bradley Johnson, and J. Gordon Leishman. Understanding the aerodynamic efficiency of a hovering micro-rotor. *Journal of the American Helicopter Society*, 53(4):412–428, 2008.

W. J. M. Rankine. On the mechanical principles of the action of propellers. *Transactions of the Institute of Naval Architects*, 6:13–39, 1865.

L. F. Richardson. The approximate arithmetical solution by finite differences of physical problems including differential equations, with an application to the stresses in a masonry dam. *Philosophical Transactions of the Royal Society of London.*, 210:307–357, 1911.

Vernon J. Rossow. Technical notes: Thrust changes induced by ground and ceiling planes on a rotor in hover. *Journal of the American Helicopter Society*, 30(3): 53–55, 1985.

D. Schafroth, C. Bermes, S. Bouabdallah, and R. Siegwart. Modeling, system identification and robust control of a coaxial micro helicopter. *Control Engineering Practice*, 18:700–711, 2010a.

Dario Schafroth. *Aerodynamics, Modeling and Control of an Autonomous Micro Helicopter*. PhD thesis, ETH Zurich, 2010.

Dario Schafroth, Christian Bermes, Samir Bouabdallah, and Roland Siegwart. Modeling and system identification of the mufly micro helicopter. *Journal of Intelligent and Robotic Systems*, 57:27–47, 2010b.

Roland Schiestel. *Modeling and Simulation of Turbulent Flows*. Wiley, 2006.

E. Schrijver and J. van Dijk. Disturbance observers for rigid mechanical systems: Equivalence, stability and design. *Journal of Dynamic Systems, Measurement and Control*, 124(4):539–548, 2002.

Michael S. Selig, James J. Guglielmo, Andy P. Broern, and Philippe Giguere. Summary of low-speed airfoil data. Technical report, University of Illinois at Urbana-Champaign, 1995.

Seneca Instruments. *Z-SG Strain Gauge Converter*. Seneca Instruments, 2015.

Hyo-San Shin, Tae-Hun Kim, and Min-Jea Tahk. Nonlinear formation guidance law with robust disturbance observer. *International Journal of Aeronautical & Space Sciences*, 10(1):30–36, 2009.

Sigurd Skogestad and Ian Postlethwaite. *Multivariable Feedback Control: Analysis and Design*. Wiley and Sons, second edition, 2001.

S. P. Soundararaj, A. K. Sujeeth, and A. Saxena. Autonomous indoor helicopter flight using a single onboard camera. In *International Conference on Intelligent Robots and Systems*, 2009.

P. Spalart and S. Allmaras. A one-equation turbulence model for aerodynamic flows. In *30th Aerospace Sciences Meeting and Exhibit*, 1992.

Philippe Spalart. Trends in turbulence treatments. In *Fluids 2000 Conference and Exhibit*, 2000.

Spektrum. *DX4e 4-Channel Full Range DSM 2.4GHz Transmitter*. Spektrum, 2011.

G. R. Srinivasan and J. D. Baeder. Turns - a free-wake euler/navier-stokes numerical method for helicopter rotors. *AIAA Journal*, 31:959–962, 1993.

G. R. Srinivasan, J. D. Baeder, S. Obayashi, and W. J. McCroskey. Flowfield of a lifting rotor in hover - a navier-stokes simulation. *AIAA Journal*, 30:2371–2378, 1992.

G. R. Srinivasan, V. Raghavan, E. P. N. Duque, and W. J. McCroskey. Flowfield analysis of modern helicopter rotors in hover by navier-stokes method. *Journal of the American Helicopter Society*, 38(3):3–13, 1993.

J. L. Steger, F. C. Dougherty, and J. A. Benek. Chimera grid scheme. *ASME Fluids Engineering Division*, 5:59–69, 1983.

J. L. Stein and Y. Park. Measurement signal selection and a simultaneous state and input observer. *Journal of Dynamic Systems, Measurement and Control*, 110: 151–159, 1988.

J. Steinhoff and N. Lynn. *Computing the Future IV: frontiers of computational fluid dynamics*, chapter Chapter 10, pages 786–793. Springer-Verlag, 2006.

STMicroelectronics. *LIS344ALH MEMS inertial sensor high performance 3-axis ±2/±6g ultracompact linear accelerometer*, 2008.

Roger C. Strawn, Francis X. Caradonna, and Earl P. N. Duque. 30 years of rotorcraft computational fluid dynamics research and development. *Journal of the American Helicopter Society*, 51:5–21, 2006.

L. Tang. *Improved Euler Simulation of Helicopter Vortical Flows*. PhD thesis, University of Maryland at College Park, 1998.

James L. Tangler, Robert M. Wohlfeld, and Stan J. Miley. An experimental investigation of vortex stability, tip shapes, compressibility, and noise for hovering model rotors. Technical Report CR-2305, NASA, 1973.

Brook Taylor. *Methodus Incrementorum Directa et Inversa*. 1715.

Marion K. Taylor. A balsa-dust technique for air-flow visualization and its application to flow through model helicopter rotors in static thrust. Technical Report 2220, NACA, 1950.

Texas Instruments. *±2.5°C Low-Power, Analog Out TEMPERATURE SENSOR*. Texas Instruments, 2009.

T. L. Thompson, N. M. Komerath, and R. B. Gray. Visualization and measurement of the tip vortex core of a rotor blade in hover. *AIAA Journal of Aircraft*, 25(12): 1113–1121, 1988.

M. B. Tischler and M. G. Cauffman. Frequency-response method for rotorcraft system identification: Flight application to bo-105 coupled rotor/fueslage dynamics. *Journal of the American Helicopter Society*, 37(3):3–17, 1992.

T. Umeno and Y. Hori. Robust speed control of dc servomotors using modern two degrees-of-freedom controller design. *IEEE Transactions on Industrial Electronics*, 38(5):363–368, 1991.

Roberto G. Valenti, Ivan Dryanovski, and Jizhong Xiao. Keeping a good attitude: A quaternion-based orientation filter for imus and margs. *Sensors*, 15:19302–19330, 2015.

G. H. Vatistias, V. Kozel, and W. C. Mih. A simpler model for concentrated vortices. *Experiments in Fluids*, 11:72–76, 1991.

V. Venkatakrishnan. Perspective on unstructured grid flow solvers. *AIAA Journal*, 34(3):533–547, 1996.

Vishay Siliconix. *N-Channel 8-V (D-S) MOSFET*. Vishay Siliconix, 2012.

B. E. Wake and J. D. Baeder. Evaluation of a navier-stokes analysis method for hover performance prediction. *Journal of the American Helicopter Society*, 41(1): 7–17, 1996.

N. Weiner. *Extrapolation, Interpolation and Smoothing of Stationary Time Series*. MIT Press, 1949.

Peter D. Welch. The use of fast fourier transform for the estimation of power spectra: A method based on time averaging over short, modified periodograms. *IEEE Transactions on Audio and Electroacoustics*, 15:70–73, 1967.

Frank M. White. *Fluid Mechanics*. McGraw Hill, 2003.

Adrian Wills, B. Ninness, and S. Gibson. On gradient-based search for multivariable system estimates. In *Proceedings of the 16th IFAC World Congress*, 2005.

Ye Xie, Yunfeng Cao, Biao Wang, and Meng Ding. Disturbance observer based control of multirotor helicopters based on a universal model with unstructured uncertainties. *Journal of Robotics*, 2015, 2015.

Xinfu Ye, Lian Zhu, Sun Changyin, and Wei Wang. *Intelligence Science and Big Data Engineering*, chapter An Attitude Determination System of Quad-rotor

Aircraft Based on Extended Kalman Filter and Data Fusion Technique, pages 764–770. Springer Berlin Heidelberg, 2013.

Fanglai Zhu. State estimation and unknown input reconstruction via both reduced-order and high-order sliding mode observers. *Journal of Process Control*, 22(1): 296–302, 2012.

Appendix A

Additional Computational Fluid Dynamics Results

For clarity, and to maintain a coherent structure for this thesis, some CFD results have been left out of the main body of this thesis. For the benefit of the reader, these additional results are included in this appendix.

A.1 Fluid Interactions Between a Hovering Micro Rotor and a Ground Plane

As outlined in Section 5.2, simulations of a hovering micro rotor near a ground plane have been conducted in order to validate the CFD method used in this research. For completeness, additional CFD results for the near-ground case are presented in this section.

A.1.1 Induced Velocity

A plot of non-dimensionalised induced velocity against non-dimensionalised radius is provided in Figure A.1 . For $r/R < 0.75$ there is a significant decrease in induced velocity relative to the baseline case as rotor-ground gap decreases. The decrease in induced velocity is most significant toward the rotor hub. This is because there is stagnation in the flow directly below the rotor hub near the blade surface, forcing a

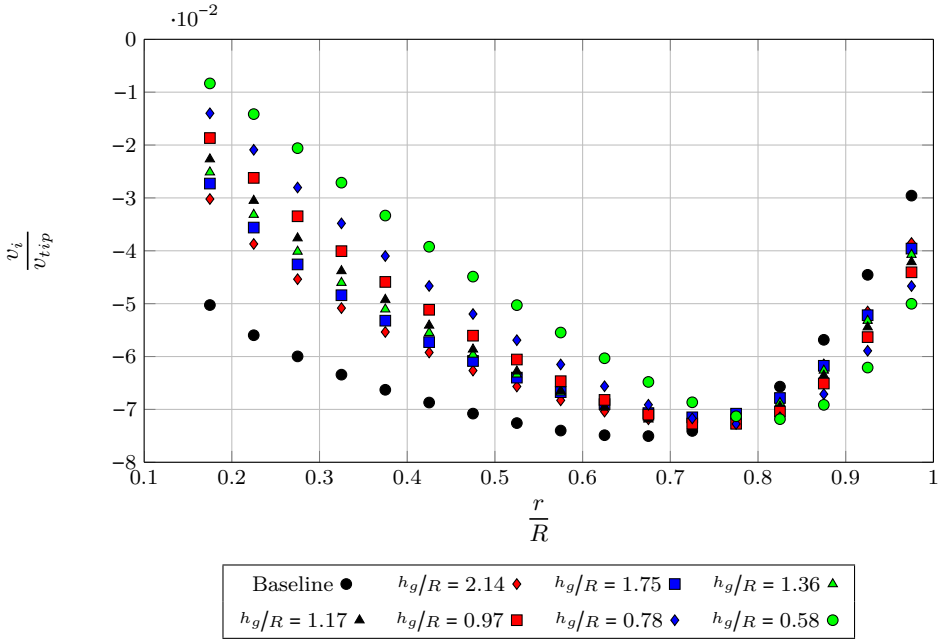

Figure A.1: Effect of rotor-ground gap on induced velocity. Plot shows non-dimensionalised induced velocity vs non-dimensionalised spanwise distance.

very small induced velocity toward the rotor hub. For $r/R > 0.75$, there is an increase in induced velocity relative to the baseline case as rotor-ground gap decreases. The increase in induced velocity becomes more significant toward the rotor tip. This is because radial expansion of the flow forces a larger proportion of mass flow rate through the rotor disk to occur toward the blade tip.

A.1.2 Local Effective Angle of Attack

Local effective angle of attack is plotted against non-dimensionalised radius in Figure A.2. For $r/R < 0.75$, there is a significant increase in local effective angle of attack as rotor-ground gap decreases. This increase is most significant toward the rotor hub. At $h_g/R = 0.58$ the minimum local effective angle of attack is 6.5°, occurring at $r/R = 0.575$. In contrast, for the baseline case, the local effective angle of attack keeps decreasing toward the rotor hub and is below -4° at $r/R = 0.175$. For $r/R > 0.75$, there is a decrease in local effective angle of attack as rotor-ground gap decreases. These observed changes in local effective angle of attack are directly driven by the changes in induced velocity previously shown in Figure A.1 . Note that the change in local effective angle of attack is small toward the blade tip because here it is

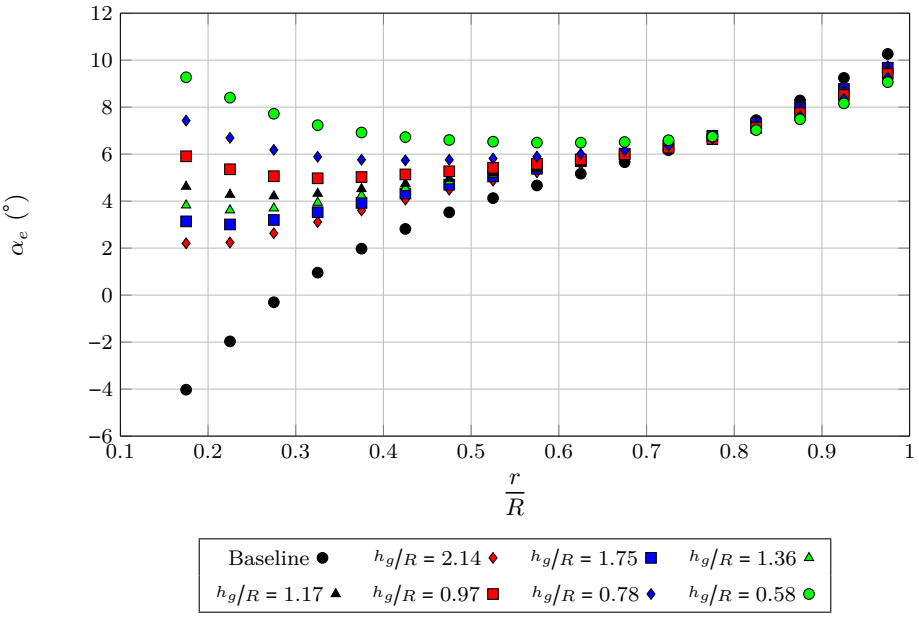

FIGURE A.2: Effect of rotor-ground gap on local effective angle of attack. Plot shows local effective angle of attack vs non-dimensionalised spanwise distance.

dominated by the incident velocity (Ωr). The change is large toward the rotor hub because here the incident velocity is close to zero. The increase in local effective angle of attack is the primary mechanism that drives the increase in thrust ratio, previously shown in Figure 5.6.

A.1.3 Blade Pressure Field

In Figure A.3, contours of pressure coefficient, C_p, at the top and bottom surfaces of the blade are plotted. At the top surface of the blade, the contours show that there is a low pressure region at the leading edge of the blade that runs from approximately a quarter of the blade span to the blade tip. From the blade hub to approximately 1/4 of the blade span there is a high pressure region at the leading edge. This high pressure region is present for the baseline case because the local effective angle of attack is negative near the blade hub, as previously shown in Figure A.2. As the rotor-ground gap decreases, the low pressure region extends further toward the rotor hub. This is due to the increase in local effective angle of attack that is experienced near the blade hub as rotor-ground gap decreases.

At the bottom surface of the blade for the baseline case, there is a distinct high

pressure region at the leading edge that stretches from approximately $1/4$ of the blade span to the blade tip. Additionally, there is a low pressure region at the blade tip behind the leading edge high pressure region. This low pressure region is caused by the highly 3D flow that is present as the flow around the blade tip rolls up into the blade tip vortex. As the rotor-ground gap decreases, the high pressure region at the leading edge of the bottom surface of the blade extends further toward the blade hub. With the exception of the low pressure region at the blade tip, the entire bottom surface of the blade has a high pressure acting on it by $h_g/R = 0.58$.

A.1.4 Spanwise Loading

Sectional thrust and power coefficients across the blade span can be obtained by integrating the pressure contours shown in Figures A.3 over the blade. Sectional thrust coefficient and sectional power coefficient are plotted against non-dimensionalised spanwise distance in Figures A.4(a) and A.4(b) respectively. For spanwise distance less than $r/R < 0.85$ there is a significant increase in thrust coefficient as rotor-ground gap decreases. This is due to the increase in local effective angle of attack that occurs toward the rotor hub as rotor-ground gap decreases. There is a small decrease in sectional thrust coefficient for spanwise locations greater than $r/R > 0.85$. This is due to the decrease in local effective angle of attack that occurs toward the blade hub. This decrease in thrust coefficient near the blade tip is consistent with the results of Kalra (2014) for a blunt leading edge/sharp trailing edge cambered airfoil at a blade tip Reynolds number of $32,400$ and angle of attack of 12°. For the sectional power coefficient results, there is a clear increase as rotor-ground gap decreases for spanwise distances less than $r/R < 0.8$. Near the blade tip, sectional power coefficient begins to decrease for very small rotor-ground gaps. Once again, this is due to the decrease in local effective angle of attack near the blade tip. The changes in spanwise blade loading discussed in this section directly induce the changes in rotor thrust ratio previously shown in Figure 5.6.

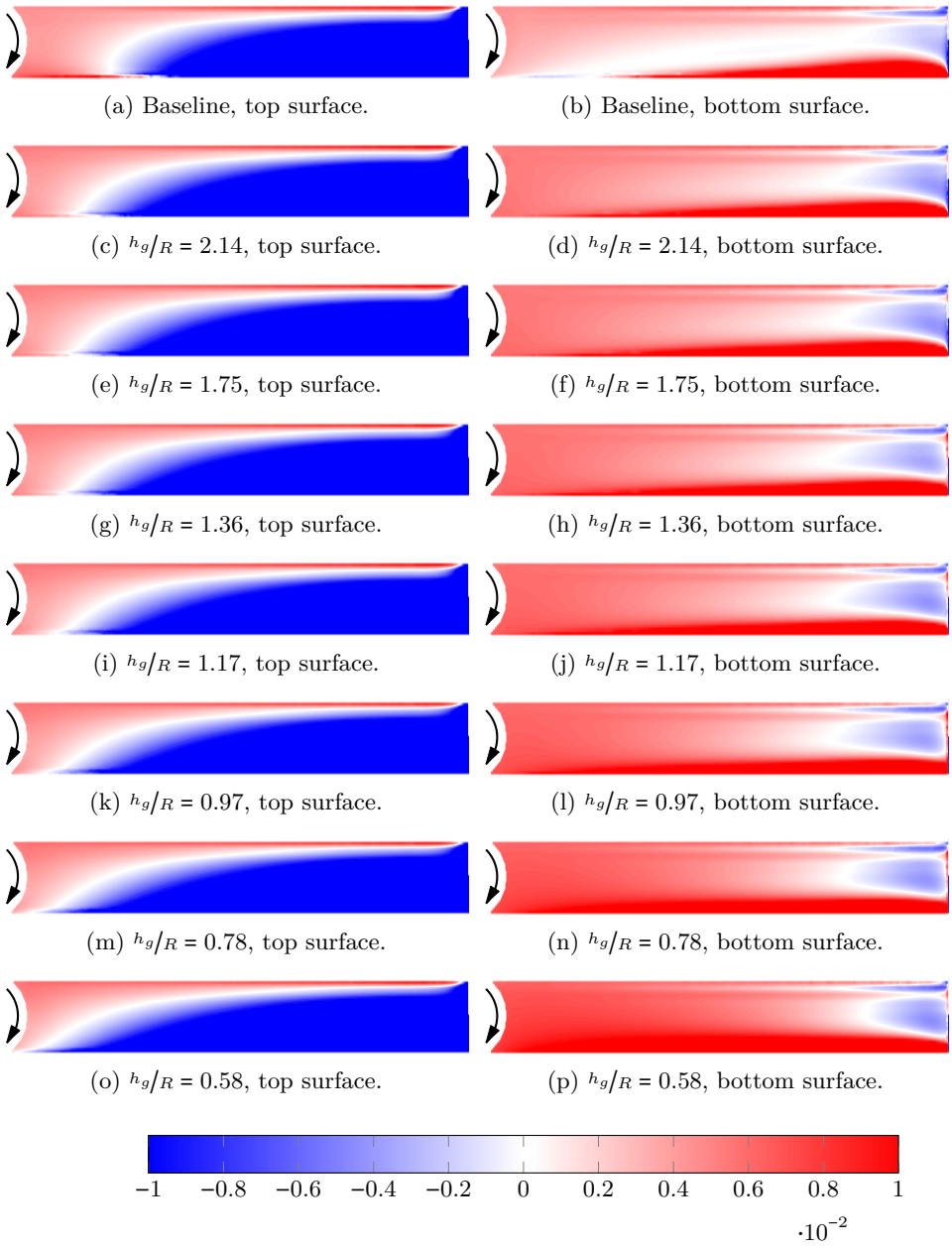

(a) Baseline, top surface.
(b) Baseline, bottom surface.
(c) h_g/R = 2.14, top surface.
(d) h_g/R = 2.14, bottom surface.
(e) h_g/R = 1.75, top surface.
(f) h_g/R = 1.75, bottom surface.
(g) h_g/R = 1.36, top surface.
(h) h_g/R = 1.36, bottom surface.
(i) h_g/R = 1.17, top surface.
(j) h_g/R = 1.17, bottom surface.
(k) h_g/R = 0.97, top surface.
(l) h_g/R = 0.97, bottom surface.
(m) h_g/R = 0.78, top surface.
(n) h_g/R = 0.78, bottom surface.
(o) h_g/R = 0.58, top surface.
(p) h_g/R = 0.58, bottom surface.

FIGURE A.3: Effect of rotor-ground gap on blade pressure field. Plots show contours of pressure coefficient, C_p, (measured relative to far-field pressure) at blade surface.

A.1.5 Relationship Between Vertical Force Disturbance and Rotor-Ground Gap

In this section, the effect of changes in thrust ratio (induced by ground proximity) on the helicopter hovering dynamics identified in Section 3.3 is discussed. The variation in thrust ratio shown in Figure 5.6 will generate a vertical force disturbance, $\overline{Z}$,

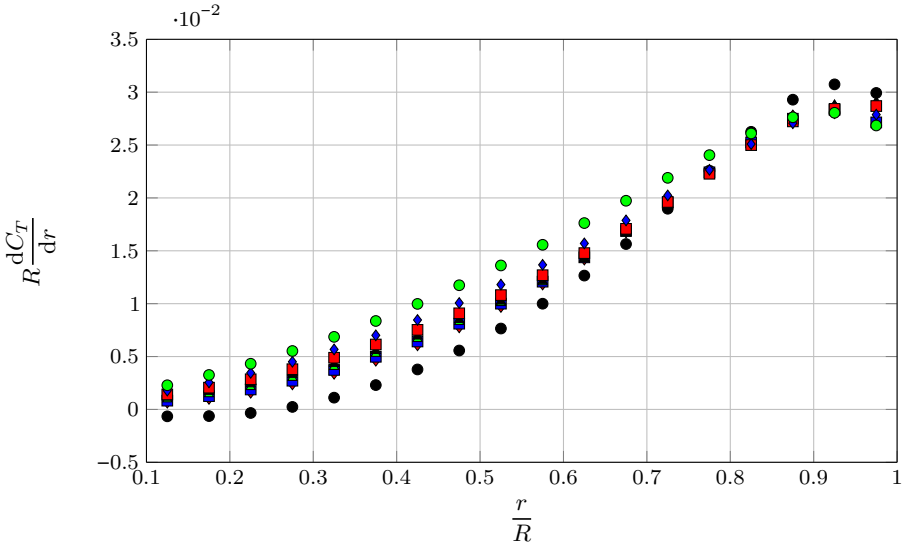

(a) Sectional thrust coefficient vs non-dimensionalised spanwise distance.

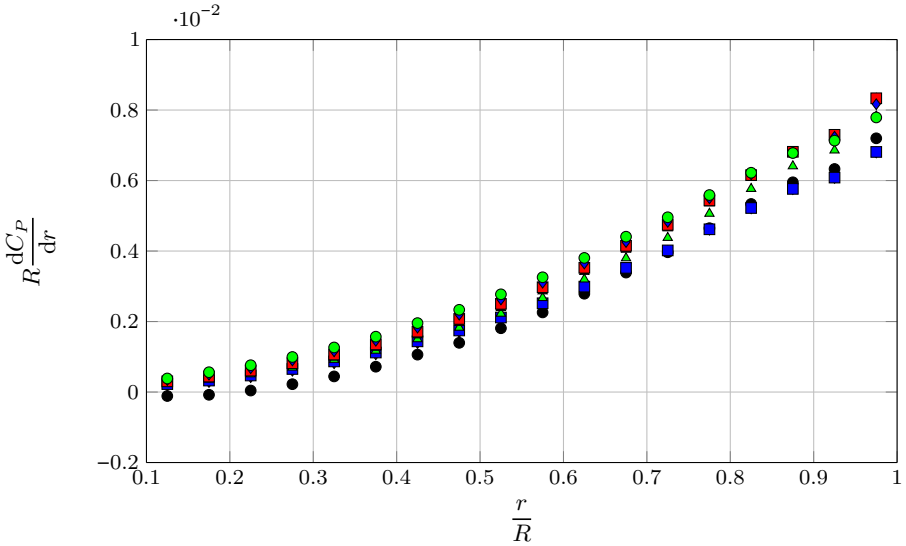

(b) Sectional power coefficient vs non-dimensionalised spanwise distance.

Baseline ●	h_g/R = 2.14 ♦	h_g/R = 1.75 ■	h_g/R = 1.36 ▲
h_g/R = 1.17 ▲	h_g/R = 0.97 ■	h_g/R = 0.78 ♦	h_g/R = 0.58 ●

Figure A.4: Effect of rotor-ground gap on loading across blade span.

acting on the micro helicopter. In order to quantify the effect that this disturbance will have on helicopter hovering dynamics, it is useful to characterise the relationship between $\overline{Z}$ and ground proximity

$$\overline{Z} \approx -mg \cdot 0.0996 \left(\frac{h_g}{R}\right)^{-1.34}, \tag{A.1}$$

where the power law described by Equation (A.1) has been fitted to the CFD results using least squares regression with a R^2 value of 0.97383. Note that Equation (A.1) will tend to infinity as h_g tends to zero. Clearly, this is a non physical result. With this in mind, it is important to acknowledge that the relationship described by Equation (A.1) will only be valid when the rotor is outside of the ground boundary layer.

A.2 Fluid Interactions Between a Hovering Micro Rotor and a Wall Plane

A.2.1 Flow Field

As outlined in Section 7.1.2, fluid interactions between a hovering micro rotor and a wall plane occur predominantly in the plane normal to the wall. As such, the CFD results presented in Chapter 7 focus primarily on effects that occur in this plane. For completeness, additional flow field visualisations for the plane parallel to the wall are included in Figures A.5, A.6, A.7 and A.8. These figures clearly demonstrate that the wall plane has little effect on the flow field when analysing the plane parallel to the wall.

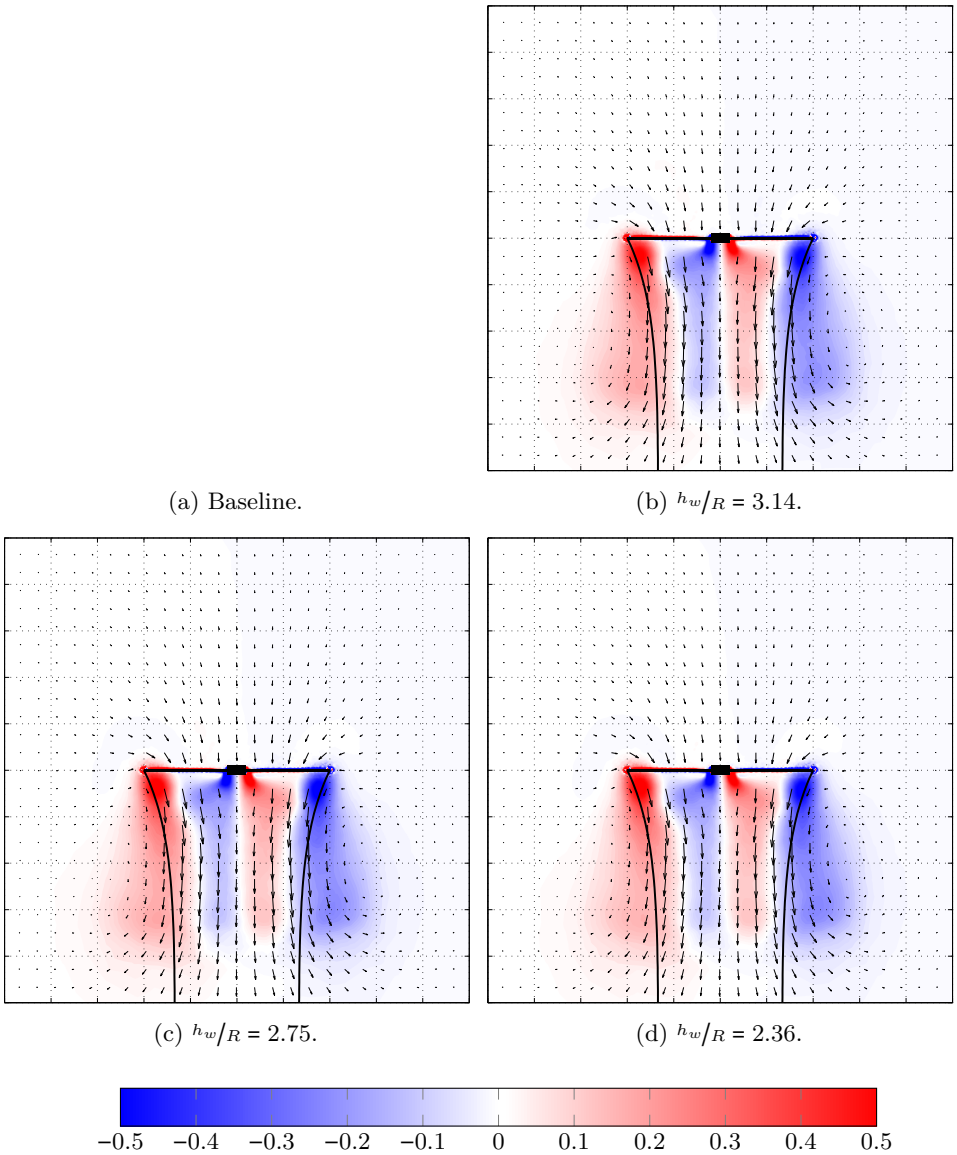

(a) Baseline.

(b) $h_w/R = 3.14$.

(c) $h_w/R = 2.75$.

(d) $h_w/R = 2.36$.

Figure A.5: Flow field through a hovering micro rotor in close proximity to a wall plane. Plots show sectional contours of vorticity non-dimensionalised by rotor speed, ω/Ω, and velocity vectors at $\zeta = 0^\circ$ and $\phi_w = 90^\circ/270^\circ$ at different rotor-wall gaps, h_w. Wake slipstream boundary obtained using the 2D FV model is indicated by the solid black line (——). The grid lines are separated by $0.5R$.

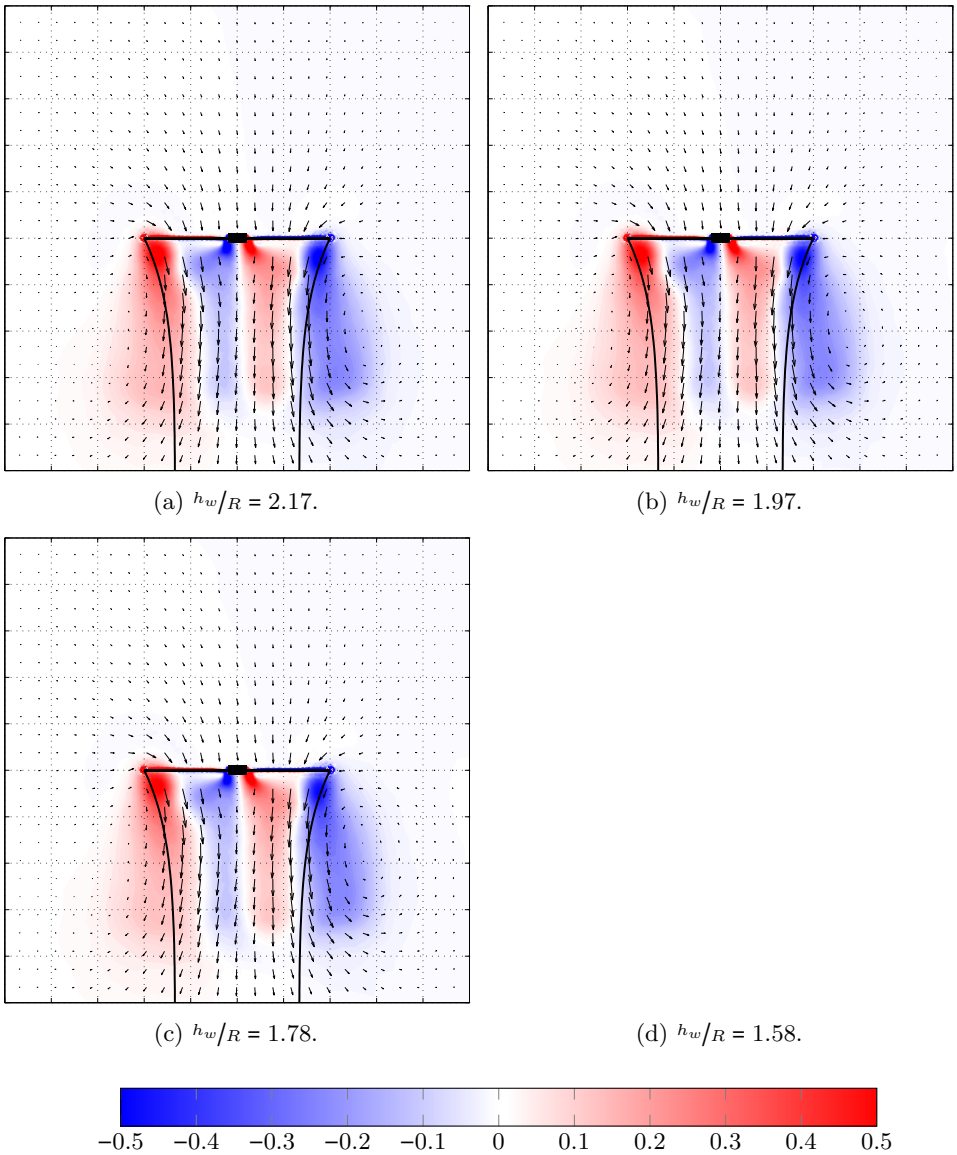

(a) h_w/R = 2.17.

(b) h_w/R = 1.97.

(c) h_w/R = 1.78.

(d) h_w/R = 1.58.

FIGURE A.6: Flow field through a hovering micro rotor in close proximity to a wall plane. Plots show sectional contours of vorticity non-dimensionalised by rotor speed, ω/Ω, and velocity vectors at $\zeta = 0^\circ$ and $\phi_w = 90^\circ/270^\circ$ at different rotor-wall gaps, h_w. Wake slipstream boundary obtained using the 2D FV model is indicated by the solid black line (——). The grid lines are separated by $0.5R$.

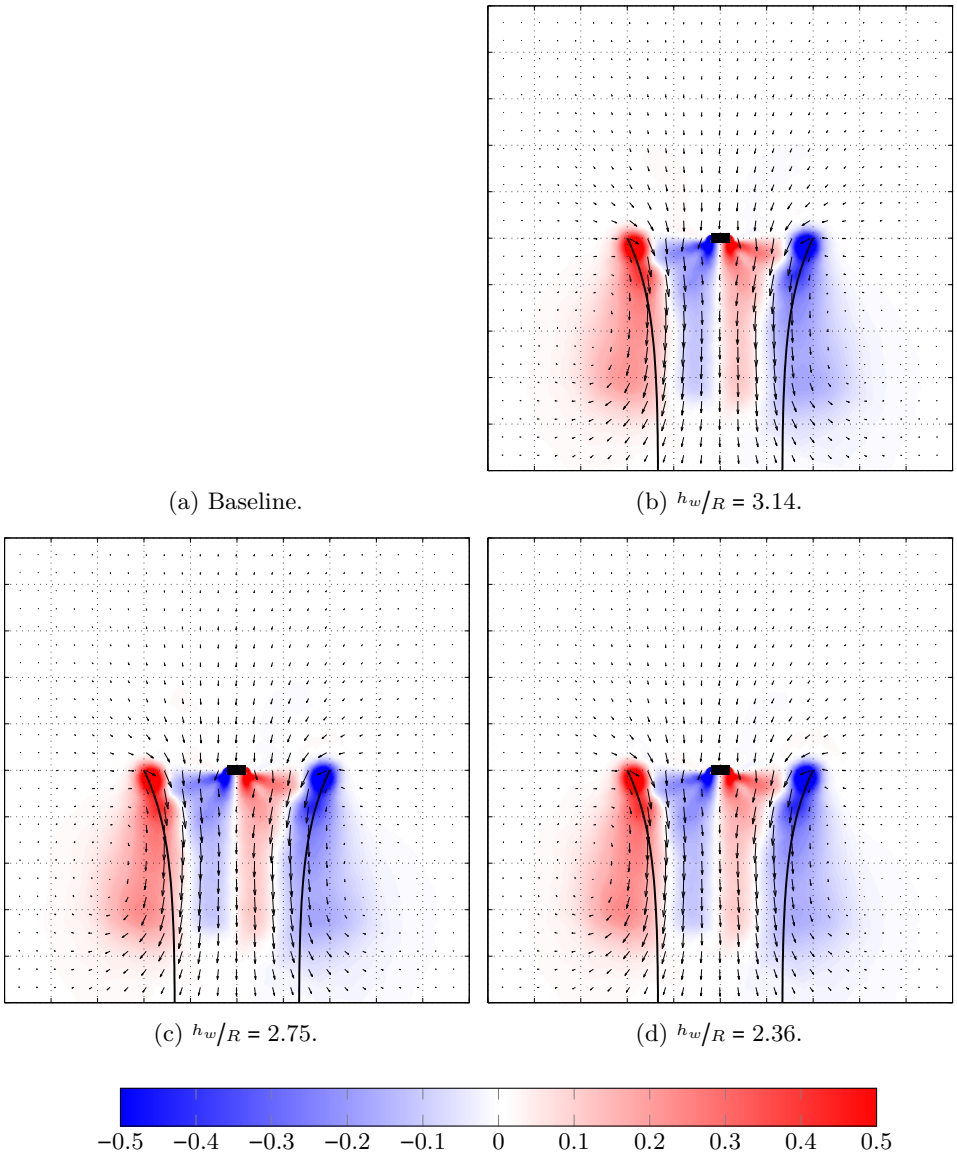

(a) Baseline.

(b) $h_w/R = 3.14$.

(c) $h_w/R = 2.75$.

(d) $h_w/R = 2.36$.

Figure A.7: Flow field through a hovering micro rotor in close proximity to a wall plane. Plots show sectional contours of vorticity non-dimensionalised by rotor speed, ω/Ω, and velocity vectors at $\zeta = 90^\circ$ and $\phi_w = 0^\circ/180^\circ$ at different rotor-wall gaps, h_w. Wake slipstream boundary obtained using the 2D FV model is indicated by the solid black line (——). The grid lines are separated by $0.5R$.

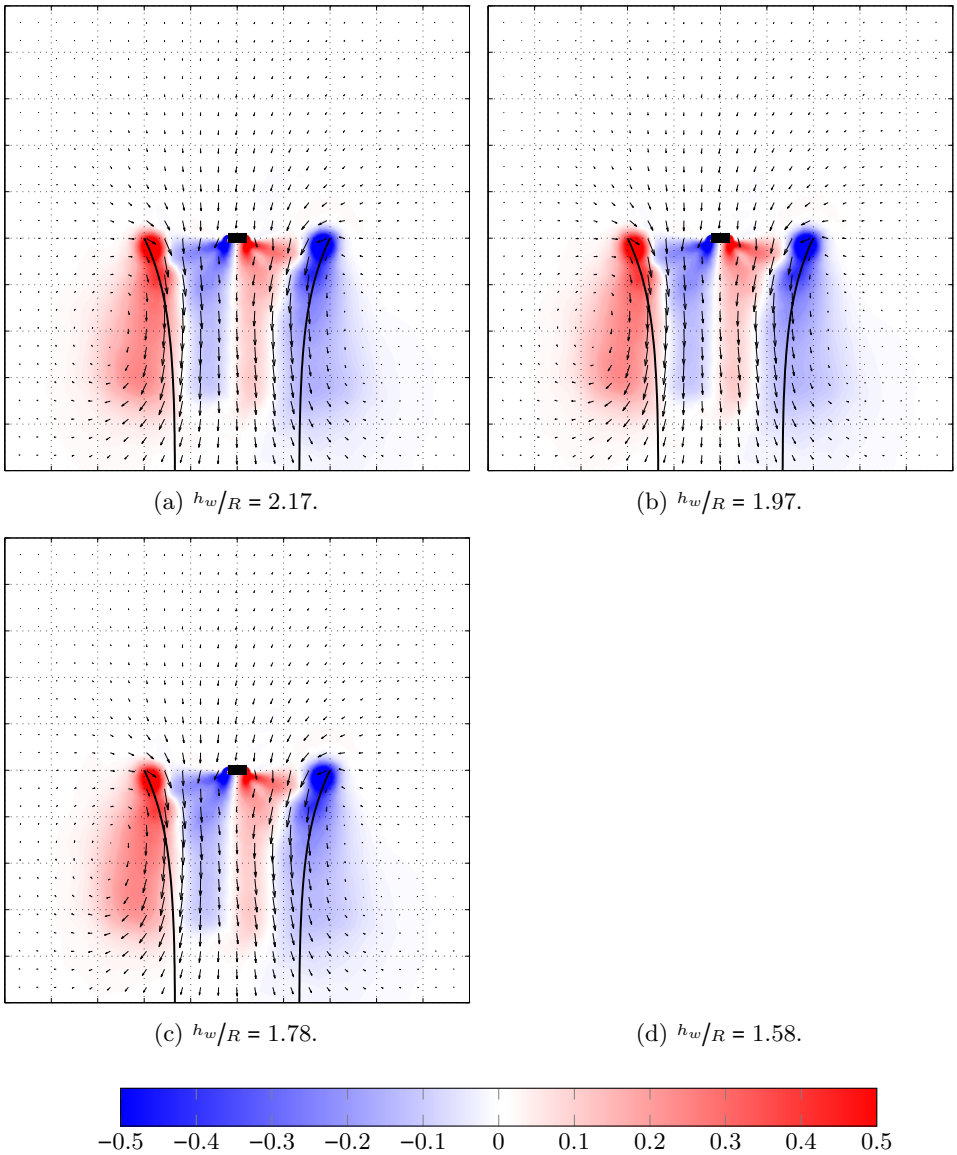

(a) h_w/R = 2.17.

(b) h_w/R = 1.97.

(c) h_w/R = 1.78.

(d) h_w/R = 1.58.

FIGURE A.8: Flow field through a hovering micro rotor in close proximity to a wall plane. Plots show sectional contours of vorticity non-dimensionalised by rotor speed, ω/Ω, and velocity vectors at $\zeta = 90^\circ$ and $\phi_w = 0^\circ/180^\circ$ at different rotor-wall gaps, h_w. Wake slipstream boundary obtained using the 2D FV model is indicated by the solid black line (——). The grid lines are separated by $0.5R$.